Available online at www.sciencedirect.com

Friction stir welding and processing

R.S. Mishra^{a,*}, Z.Y. Ma^b^aCenter for Friction Stir Processing, Department of Materials Science and Engineering, University of Missouri, Rolla, MO 65409, USA^bInstitute of Metal Research, Chinese Academy of Sciences, Shenyang 110016, China

Available online 18 August 2005

Abstract

Friction stir welding (FSW) is a relatively new solid-state joining process. This joining technique is energy efficient, environment friendly, and versatile. In particular, it can be used to join high-strength aerospace aluminum alloys and other metallic alloys that are hard to weld by conventional fusion welding. FSW is considered to be the most significant development in metal joining in a decade. Recently, friction stir processing (FSP) was developed for microstructural modification of metallic materials. In this review article, the current state of understanding and development of the FSW and FSP are addressed. Particular emphasis has been given to: (a) mechanisms responsible for the formation of welds and microstructural refinement, and (b) effects of FSW/FSP parameters on resultant microstructure and final mechanical properties. While the bulk of the information is related to aluminum alloys, important results are now available for other metals and alloys. At this stage, the technology diffusion has significantly outpaced the fundamental understanding of microstructural evolution and microstructure–property relationships.

© 2005 Elsevier B.V. All rights reserved.

Keywords: Friction stir welding; Friction stir processing; Weld; Processing; Microstructure

1. Introduction

The difficulty of making high-strength, fatigue and fracture resistant welds in aerospace aluminum alloys, such as highly alloyed 2XXX and 7XXX series, has long inhibited the wide use of welding for joining aerospace structures. These aluminum alloys are generally classified as non-weldable because of the poor solidification microstructure and porosity in the fusion zone. Also, the loss in mechanical properties as compared to the base material is very significant. These factors make the joining of these alloys by conventional welding processes unattractive. Some aluminum alloys can be resistance welded, but the surface preparation is expensive, with surface oxide being a major problem.

Friction stir welding (FSW) was invented at The Welding Institute (TWI) of UK in 1991 as a solid-state joining technique, and it was initially applied to aluminum alloys [1,2]. The basic concept of FSW is remarkably simple. A non-consumable rotating tool with a specially designed pin and shoulder is inserted into the abutting edges of sheets or plates to be joined and traversed along the line of joint (Fig. 1). The tool serves two primary functions: (a) heating of workpiece, and (b) movement of material to produce the joint. The heating is accomplished by friction between the tool and the workpiece and plastic deformation of workpiece. The localized heating softens the material around the pin and combination of tool rotation and translation leads to movement of material from the front of

* Corresponding author. Tel.: +1 573 341 6361; fax: +1 573 341 6934.
E-mail address: rsmishra@umr.edu (R.S. Mishra).

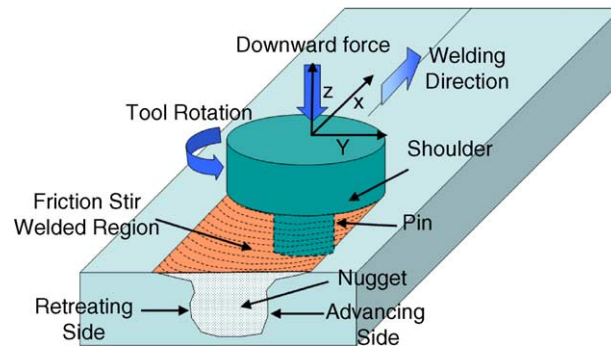


Fig. 1. Schematic drawing of friction stir welding.

the pin to the back of the pin. As a result of this process a joint is produced in ‘solid state’. Because of various geometrical features of the tool, the material movement around the pin can be quite complex [3]. During FSW process, the material undergoes intense plastic deformation at elevated temperature, resulting in generation of fine and equiaxed recrystallized grains [4–7]. The fine microstructure in friction stir welds produces good mechanical properties.

FSW is considered to be the most significant development in metal joining in a decade and is a “green” technology due to its energy efficiency, environment friendliness, and versatility. As compared to the conventional welding methods, FSW consumes considerably less energy. No cover gas or flux is used, thereby making the process environmentally friendly. The joining does not involve any use of filler metal and therefore any aluminum alloy can be joined without concern for the compatibility of composition, which is an issue in fusion welding. When desirable, dissimilar aluminum alloys and composites can be joined with equal ease [8–10]. In contrast to the traditional friction welding, which is usually performed on small axisymmetric parts that can be rotated and pushed against each other to form a joint [11], friction stir welding can be applied to various types of joints like butt joints, lap joints, T butt joints, and fillet joints [12]. The key benefits of FSW are summarized in Table 1.

Recently friction stir processing (FSP) was developed by Mishra et al. [13,14] as a generic tool for microstructural modification based on the basic principles of FSW. In this case, a rotating tool is inserted in a monolithic workpiece for localized microstructural modification for specific property enhancement. For example, high-strain rate superplasticity was obtained in commercial 7075Al alloy

Table 1
Key benefits of friction stir welding

Metallurgical benefits	Environmental benefits	Energy benefits
Solid phase process	No shielding gas required	Improved materials use (e.g., joining different thickness) allows reduction in weight
Low distortion of workpiece	No surface cleaning required	Only 2.5% of the energy needed for a laser weld
Good dimensional stability and repeatability	Eliminate grinding wastes	Decreased fuel consumption in light weight aircraft, automotive and ship applications
No loss of alloying elements	Eliminate solvents required for degreasing	
Excellent metallurgical properties in the joint area	Consumable materials saving, such as rags, wire or any other gases	
Fine microstructure		
Absence of cracking		
Replace multiple parts joined by fasteners		

by FSP [13–15]. Furthermore, FSP technique has been used to produce surface composite on aluminum substrate [16], homogenization of powder metallurgy aluminum alloy [17], microstructural modification of metal matrix composites [18] and property enhancement in cast aluminum alloys [19].

FSW/FSP is emerging as a very effective solid-state joining/processing technique. In a relatively short duration after invention, quite a few successful applications of FSW have been demonstrated [20–23]. In this paper, the current state of understanding and development of the FSW and FSP are reviewed.

2. Process parameters

FSW/FSP involves complex material movement and plastic deformation. Welding parameters, tool geometry, and joint design exert significant effect on the material flow pattern and temperature distribution, thereby influencing the microstructural evolution of material. In this section, a few major factors affecting FSW/FSP process, such as tool geometry, welding parameters, joint design are addressed.

2.1. Tool geometry

Tool geometry is the most influential aspect of process development. The tool geometry plays a critical role in material flow and in turn governs the traverse rate at which FSW can be conducted. An FSW tool consists of a shoulder and a pin as shown schematically in Fig. 2. As mentioned earlier, the tool has two primary functions: (a) localized heating, and (b) material flow. In the initial stage of tool plunge, the heating results primarily from the friction between pin and workpiece. Some additional heating results from deformation of material. The tool is plunged till the shoulder touches the workpiece. The friction between the shoulder and workpiece results in the biggest component of heating. From the heating aspect, the relative size of pin and shoulder is important, and the other design features are not critical. The shoulder also provides confinement for the heated volume of material. The second function of the tool is to ‘stir’ and ‘move’ the material. The uniformity of microstructure and properties as well as process loads are governed by the tool design. Generally a concave shoulder and threaded cylindrical pins are used.

With increasing experience and some improvement in understanding of material flow, the tool geometry has evolved significantly. Complex features have been added to alter material flow, mixing and reduce process loads. For example, WhorlTM and MX TrifluteTM tools developed by TWI are

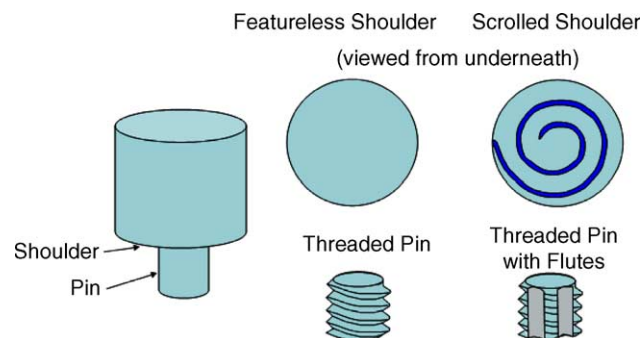


Fig. 2. Schematic drawing of the FSW tool.

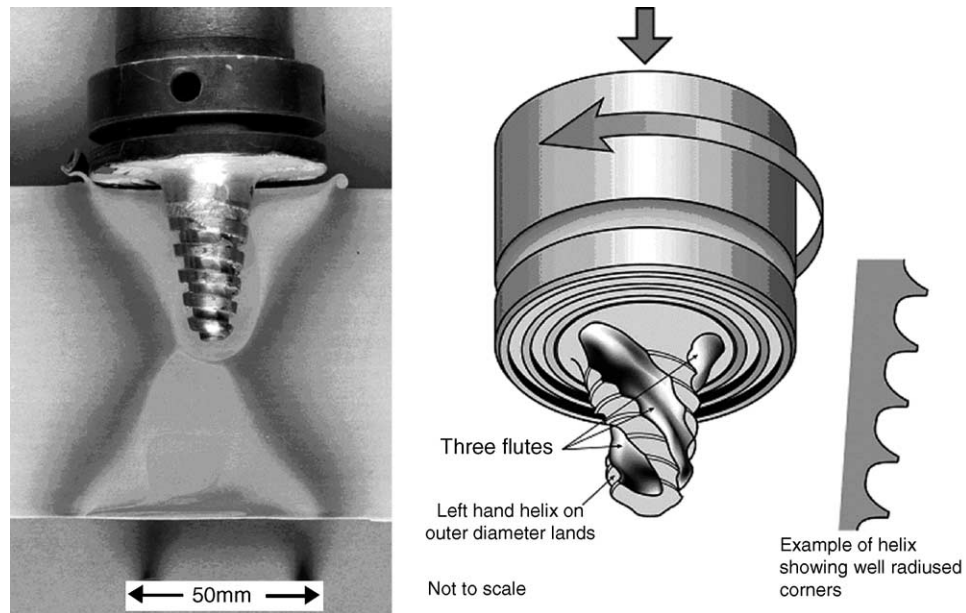


Fig. 3. WhorlTM and MX TrifluteTM tools developed by The Welding Institute (TWI), UK (Copyright © 2001, TWI Ltd) (after Thomas et al. [24]).

shown in Fig. 3. Thomas et al. [24] pointed out that pins for both tools are shaped as a frustum that displaces less material than a cylindrical tool of the same root diameter. Typically, the WhorlTM reduces the displaced volume by about 60%, while the MX TrifluteTM reduces the displaced volume by about 70%. The design features of the WhorlTM and the MX TrifluteTM are believed to (a) reduce welding force, (b) enable easier flow of plasticized material, (c) facilitate the downward augering effect, and (d) increase the interface between the pin and the plasticized material, thereby increasing heat generation. It has been demonstrated that aluminum plates with a thickness of up to 50 mm can be successfully friction stir welded in one pass using these two tools. A 75 mm thick 6082Al-T6 FSW weld was made using WhorlTM tool in two passes, each giving about 38 mm penetration. Thomas et al. [24] suggested that the major factor determining the superiority of the whorl pins over the conventional cylindrical pins is the ratio of the swept volume during rotation to the volume of the pin itself, i.e., a ratio of the “dynamic volume to the static volume” that is important in providing an adequate flow path. Typically, this ratio for pins with similar root diameters and pin length is 1.1:1 for conventional cylindrical pin, 1.8:1 for the WhorlTM and 2.6:1 for the MX TrifluteTM pin (when welding 25 mm thick plate).

For lap welding, conventional cylindrical threaded pin resulted in excessive thinning of the top sheet, leading to significantly reduced bend properties [25]. Furthermore, for lap welds, the width of the weld interface and the angle at which the notch meets the edge of the weld is also important for applications where fatigue is of main concern. Recently, two new pin geometries—Flared-TrifluteTM with the flute lands being flared out (Fig. 4) and A-skewTM with the pin axis being slightly inclined to the axis of machine spindle (Fig. 5) were developed for improved quality of lap welding [25–27]. The design features of the Flared-TrifluteTM and the A-skewTM are believed to: (a) increase the ratio between of the swept volume and static volume of the pin, thereby improving the flow path around and underneath the pin, (b) widen the welding region due to flared-out flute lands in the Flared-TrifluteTM pin and the skew action in the A-skewTM pin, (c) provide an improved mixing action for oxide fragmentation and dispersal at the weld interface, and (d) provide an orbital forging action at the root of the weld due to the skew action, improving weld quality in this region. Compared to the

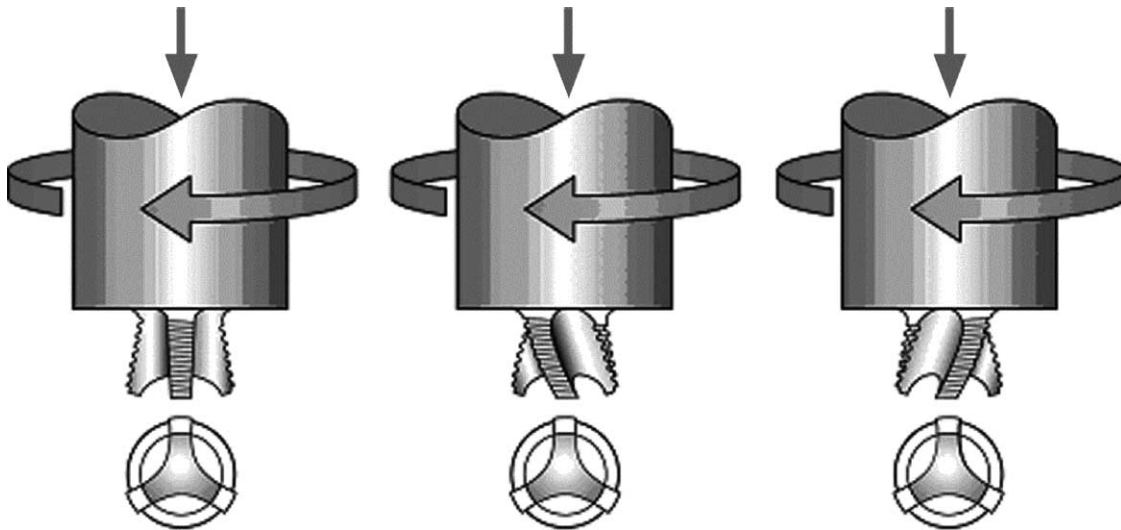


Fig. 4. Flared-Triflute™ tools developed by The Welding Institute (TWI), UK: (a) neutral flutes, (b) left flutes, and (c) right hand flutes (after Thomas et al. [25]).

conventional threaded pin, Flared-Triflute™ and A-skew™ pins resulted in: (a) over 100% improvement in welding speed, (b) about 20% reduction in axial force, (c) significantly widened welding region (190–195% of the plate thickness for Flared-Triflute™ and A-skew™ pins, 110% for conventional threaded pin), and (d) a reduction in upper plate thinning by a factor of >4 [27]. Further, Flared-Triflute™ pin reduced significantly the angle of the notch upturn at the overlapping plate/weld interface, whereas A-skew™ pin produced a slight downturn at the outer regions of the overlapping plate/weld interface, which are beneficial to improving the properties of the FSW joints [25,27]. Thomas and Dolby [27] suggested that both Flared-Triflute™ and A-skew™ pins are suitable for lap, T, and similar welds where joining interface is vertical to the machine axis.

Further, various shoulder profiles were designed in TWI to suit different materials and conditions (Fig. 6). These shoulder profiles improve the coupling between the tool shoulder and the workpieces by entrapping plasticized material within special re-entrant features.

Considering the significant effect of tool geometry on the metal flow, fundamental correlation between material flow and resultant microstructure of welds varies with each tool. A critical need is to develop systematic framework for tool design. Computational tools, including finite element analysis

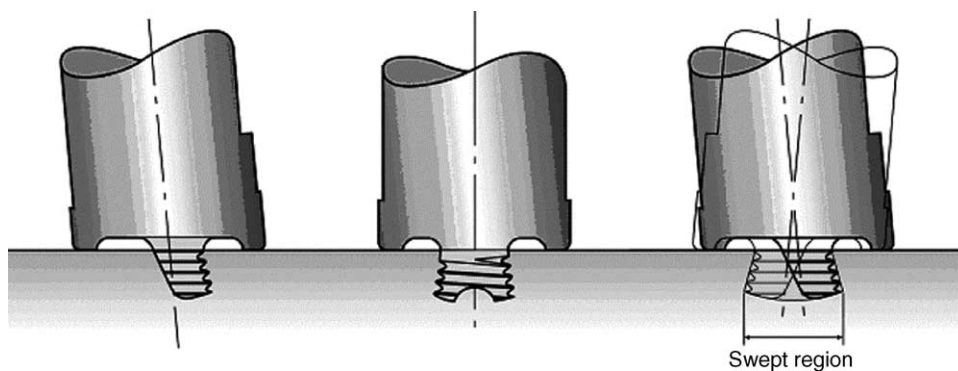


Fig. 5. A-Skew™ tool developed by The Welding Institute (TWI), UK: (a) side view, (b) front view, and (c) swept region encompassed by skew action (after Thomas et al. [25]).

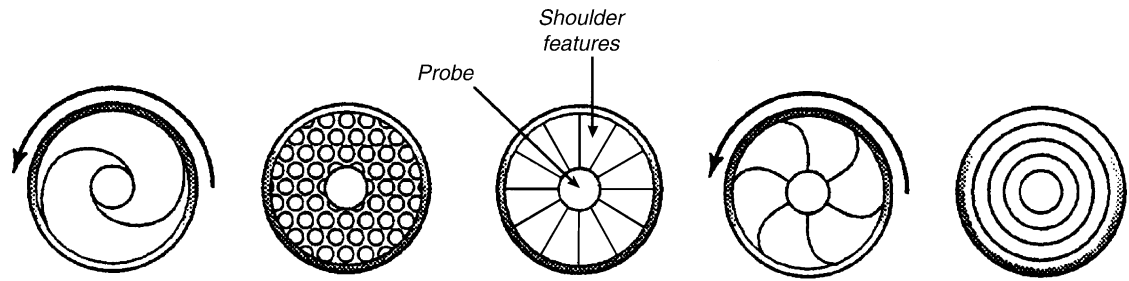


Fig. 6. Tool shoulder geometries, viewed from underneath the shoulder (Copyright © 2001, TWI Ltd) (after Thomas et al. [24]).

(FEA), can be used to visualize the material flow and calculate axial forces. Several companies have indicated internal R&D efforts in friction stir welding conferences, but no open literature is available on such efforts and outcome. It is important to realize that generalization of microstructural development and influence of processing parameters is difficult in absence of the tool information.

2.2. Welding parameters

For FSW, two parameters are very important: tool rotation rate (ω , rpm) in clockwise or counterclockwise direction and tool traverse speed (v , mm/min) along the line of joint. The rotation of tool results in stirring and mixing of material around the rotating pin and the translation of tool moves the stirred material from the front to the back of the pin and finishes welding process. Higher tool rotation rates generate higher temperature because of higher friction heating and result in more intense stirring and mixing of material as will be discussed later. However, it should be noted that frictional coupling of tool surface with workpiece is going to govern the heating. So, a monotonic increase in heating with increasing tool rotation rate is not expected as the coefficient of friction at interface will change with increasing tool rotation rate.

In addition to the tool rotation rate and traverse speed, another important process parameter is the angle of spindle or tool tilt with respect to the workpiece surface. A suitable tilt of the spindle towards trailing direction ensures that the shoulder of the tool holds the stirred material by threaded pin and move material efficiently from the front to the back of the pin. Further, the insertion depth of pin into the workpieces (also called target depth) is important for producing sound welds with smooth tool shoulders. The insertion depth of pin is associated with the pin height. When the insertion depth is too shallow, the shoulder of tool does not contact the original workpiece surface. Thus, rotating shoulder cannot move the stirred material efficiently from the front to the back of the pin, resulting in generation of welds with inner channel or surface groove. When the insertion depth is too deep, the shoulder of tool plunges into the workpiece creating excessive flash. In this case, a significantly concave weld is produced, leading to local thinning of the welded plates. It should be noted that the recent development of ‘scrolled’ tool shoulder allows FSW with 0° tool tilt. Such tools are particularly preferred for curved joints.

Preheating or cooling can also be important for some specific FSW processes. For materials with high melting point such as steel and titanium or high conductivity such as copper, the heat produced by friction and stirring may be not sufficient to soften and plasticize the material around the rotating tool. Thus, it is difficult to produce continuous defect-free weld. In these cases, preheating or additional external heating source can help the material flow and increase the process window. On the other hand, materials with lower melting point such as aluminum and magnesium, cooling can be used to reduce

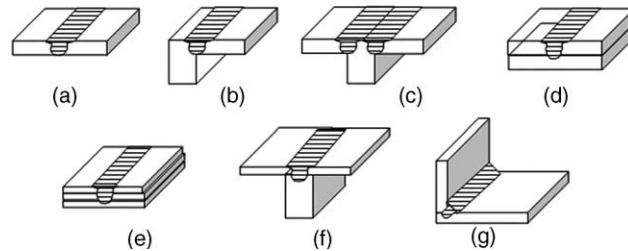


Fig. 7. Joint configurations for friction stir welding: (a) square butt, (b) edge butt, (c) T butt joint, (d) lap joint, (e) multiple lap joint, (f) T lap joint, and (g) fillet joint.

extensive growth of recrystallized grains and dissolution of strengthening precipitates in and around the stirred zone.

2.3. Joint design

The most convenient joint configurations for FSW are butt and lap joints. A simple square butt joint is shown in Fig. 7a. Two plates or sheets with same thickness are placed on a backing plate and clamped firmly to prevent the abutting joint faces from being forced apart. During the initial plunge of the tool, the forces are fairly large and extra care is required to ensure that plates in butt configuration do not separate. A rotating tool is plunged into the joint line and traversed along this line when the shoulder of the tool is in intimate contact with the surface of the plates, producing a weld along abutting line. On the other hand, for a simple lap joint, two lapped plates or sheets are clamped on a backing plate. A rotating tool is vertically plunged through the upper plate and into the lower plate and traversed along desired direction, joining the two plates (Fig. 7d). Many other configurations can be produced by combination of butt and lap joints. Apart from butt and lap joint configurations, other types of joint designs, such as fillet joints (Fig. 7g), are also possible as needed for some engineering applications.

It is important to note that no special preparation is needed for FSW of butt and lap joints. Two clean metal plates can be easily joined together in the form of butt or lap joints without any major concern about the surface conditions of the plates.

3. Process modeling

FSW/FSP results in intense plastic deformation and temperature increase within and around the stirred zone. This results in significant microstructural evolution, including grain size, grain boundary character, dissolution and coarsening of precipitates, breakup and redistribution of dispersoids, and texture. An understanding of mechanical and thermal processes during FSW/FSP is needed for optimizing process parameters and controlling microstructure and properties of welds. In this section, the present understanding of mechanical and thermal processes during FSW/FSP is reviewed.

3.1. Metal flow

The material flow during friction stir welding is quite complex depending on the tool geometry, process parameters, and material to be welded. It is of practical importance to understand the material flow characteristics for optimal tool design and obtain high structural efficiency welds. This has led to

numerous investigations on material flow behavior during FSW. A number of approaches, such as tracer technique by marker, welding of dissimilar alloys/metals, have been used to visualize material flow pattern in FSW. In addition, some computational methods including FEA have been also used to model the material flow.

3.1.1. Experimental observations

The material flow is influenced very significantly by the tool design. Therefore, any generalization should be treated carefully. Also, most of the studies do not report tool design and all process conditions. Therefore, differences among various studies cannot be easily discerned. To develop an overall pattern, in this review a few studies are specifically summarized and then some general trends are presented.

3.1.1.1. Tracer technique by marker. One method of tracking the material flow in a friction stir weld is to use a marker material as a tracer that is different from the material being welded. In the past few years, different marker materials, such as aluminum alloy that etch differently from the base metal [28–30], copper foil [31], small steel shots [32,33], Al–SiC_p and Al–W composites [3,34], and tungsten wire [35], have been used to track the material flow during FSW.

Reynolds and coworkers [28–30] investigated the material flow behavior in FSW 2195Al-T8 using a marker insert technique (MIT). In this technique, markers made of 5454Al-H32 were embedded in the path of the rotating tool as shown in Fig. 8 and their final position after welding was revealed by milling off successive slices of 0.25 mm thick from the top surface of the weld, etching with Keller’s reagent, and metallographic examination. Further, a projection of the marker positions onto a vertical plane in the welding direction was constructed. These investigations revealed the following. First, all welds exhibited some common flow patterns. The flow was not symmetric about the weld centerline. Bulk of the marker material moved to a final position behind its original position and only a small amount of the material on the advancing side was moved to a final position in front of its original position. The backward movement of material was limited to one pin diameter behind its original position. Second, there is a well-defined interface between the advancing and retreating sides, and the material was not really stirred across the interface during the FSW process, at least not on a macroscopic level. Third, material was pushed downward on the advancing side and moved toward the top at the retreating side within the pin diameter. This indicates that the “stirring” of material occurred only at the top of the weld where the material transport was directly influenced by the rotating tool shoulder that moved material from the retreating side around the pin to the advancing

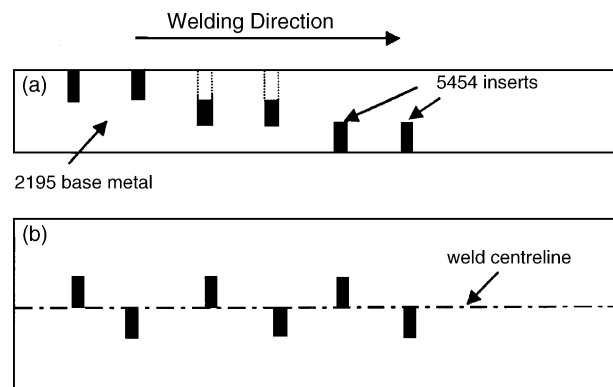


Fig. 8. Schematic drawing of the marker configuration (after Reynolds [29]).

side. Fourth, the amount of vertical displacement of the retreating side bottom marker was inversely proportional to the weld pitch (welding speed/rotation rate, i.e. the tool advance per rotation). Fifth, the material transport across the weld centerline increased with increasing the pin diameter at a constant tool rotation rate and traverse speed. Based on these observations, Reynolds et al. [29,30] suggested that the friction stir welding process can be roughly described as an in situ extrusion process wherein the tool shoulder, the pin, the weld backing plate, and cold base metal outside the weld zone form an “extrusion chamber” which moves relative to the workpiece. They concluded that the extrusion around the pin combined with the stirring action at the top of the weld created within the pin diameter a secondary, vertical, circular motion around the longitudinal axis of the weld.

Guerra et al. [31] studied the material flow of FSW 6061Al by means of a faying surface tracer and a pin frozen in place at the end of welding. For this technique, weld was made with a thin 0.1 mm high-purity Cu foil along the faying surface of the weld. After a stable weld had been established, the pin rotation and specimen translation were manually stopped to produce a pin frozen into the workpiece. Plan view and transverse metallographic sections were examined after etching. Based on the microstructural examinations, Guerra et al. [31] concluded that the material was moved around the pin in FSW by two processes. First, material on the advancing side front of a weld entered into a zone that rotates and advances simultaneously with the pin. The material in this zone was very highly deformed and sloughed off behind the pin in arc shaped features. This zone exhibited high Vicker’s microhardness of 95. Second, material on the retreating front side of the pin extruded between the rotational zone and the parent metal and in the wake of the weld fills in between material sloughed off from the rotational zone. This zone exhibited low Vicker’s microhardness of 35. Further, they pointed out that material near the top of the weld (approximately the upper one-third) moved under the influence of the shoulder rather than the threads on the pin.

Colligan [32,33] studied the material flow behavior during FSW of aluminum alloys by means of steel shot tracer technique and “stop action” technique. For the steel shot tracer technique, a line of small steel balls of 0.38 mm diameter were embedded along welding direction at different positions within butt joint welds of 6061Al-T6 and 7075Al-T6 plates. After stopping welding, each weld was subsequently radiographed to reveal the distribution of the tracer material around and behind the pin. The “stop action” technique involved terminating friction stir welding by suddenly stopping the forward motion of the welding tool and simultaneously retracting the tool at a rate that caused the welding tool pin to unscrew itself from the weld, leaving the material within the threads of the pin intact and still attached to the keyhole. By sectioning the keyhole, the flow pattern of material in the region immediately within the threads of the welding tool was revealed. These investigations revealed the following important observations. First, the distribution of the tracer steel shots can be divided into two general categories: chaotical and continuous distribution. In the regions near top surface of the weld, individual tracer elements were scattered in an erratic way within a relatively broad zone behind the welding tool pin, i.e., chaotical distribution. The chaotically deposited tracer steel shots had moved to a greater depth from their original position. In other regions of the weld, the initial continuous line of steel shots was reorientated and deposited as a roughly continuous line of steel shot behind the pin, i.e., continuous distribution. However, the tracer steel shots were found to be little closer to the upper surface of the weld. Second, in the leading side of the keyhole, the thread form gradually developed from curls of aluminum. The continuous downward motion of the thread relative to the forward advance of the pin caused the material captured inside the thread space to be deposited behind the pin. Based on these observations, Colligan [32,33] concluded that not all the material in the tool path was actually stirred and rather a large amount of the material was simply extruded around the retreating side of the welding tool pin and deposited behind. However, it should be pointed out that if the marker

material has different flow strength and density, it can create uncertainty about the accuracy of the conclusions.

London et al. [34] investigated material flow in FSW of 7050Al-T7451 monitored with 6061Al–30 vol.% SiC_p and Al–20 vol.% W composite markers. The markers with a cross-section of 0.79 mm × 0.51 mm were placed at the center on the midplane of the workpiece (MC) and at the advancing side on the midplane (MA). In each FSW experiment, the forward progress of the tool was stopped while in the process of spreading the marker. The distribution of marker material was examined by metallography and X-ray. Based on experimental observations, London et al. [34] suggested that the flow of the marker in the FSW zone goes through the following sequence of events. First, material ahead of the pin is significantly uplifted because of the 3° tilt of the tool, which creates a “plowing action” of the metal ahead of the weld. Second, following this uplift, the marker is sheared around the periphery of the pin while at the same time it is being pushed downward in the plate because of the action of the threads. Third, marker material is dropped off behind the pin in “streaks” which correspond to the geometry of the threads and specific weld parameters used to create these welds. Furthermore, London et al. [34] showed that the amount of material deformation in the FSW weld depends on the locations relative to the pin. Markers on the advancing side of the weld are distributed over a much wider region in the wake of the weld than markers that begin at the weld centerline.

3.1.1.2. Flow visualization by FSW of dissimilar materials. In addition to the tracer technique, several studies have used friction stir welding of dissimilar metals for visualizing the complex flow phenomenon. Midling [35] investigated the influence of the welding speed on the material flow in welds of dissimilar aluminum alloys. He was the first to report on interface shapes using images of the microstructure. However, information on flow visualization was limited to the interface between dissimilar alloys.

Ouyang and Kovacevic [36] examined the material flow behavior in friction stir butting welding of 2024Al to 6061Al plates of 12.7 mm thick. Three different regions were revealed in the welded zone. The first was the mechanically mixed region characterized by the relatively uniformly dispersed particles of different alloy constituents. The second was the stirring-induced plastic flow region consisting of alternative vortex-like lamellae of the two aluminum alloys. The third was the unmixed region consisting of fine equiaxed grains of the 6061Al alloy. They reported that in the welds the contact between different layers is intimate, but the mixing is far from complete. However, the bonding between the two aluminum alloys was complete. Further, they attributed the vortex-like structure and alternative lamellae to the stirring action of the threaded tool, in situ extrusion, and traverse motion along the welding direction.

Murr and co-workers [8,10,37,38] investigated the solid-state flow visualization in friction stir butt welding of 2024Al to 6061Al and copper to 6061Al. The material flow was described as a chaotic–dynamic intercalation microstructures consisting of vortex-like and swirl features. They further suggested that the complex mixing and intercalation of dissimilar metals in FSW is essentially the same as the microstructures characteristic of mechanically alloyed systems. On the other hand, a recent investigation on friction stir lap welding of 2195Al to 6061Al revealed that there is large vertical movement of material within the rotational zone caused by the wash and backwash of the threads [31]. Guerra et al. [31] have stated that material entering this zone followed an unwound helical trajectory formed by the rotational motion, the vertical flow, and the translational motion of the pin.

3.1.1.3. Microstructural observations. The idea that the FSW is likened to an extrusion process is also supported by Krishnan [39]. Krishnan [39] investigated the formation of onion rings in friction stir welds of 6061Al and 7075Al alloys by using different FSW parameters. Onion rings found in the

welded zone is a direct evidence of characteristic material transport phenomena occurring during FSW. It was suggested that the friction stir welding process can be thought to be simply extruding one layer of semicylinder in one rotation of the tool and a cross-sectional slice through such a set of semicylinder results in the familiar onion ring structure. On the other hand, Biallas et al. [40] suggested that the formation of onion rings was attributed to the reflection of material flow approximately at the imaginary walls of the groove that would be formed in the case of regular milling of the metal. The induced circular movement leads to circles that decrease in radii and form the tube system. In this case, it is believed that there should be thorough mixing of material in the nugget region. Although microstructural examinations revealed an abrupt variation in grain size and/or precipitate density at these rings [41,42], it is noted that the understanding of formation of onion rings is far from complete and an insight into the mechanism of onion ring formation would shed light on the overall material flow occurring during FSW.

Recently, Ma et al. [43] conducted a study on microstructural modification of cast A356 via friction stir processing. As-cast A356 plates were subjected to friction stir processing by using different tool geometries and FSP parameters. Fig. 9 shows the optical micrographs of as-cast A356 and FSP sample prepared using a standard threaded pin and tool rotation rate of 900 rpm and traverse speed of 203 mm/min. The as-cast A356 was characterized by coarse acicular Si particles with an aspect ratio of up to 25, coarse primary aluminum dendrites with an average size of $\sim 100\ \mu\text{m}$, and porosity of $\sim 50\ \mu\text{m}$ diameter (Fig. 9a). The acicular Si particles were preferentially distributed along the boundaries of the primary aluminum dendrites, i.e., the distribution of Si particles in the as-cast A356 was not uniform. FSP resulted in a significant breakup of acicular Si particles and aluminum dendrites. A uniform redistribution of the broken Si particles in the aluminum matrix was also produced. After FSP, the average aspect ratio of Si was reduced to ~ 2.0 . Further, FSP also eliminated the porosity in the as-cast A356. Clearly, the material within the processed zone of the FSP A356 experienced intense stirring and mixing, thereby resulting in breakup of the coarse acicular Si particles and dendrite structure and homogeneous distribution of the Si particles throughout the aluminum matrix. Previous investigations have indicated that the extrusion at high temperature does not reduce the high-aspect-ratio reinforcements to nearly equiaxed particles [44,45]. Besides, as-extruded metal matrix composites are usually characterized by alternative particle-rich bands and particle-free bands [45,46]. Therefore, in the case of FSP A356 under the experimental conditions used, the material flow within the nugget zone cannot be considered as a simple extrusion process.

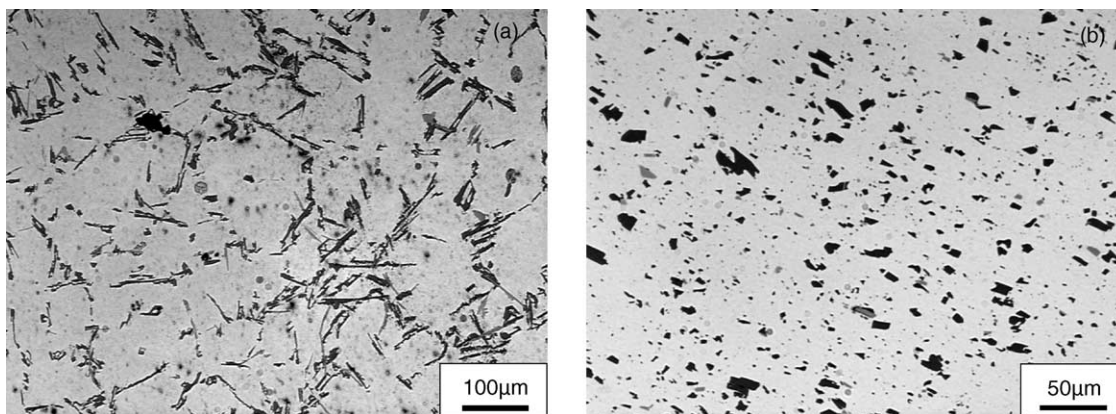


Fig. 9. Optical micrographs showing the microstructure of as-cast and FSP A356 (standard threaded pin, 900 rpm and 203 mm/min) [43].

3.1.2. Material flow modeling

Apart from experimental approaches, a number of studies have been carried out to model the materials flow during FSW using different computational codes [47–53], mathematical modeling tools [54,55], simple geometrical model [56], and metalworking model [57]. These attempts were aimed at understanding the basic physics of the material flow occurring during FSW.

Xu et al. [47] developed two finite element models, the slipping interface model and the frictional contact model, to simulate the FSW process. The simulation predictions of the material flow pattern based on these finite element models compare qualitatively well with an experimentally measured pattern by means of marker insert technique [29,30].

Colegrove and Shercliff [49] modeled the metal flow around profiled FSW tools using a two-dimensional Computational Fluid Dynamics (CFD) code, Fluent. A ‘slip’ model was developed, where the interface conditions were governed by the local shear stresses. The two-dimensional modeling resulted in the following important findings. First, flow behavior obtained by the slip model is significantly different from that obtained by the common assumption of material stick. The slip model revealed significant differences in flow with different tool shapes, which is not evident with the conventional stick model. Second, the deformation region for the slip model is much smaller on the advancing side than retreating side. Third, the material in the path of the pin is swept round the retreating side of the tool. This characteristic of the model is supported by flow visualization experiments by London et al. [3,34] and Guerra et al. [31]. Fourth, the streamlines show a bulge behind the tool, and the dragging of material behind the pin on the advancing side. This correlated well with previous embedded marker experiments by Reynolds and co-workers [29,30].

Smith et al. [50] and Bendzsak and Smith [51] developed a thermo-mechanical flow model (STIR-3D). The principles of fluid mechanics were applied in this model. It assumes viscous heat dissipation as opposed to frictional heating. This model uses tool geometry, alloy type, tool rotation speed, tool position and travel speed as inputs and predicts the material flow profiles, process loads, and thermal profiles. It was indicated that three quite distinct flow regimes were formed below the tool shoulder, namely, (a) a region of rotation immediately below the shoulder where flow occurred in the direction of tool rotation, (b) a region where material is extruded past the rotating tool and this occurred towards the base of the pin, and (c) a region of transition in between regions (a) and (b) where the flow had chaotic behavior.

Askari et al. [52] adapted a CTH code [58] that is a three-dimensional code capable of solving time-dependent equations of continuum mechanics and thermodynamics. This model predicts important fields like strain, strain rate and temperature distribution. The validity of the model was verified by previous marker insert technique [3,34]. Goetz and Jata [53] used a two-dimensional FEM code, DEFORM [59], to simulate material flow in FSW of 1100Al and Ti–6Al–4V alloys. Non-isothermal simulation showed that highly localized metal flow is likely to occur during FSW. The movement of tracking points in these simulations shows metal flow around the tool from one side to the other, creating a weld. The simulations predict strain rates of 2–12 s⁻¹ and strains of 2–5 in the zone of localized flow.

Stewart et al. [54] proposed two models for FSW process, mixed zone model and single slip surface model. Mixed zone model assumes that the metal in the plastic zone flows in a vortex system at an angular velocity of the tool at the tool–metal interface and the angular velocity drops to zero at the edge of the plastic zone. In the single slip surface model, the principal rotational slip takes place at a contracted slip surface outside the tool–workpiece interface. It was demonstrated that using a limited region of slip, predictions of the thermal field, the force and the weld region shape were in agreement with experimental measurement. Nunes [55] developed a detailed mathematical model of wiping flow transfer. This model is found to have the in-built capability to describe the tracer experiments.

Recently, Arbegast [57] suggested that the resultant microstructure and metal flow features of a friction stir weld closely resemble hot worked microstructure of typical aluminum extrusion and forging. Therefore, the FSW process can be modeled as a metalworking process in terms of five conventional metal working zones: (a) preheat, (b) initial deformation, (c) extrusion, (d) forging, and (e) post heat/cool down (Fig. 10). In the preheat zone ahead of the pin, temperature rises due to the frictional heating of the rotating tool and adiabatic heating because of the deformation of material. The thermal properties of material and the traverse speed of the tool govern the extent and heating rate of this zone. As the tool moves forward, an initial deformation zone forms when material is heated to above a critical temperature and the magnitude of stress exceeds the critical flow stress of the material, resulting in material flow. The material in this zone is forced both upwards into the shoulder zone and downwards into the extrusion zone, as shown in Fig. 10. A small amount of material is captured in the swirl zone beneath the pin tip where a vortex flow pattern exists. In the extrusion zone with a finite width, material flows around the pin from the front to the rear. A critical isotherm on each side of the tool defines the width of the extrusion zone where the magnitudes of stress and temperature are insufficient to allow metal flow. Following the extrusion zone is the forging zone where the material from the front of the tool is forced into the cavity left by the forward moving pin under hydrostatic pressure conditions. The shoulder of the tool helps to constrain material in this cavity and also applies a downward forging force. Material from shoulder zone is dragged across the joint from the retreating side toward the advancing side. Behind the forging zone is the post heat/cool zone where the material cools under either passive or forced cooling conditions. Arbegast [57] developed a simple approach to metal flow modeling of the extrusion zone using mass balance considerations that reveals a relationship between tool geometry, operating parameters, and flow stress of the materials being joined. It was indicated that the calculated temperature, width of the extrusion zone, strain rate, and extrusion pressure are consistent with experimental observations.

In summary, the material flow during FSW is complicated and the understanding of deformation process is limited. It is important to point out that there are many factors that can influence the material flow during FSW. These factors include tool geometry (pin and shoulder design, relative dimensions of pin and shoulder), welding parameters (tool rotation rate and direction, i.e., clockwise or counter-clockwise, traverse speed, plunge depth, spindle angle), material types, workpiece temperature, etc. It is very likely that the material flow within the nugget during FSW consists of several independent deformation processes.

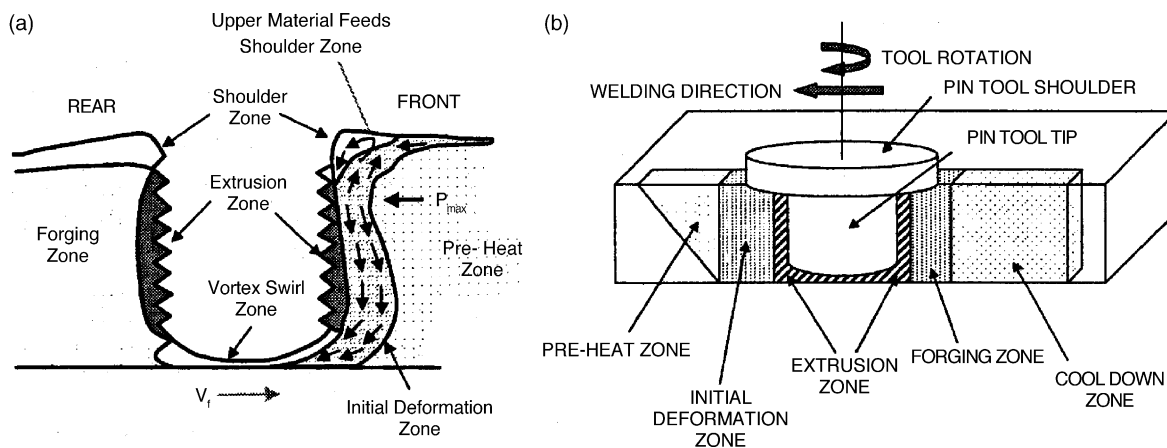


Fig. 10. (a) Metal flow patterns and (b) metallurgical processing zones developed during friction stir welding (after Arbegast [57]).

3.2. Temperature distribution

FSW results in intense plastic deformation around rotating tool and friction between tool and workpieces. Both these factors contribute to the temperature increase within and around the stirred zone. Since the temperature distribution within and around the stirred zone directly influences the microstructure of the welds, such as grain size, grain boundary character, coarsening and dissolution of precipitates, and resultant mechanical properties of the welds, it is important to obtain information about temperature distribution during FSW. However, temperature measurements within the stirred zone are very difficult due to the intense plastic deformation produced by the rotation and translation of tool. Therefore, the maximum temperatures within the stirred zone during FSW have been either estimated from the microstructure of the weld [4,5,60] or recorded by embedding thermocouple in the regions adjacent to the rotating pin [41,61–63].

An investigation of microstructural evolution in 7075Al-T651 during FSW by Rhodes et al. [4] showed dissolution of larger precipitates and reprecipitation in the weld center. Therefore, they concluded that maximum process temperatures are between about 400 and 480 °C in an FSW 7075Al-T651. On the hand, Murr and co-workers [5,60] indicated that some of the precipitates were not dissolved during welding and suggested that the temperature rises to roughly 400 °C in an FSW 6061Al. Recently, Sato et al. [61] studied the microstructural evolution of 6063Al during FSW using transmission electron microscopy (TEM) and compared it with that of simulated weld thermal cycles. They reported that the precipitates within the weld region (0–8.5 mm from weld center) were completely dissolved into aluminum matrix. By comparing with the microstructures of simulated weld thermal cycles at different peak temperatures, they concluded that the regions 0–8.5, 10, 12.5, and 15 mm away from the friction stir weld center were heated to temperatures higher than 402, 353, 302 °C and lower than 201 °C, respectively.

Recently, Mahoney et al. [41] conducted friction stir welding of 6.35 mm thick 7075Al-T651 plate and measured the temperature distribution around the stirred zone both as a function of distance from the stirred zone and through the thickness of the sheet. Fig. 11 shows the peak temperature distribution adjacent to the stirred zone. Fig. 11 reveals three important observations. First, maximum temperature was recorded at the locations close to the stirred zone, i.e., the edge of the stirred zone, and the temperature decreased with increasing distance from the stirred zone. Second, the temperature at

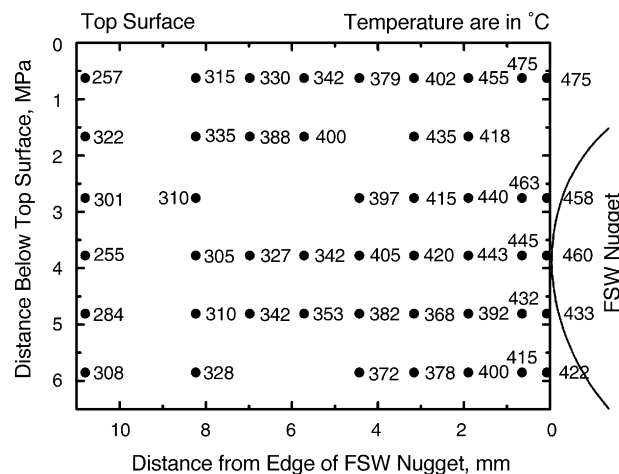


Fig. 11. Peak temperature distribution adjacent to a friction stir weld in 7075Al-T651. The line on the right side of figure shows the nugget boundary (after Mahoney et al. [41]).

the edge of the stirred zone increased from the bottom surface of the plate to the top surface. Third, a maximum temperature of 475 °C was recorded near the corner between the edge of the stirred zone and the top surface. This temperature is believed to exceed the solution temperature for the hardening precipitates in 7075Al-T651 [64–66]. Based on these results the temperature within the stirred zone is likely to be above 475 °C. However, the maximum temperature within the stirred zone should be lower than the melting point of 7075Al because no evidence of material melting was observed in the weld [4,41].

More recently, an attempt was made by Tang et al. [62] to measure the heat input and temperature distribution within friction stir weld by embedding thermocouples in the region to be welded. 6061Al-T6 aluminum plates with a thickness of 6.4 mm were used. They embedded thermocouples in a series of small holes of 0.92 mm diameter at different distances from weld seam drilled into the back surface of the workpiece. Three depths of holes (1.59, 3.18, and 4.76 mm) were used to measure the temperature field at one quarter, one half, and three quarter of the plate thickness. They reported that the thermocouple at the weld center was not destroyed by the pin during welding but did change position slightly due to plastic flow of material ahead of the pin [62]. Fig. 12 shows the variation of the peak temperature with the distance from the weld centerline for various depths below the top surface. Three important observations can be made from this plot. First, maximum peak temperature was recorded at the weld center and with increasing distance from the weld centerline, the peak temperature decreased. At a tool rotation rate of 400 rpm and a traverse speed of 122 mm/min, a peak temperature of ~450 °C was observed at the weld center one quarter from top surface. Second, there is a nearly isothermal region ~4 mm from the weld centerline. Third, the peak temperature gradient in the thickness direction of the welded joint is very small within the stirred zone and between 25 and 40 °C in the region away from the stirred zone. This indicates that the temperature distribution within the stirred zone is relatively uniform. Tang et al. [62] further investigated the effect of weld pressure and tool rotation rate on the temperature field of the weld zone. It was reported that increasing both tool rotation rate and weld pressure resulted in an increase in the weld temperature. Fig. 13 shows the effect of tool rotation rate on the peak temperature as a function of distance from the weld centerline. Clearly, within the weld zone the peak temperature increased by almost 40 °C with increasing tool rotation rate from 300 to 650 rpm, whereas it only increased by 20 °C when the tool rotation rate increased from 650 to 1000 rpm, i.e., the rate of temperature increase is lower at higher

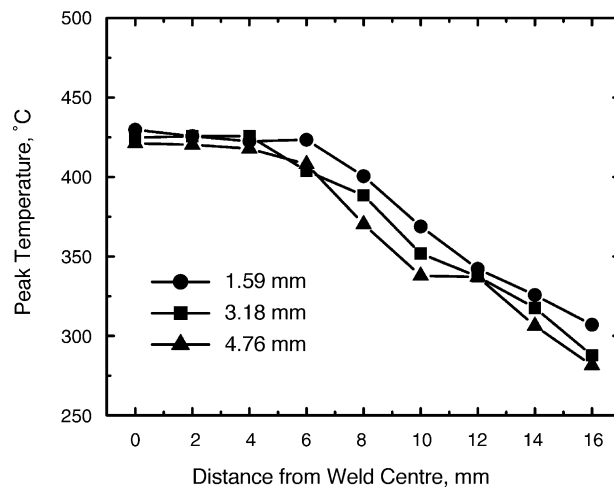


Fig. 12. Effect of depth on peak temperature as a function of distance from weld centerline for a 6061Al-T6 FSW weld made at 400 rpm and 120 mm/min traverse speed (after Tang et al. [62]).

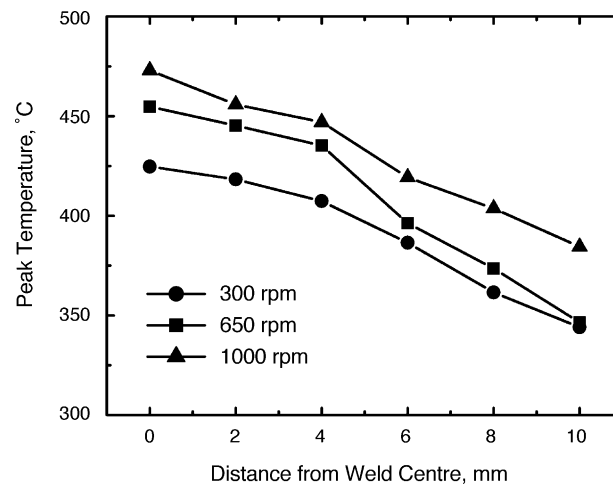


Fig. 13. Effect of tool rotation rate on peak temperature as a function of distance from weld centerline for a 6061Al-T6 FSW weld made at 120 mm/min traverse speed (after Tang et al. [62]).

tool rotation rates. Furthermore, Tang et al. [62] studied the effect of shoulder on the temperature field by using two tools with and without pin. The shoulder dominated the heat generation during FSW (Fig. 14). This was attributed to the fact that the contact area and vertical pressure between the shoulder and workpiece is much larger than those between the pin and workpiece, and the shoulder has higher linear velocity than the pin with smaller radius [62]. Additionally, Tang et al. [62] showed that the thermocouples placed at equal distances from the weld seam but on opposite sides of the weld showed no significant differences in the temperature.

Similarly, Kwon et al. [63], Sato et al. [67], and Hashimoto et al. [68] also measured the temperature rise in the weld zone by embedding thermocouples in the regions adjacent to the rotating pin. Kwon et al. [63] reported that in FSW 1050Al, the peak temperature in the FSP zone increased linearly from 190 to 310 °C with increasing tool rotation rate from 560 to 1840 rpm at a constant tool traverse speed of 155 mm/min. An investigation by Sato et al. [67] indicated that in FSW 6063Al, the peak temperature of FSW thermal cycle increased sharply with increasing tool rotation rate from 800

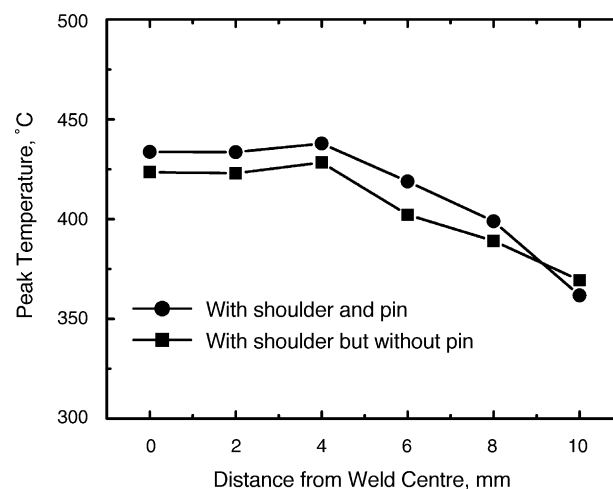


Fig. 14. Variation of peak temperature with distance from weld centerline for a 6061Al-T6 FSW weld made with and without pin (400 rpm and 120 mm/min traverse speed) (after Tang et al. [62]).

to 2000 rpm at a constant tool traverse speed of 360 mm/min, and above 2000 rpm, however, it rose gradually with increasing rotation rate from 2000 to 3600 rpm. Peak temperature of $>500\text{ }^{\circ}\text{C}$ was recorded at a high tool rotation rate of 3600 rpm. Hashimoto et al. [68] reported that the peak temperature in the weld zone increases with increasing the ratio of tool rotation rate/traverse speed for FSW of 2024Al-T6, 5083Al-O and 7075Al-T6 (Fig. 15). A peak temperature $>550\text{ }^{\circ}\text{C}$ was observed in FSW 5083Al-O at a high ratio of tool rotation rate/traverse speed.

In a recent investigation, a numerical three-dimensional heat flow model for friction stir welding of age hardenable aluminum alloy has been developed by Frigaad et al. [69], based on the method of finite differences. The average heat input per unit area and time according to their model is [69]:

$$q_0 = \frac{4}{3}\pi^2 \mu P \omega R^3, \quad (1)$$

where q_0 is the net power (W), μ the friction coefficient, P the pressure (Pa), ω the tool rotational speed (rot/s) and R is the tool radius (m). Frigaad et al. [69] suggested that the tool rotation rate and shoulder radius are the main process variables in FSW, and the pressure P cannot exceed the actual flow stress of the material at the operating temperature if a sound weld without depressions is to be obtained. The process model was compared with in situ thermocouple measurements in and around the FSW zone. FSW of 6082Al-T6 and 7108Al-T79 was performed at constant tool rotation rate of 1500 rpm and a constant welding force of 7000 N, at three welding speeds of 300, 480, and 720 mm/min. They revealed three important observations. First, peak temperature of above $\sim 500\text{ }^{\circ}\text{C}$ was recorded in the FSW zone. Second, peak temperature decreased with increasing traverse speeds from 300 to 720 mm/min. Third, the three-dimensional numerical heat flow model yields a temperature–time pattern that is consistent with that observed experimentally. Similarly, three-dimensional thermal model based on finite element analysis developed by Chao and Qi [70] and Khandkar and Khan [71] also showed reasonably good match between the simulated temperature profiles and experimental data for both butt and overlap FSW processes.

The effect of FSW parameters on temperature was further examined by Arbegast and Hartley [72]. They reported that for a given tool geometry and depth of penetration, the maximum temperature was observed to be a strong function of the rotation rate (ω , rpm) while the rate of heating was a strong function of the traverse speed (v , rpm). It was also noted that there was a slightly higher temperature on the advancing side of the joint where the tangential velocity vector direction was same as the forward

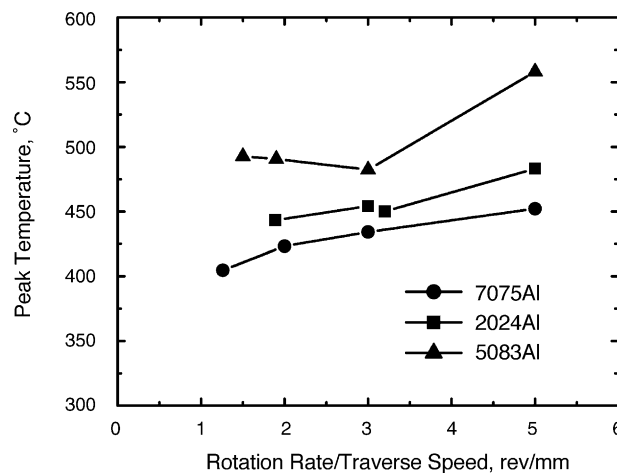


Fig. 15. Effect of tool rotation rate/traverse speed (ω/v) ratio on peak temperature of FSW 2024Al-T6, 5083Al-O, and 7075Al-T6 (after Hashimoto et al. [68]).

velocity vector. They measured the average maximum temperature on 6.35 mm aluminum plates as a function of the pseudo-“heat index w ($w = \omega^2/\nu$)”. It was demonstrated that for several aluminum alloys a general relationship between maximum welding temperature (T , °C) and FSW parameters (ω , ν) can be explained by

$$\frac{T}{T_m} = K \left(\frac{\omega^2}{\nu \times 10^4} \right)^\alpha, \quad (2)$$

where the exponent α was reported to range from 0.04 to 0.06, the constant K is between 0.65 and 0.75, and T_m (°C) is the melting point of the alloy. The maximum temperature observed during FSW of various aluminum alloys is found to be between $0.6T_m$ and $0.9T_m$, which is within the hot working temperature range for those aluminum alloys. Furthermore, the temperature range is generally within the solution heat-treatment temperature range of precipitation-strengthened aluminum alloys.

Recently, Schmidt et al. [73] have developed an analytical model for the heat generation in FSW. The important difference between this model and the previous models is the choice of sticking and sliding contact conditions. The expressions for total heat generation for sticking, sliding, and partial sliding/sticking conditions, respectively, are

$$Q_{\text{total, sticking}} = \frac{2}{3} \pi \frac{\sigma_{\text{yield}}}{\sqrt{3}} \omega ((R_{\text{shoulder}}^3 - R_{\text{probe}}^3)(1 + \tan \alpha) + R_{\text{probe}}^3 + 3R_{\text{probe}}^2 H_{\text{probe}}), \quad (3a)$$

$$Q_{\text{total, sliding}} = \frac{2}{3} \pi \mu p \omega ((R_{\text{shoulder}}^3 - R_{\text{probe}}^3)(1 + \tan \alpha) + R_{\text{probe}}^3 + 3R_{\text{probe}}^2 H_{\text{probe}}), \quad (3b)$$

$$Q_{\text{total}} = \frac{2}{3} \pi \left(\delta \frac{\sigma_{\text{yield}}}{\sqrt{3}} + (1 - \delta) \mu p \right) \omega ((R_{\text{shoulder}}^3 - R_{\text{probe}}^3)(1 + \tan \alpha) + R_{\text{probe}}^3 + 3R_{\text{probe}}^2 H_{\text{probe}}), \quad (3c)$$

where Q is the total heat generation (W), σ_{yield} the yield strength (Pa), ω the tool angular rotation rate (rad/s), R_{shoulder} the tool shoulder radius (m), R_{probe} the tool probe radius (m), α the tool shoulder cone angle (°), H_{probe} the tool probe height (m), p the contact pressure (Pa), and δ is the contact state variable. Schmidt et al. [73] verified the model using 2024Al-T3 alloy. They noted that the analytical heat generation estimate correlates with the experimental heat generation. The experimental heat generation was not proportional to the experimental plunge force. Based on this they suggested that sticking condition must be present at the tool/matrix interface. It should be noted, however, that the experiments were only performed at a rotational rate of 400 rpm and a welding speed of 120 mm/min.

In summary, many factors influence the thermal profiles during FSW. From numerous experimental investigations and process modeling, we conclude the following. First, maximum temperature rise within the weld zone is below the melting point of aluminum. Second, tool shoulder dominates heat generation during FSW. Third, maximum temperature increases with increasing tool rotation rate at a constant tool traverse speed and decreases with increasing traverse speed at a constant tool rotation rate. Furthermore, maximum temperature during FSW increases with increasing the ratio of tool rotation rate/traverse speed. Fourth, maximum temperature rise occurs at the top surface of weld zone. Various theoretical or empirical models proposed so far present different pseudo-heat index. The experimental verification of these models is very limited and attempts to correlate various data sets

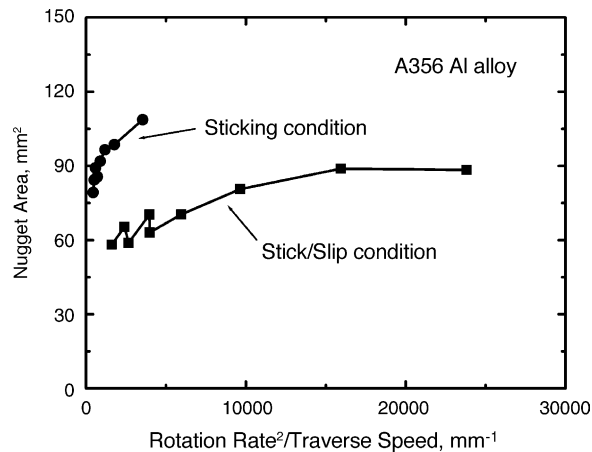


Fig. 16. Variation of nugget cross-section area with pseudo-heat index [74].

with models for this review did not show any general trend. The overall picture includes frictional heating and adiabatic heating. The frictional heating depends on the surface velocity and frictional coupling (coefficient of friction). Therefore, the temperature generation should increase from center of the tool shoulder to the edge of the tool shoulder. The pin should also provide some frictional heating and this aspect has been captured in the model of Schmidt et al. [73]. In addition, the adiabatic heating is likely to be maximum at the pin and tool shoulder surface and decrease away from the interface. Currently, the theoretical models do not integrate all these contributions. Recently, Sharma and Mishra [74] have observed that the nugget area changes with pseudo-heat index (Fig. 16). The results indicate that the frictional condition change from ‘stick’ at lower tool rotation rates to ‘stick/slip’ at higher tool rotation rates. The implications are very important and needs to be captured in theoretical and computational modeling of heat generation.

4. Microstructural evolution

The contribution of intense plastic deformation and high-temperature exposure within the stirred zone during FSW/FSP results in recrystallization and development of texture within the stirred zone [7,8,10,15,41,62,63,75–91] and precipitate dissolution and coarsening within and around the stirred zone [8,10,41,62,63]. Based on microstructural characterization of grains and precipitates, three distinct zones, stirred (nugget) zone, thermo-mechanically affected zone (TMAZ), and heat-affected zone (HAZ), have been identified as shown in Fig. 17. The microstructural changes in various zones

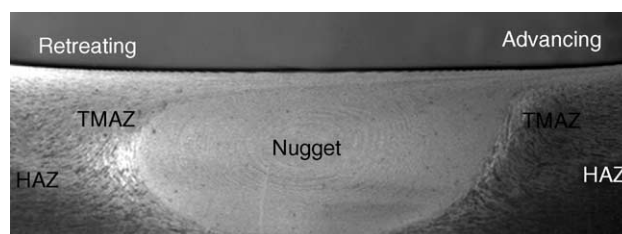


Fig. 17. A typical macrograph showing various microstructural zones in FSP 7075Al-T651 (standard threaded pin, 400 rpm and 51 mm/min).

have significant effect on postweld mechanical properties. Therefore, the microstructural evolution during FSW/FSP has been studied by a number of investigators.

4.1. Nugget zone

Intense plastic deformation and frictional heating during FSW/FSP result in generation of a recrystallized fine-grained microstructure within stirred zone. This region is usually referred to as nugget zone (or weld nugget) or dynamically recrystallized zone (DXZ). Under some FSW/FSP conditions, onion ring structure was observed in the nugget zone (Figs. 17 and 18b). In the interior of the recrystallized grains, usually there is low dislocation density [4,5]. However, some investigators reported that the small recrystallized grains of the nugget zone contain high density of sub-boundaries [61], subgrains [75], and dislocations [92]. The interface between the recrystallized nugget zone and the parent metal is relatively diffuse on the retreating side of the tool, but quite sharp on the advancing side of the tool [93].

4.1.1. Shape of nugget zone

Depending on processing parameter, tool geometry, temperature of workpiece, and thermal conductivity of the material, various shapes of nugget zone have been observed. Basically, nugget zone can be classified into two types, basin-shaped nugget that widens near the upper surface and elliptical nugget. Sato et al. [61] reported the formation of basin-shaped nugget on friction stir welding of 6063Al-T5 plate. They suggested that the upper surface experiences extreme deformation and frictional heating by contact with a cylindrical-tool shoulder during FSW, thereby resulting in generation of basin-shaped nugget zone. On the other hand, Rhodes et al. [4] and Mahoney et al. [41] reported elliptical nugget zone in the weld of 7075Al-T651.

Recently, an investigation was conducted on the effect of FSP parameter on the microstructure and properties of cast A356 [94]. The results indicated that lower tool rotation rate of 300–500 rpm resulted in generation of basin-shaped nugget zone, whereas elliptical nugget zone was observed by FSP at higher tool rotation of >700 rpm (Fig. 18). This indicates that with same tool geometry, different nugget shapes can be produced by changing processing parameters.

Reynolds [29] investigated the relationship between nugget size and pin size. It was reported that the nugget zone was slightly larger than the pin diameter, except at the bottom of the weld where the pin tapered to a hemispherical termination (Fig. 19). Further, it was revealed that as the pin diameter increases, the nugget acquired a more rounded shape with a maximum diameter in the middle of the weld.

4.1.2. Grain size

It is well accepted that the dynamic recrystallization during FSW/FSP results in generation of fine and equiaxed grains in the nugget zone [7,8,10,15,41,62,63,75–91]. FSW/FSP parameters, tool geometry, composition of workpiece, temperature of the workpiece, vertical pressure, and active cooling exert significant influence on the size of the recrystallized grains in the FSW/FSP materials.

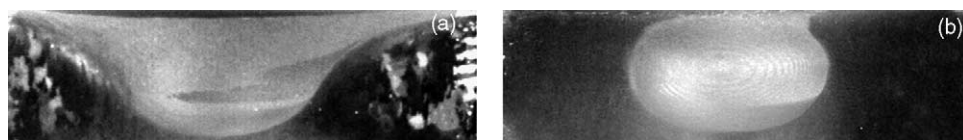


Fig. 18. Effect of processing parameter on nugget shape in FSP A356: (a) 300 rpm, 51 mm/min and (b) 900 rpm, 203 mm/min (standard threaded pin) [94].

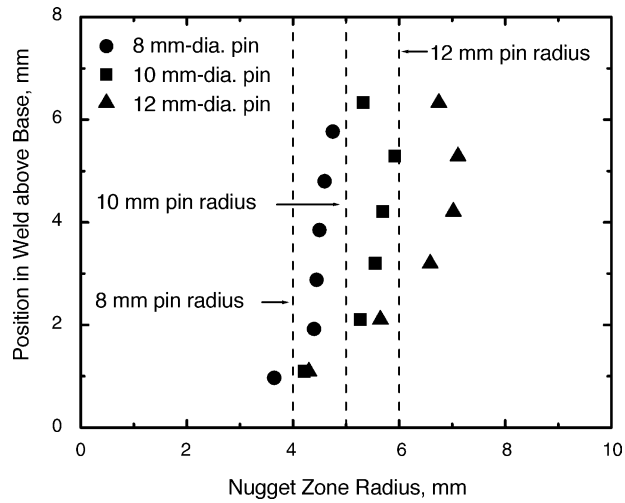


Fig. 19. Effect of pin diameter on nugget size in an FSW 2195Al-T8 (after Reynolds [29]).

Tables 2 and 3 give a summary of the grain size values for various aluminum alloys under different FSW/FSP conditions. The tool geometry was not identified in a number of studies. While the typical recrystallized grain size in the FSW/FSP aluminum alloys is in the micron range (Table 2), ultrafine-grained (UFG) microstructures (average grain size $<1 \mu\text{m}$) have been achieved by using external cooling or special tool geometries (Table 3).

Table 2

A summary of grain size in nugget zone of FSW/FSP aluminum alloys

Material	Plate thickness (mm)	Tool geometry	Rotation rate (rpm)	Traverse speed (mm/min)	Grain size (μm)	Reference
7075Al-T6	6.35	–	–	127	2–4	[4]
6061Al-T6	6.3	Cylindrical	300–1000	90–150	10	[5]
Al–Li–Cu	7.6	–	–	–	9	[6]
7075Al-T651	6.35	Threaded, cylindrical	350, 400	102, 152	3.8, 7.5	[15]
6063Al-T4, T5	4.0	–	360	800–2450	5.9–17.8	[67]
6013Al-T4, T6	4.0	–	1400	400–450	10–15	[75]
1100Al	6.0	Cylindrical	400	60	4	[76]
5054Al	6.0	–	–	–	6	[77]
1080Al-O	4.0	–	–	–	20	[78]
5083Al-O	6.0	–	–	–	4	[78]
2017Al-T6	3	Threaded, cylindrical	1250	60	9–10	[79]
2095Al	1.6	–	1000	126–252	1.6	[80]
Al–Cu–Mg–Ag–T6	4.0	–	850	75	5	[81]
2024Al-T351	6.0	–	–	80	2–3	[82]
7010Al-T7651	6.35	–	180, 450	95	1.7, 6	[83]
7050Al-T651	6.35	–	350	15	1–4	[84]
Al–4Mg–1Zr	10	Threaded, cylindrical	350	102	1.5	[85]
2024Al	6.35	Threaded, cylindrical	200–300	25.4	2.0–3.9	[86]
7475Al	6.35	–	–	–	2.2	[87]
5083Al	6.35	Threaded, cylindrical	400	25.4	6.0	[88]
2519Al-T87	25.4	–	275	101.6	2–12	[89]

Table 3

A summary of ultrafine-grained microstructures produced via FSW/FSP in aluminum alloys

Material	Plate thickness (mm)	Tool geometry	Special cooling	Rotation rate (rpm)	Traverse speed (mm/min)	Grain size (μm)	References
2024Al-T4	6.5	Threaded, cylindrical	Liquid nitrogen	650	60	0.5–0.8	[7]
1050Al	5.0	Conical pin without thread	N/A	560	155	0.5	[63,90,91]
7075Al	2	N/R	Water, methanol, dry ice	1000	120	0.1	[95]
Cast Al–Zn–Mg–Sc	6.7	Threaded, cylindrical	N/A	400	25.4	0.68	[96]

Benavides et al. [7] investigated the effect of the workpiece temperature on the grain size of FSW 2024Al. They [7] reported that decreasing the starting temperature of workpiece from 30 to $-30\text{ }^{\circ}\text{C}$ with liquid nitrogen cooling resulted in a decrease in the peak temperature from 330 to $140\text{ }^{\circ}\text{C}$ at a location 10 mm away from the weld centerline, thereby leading to a reduction in the grain size from 10 to $0.8\text{ }\mu\text{m}$ in FSW 2024Al. Following the same approach, Su et al. [95] prepared bulk nanostructured 7075Al with an average grain size of $\sim 100\text{ nm}$ via FSP, using a mixture of water, methanol and dry ice for cooling the plate rapidly behind the tool. On the other hand, Kwon et al. [63,90,91] adopted a cone-shaped pin with a sharpened tip to reduce the amount of frictional heat generated during FSP of 1050Al. A peak temperature of only $190\text{ }^{\circ}\text{C}$ was recorded in the FSP zone at a tool rotation rate of 560 rpm and a traverse speed of 155 mm/min, which resulted in grain size of $0.5\text{ }\mu\text{m}$. Similarly, Charit and Mishra [96] reported that a grain size of $0.68\text{ }\mu\text{m}$ was produced, by using a small diameter tool with normal threaded pin, in FSP of cast Al–Zn–Mg–Sc at a tool rotation rate of 400 rpm and a traverse speed of 25.4 mm/min. These observations are consistent with the general principles for recrystallization [97] where the recrystallized grain size decreases with decreasing annealing temperature.

More recently, Li et al. [10], Ma et al. [15], Sato et al. [67], and Kwon et al. [63,90,91] studied the influence of processing parameter on the microstructure of FSW/FSP aluminum alloys. It was noted that the recrystallized grain size can be reduced by decreasing the tool rotation rate at a constant tool traverse speed [10,63,67,90,91] or decreasing the ratio of tool rotation rate/traverse speed [15]. For example, Kwon et al. [63,90,91] reported that FSP resulted in generation of the grain size of ~ 0.5 , 1–2, and 3–4 μm in 1050Al at tool rotation rate of 560, 980, 1840 rpm, respectively, at a constant traverse speed of 155 mm/min. Similarly, Sato et al. [67] reported the grain size of 5.9, 9.2, and 17.8 μm in FSW 6063Al at tool rotation rate of 800, 1220, 2450 rpm, respectively, at a constant traverse speed of

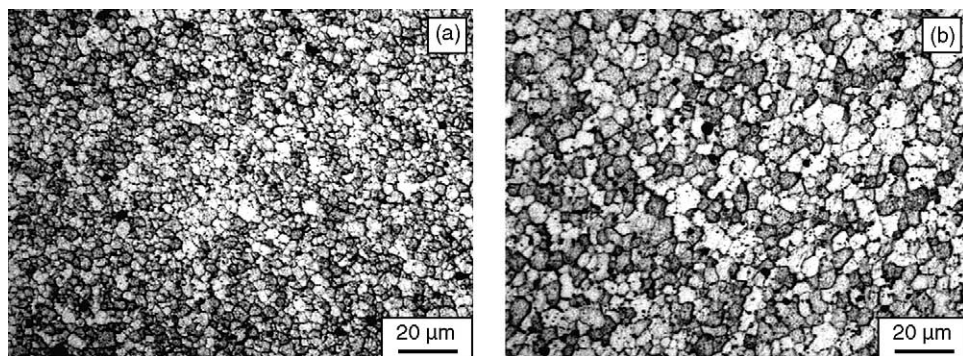


Fig. 20. Effect of FSP parameters on nugget grain size in FSP 7075Al-T7651 at processing parameter of: (a) 350 rpm, 152 mm/min and (b) 400 rpm, 102 mm/min [15].

360 mm/min. Fig. 20 shows the optical micrographs of FSP 7075Al-T651 processed by using two different processing parameter combinations. Decreasing the ratio of tool rotation rate/traverse speed from 400 rpm/102 mm/min to 350 rpm/152 mm/min resulted in a decrease in the recrystallized grain size from 7.5 to 3.8 μm . FSW/FSP at higher tool rotation rate or higher ratio of tool rotation rate/traverse speed results in an increase in both degree of deformation and peak temperature of thermal cycle. The increase in the degree of deformation during FSW/FSP results in a reduction in the recrystallized grain size according to the general principles for recrystallization [97]. On the other hand, the increase in peak temperature of FSW/FSP thermal cycle leads to generation of coarse recrystallized grains, and also results in remarkable grain growth. A recent investigation on FSP 7050Al has revealed that the initial size of newly recrystallized grains is on the order of 25–100 nm [98]. When heated for 1–4 min at 350–450 $^{\circ}\text{C}$, these grains grow to 2–5 μm , a size equivalent to that found in FSP aluminum alloys [98]. Therefore, the variation of recrystallized grain size with tool rotation rate or traverse speed in FSW/FSP aluminum alloys depends on which factor is dominant. The investigations on FSP 1050Al and 7075Al-T651 appear to indicate that the peak temperature of FSW/FSP thermal cycle is the dominant factor in determining the recrystallized grain size. Thus, the recrystallized grain size in the FSW/FSP aluminum alloys generally increases with increasing the tool rotation rate or the ratio of tool rotation rate/traverse speed. Fig. 21 shows the variation of grain size with pseudo-heat index in 2024Al and 7075Al [99]. It shows that there is an optimum combination of tool rotation rate and traverse speed for generating the finest grain size in a specific aluminum alloy with same tool geometry and temperature of the workpiece.

The grain size within the weld zone tends to increase near the top of the weld zone and it decreases with distance on either side of the weld-zone centerline, and this corresponds roughly to temperature variation within the weld zone [8,10,41]. For example, Mahoney et al. [100] reported a variation in grain size from the bottom to the top as well as from the advancing to the retreating side in a 6.35 mm-thick FSP 7050Al. Fig. 22 shows the distribution of the grain sizes in different locations of the nugget zone of FSP 7050Al [100]. The average grain size ranges from 3.2 μm at the bottom to 5.3 μm at the top and 3.5 μm from the retreating side to 5.1 μm on the advancing side. Similarly, in a 25.4 mm thick plate of FSW 2519Al, it was found that the average grain sizes were 12, 8 and 2 μm , respectively, in

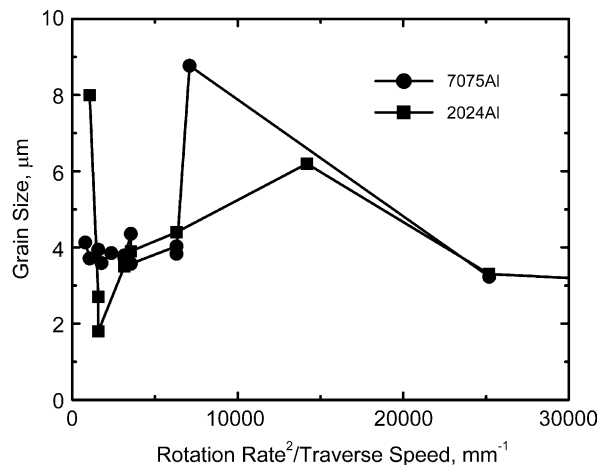


Fig. 21. Variation of grain size with pseudo-heat index [99]. Note that the grain size does not monotonically increase with increasing heat index.

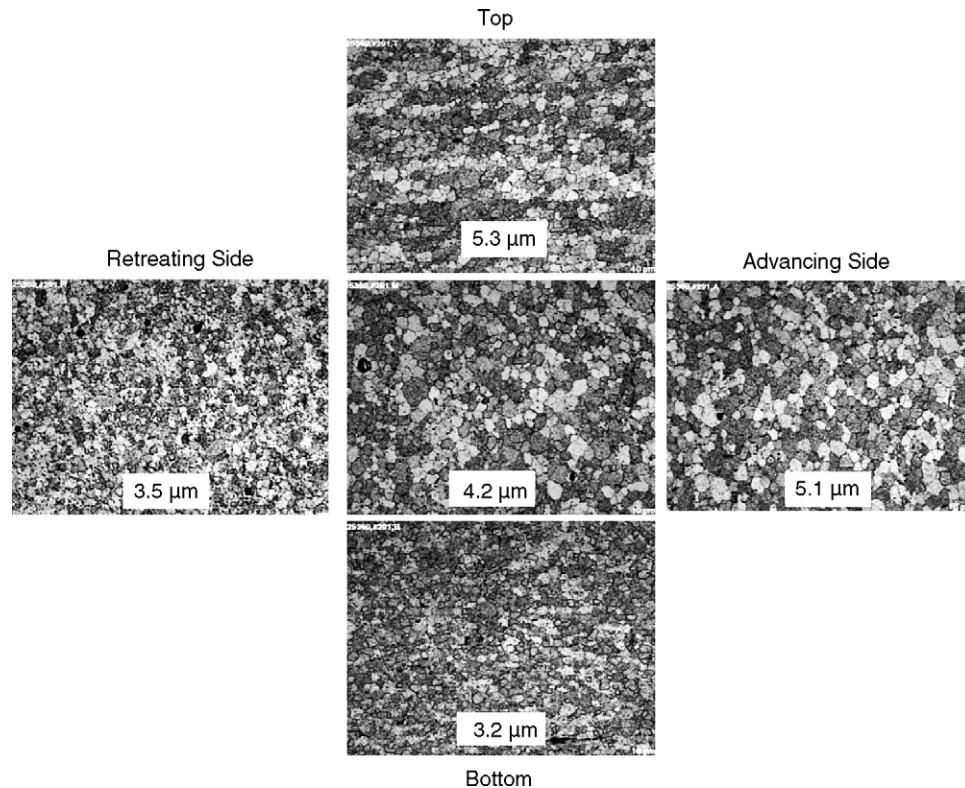


Fig. 22. Grain size distribution in various locations of 7050Al weld nugget [100].

the top, middle, and bottom region of the weld nugget [89]. Such variation in grain size from bottom to top of the weld nugget is believed to be associated with difference in temperature profile and heat dissipation in the nugget zone. Because the bottom of workpieces is in contact with the backing plate, the peak temperature is lower and the thermal cycle is shorter compared to the nugget top. The combination of lower temperature and shorter excursion time at the nugget bottom effectively retards the grain growth and results in smaller recrystallized grains. It is evident that with increasing plate thickness, the temperature difference between bottom and top of the weld nugget increases, resulting in increased difference in grain size.

4.1.3. Recrystallization mechanisms

Several mechanisms have been proposed for dynamic recrystallization process in aluminum alloys, such as discontinuous dynamic recrystallization (DDRX), continuous dynamic recrystallization (CDRX), and geometric dynamic recrystallization (GDRX) [97,101–106]. Aluminum and its alloys normally do not undergo DDRX because of their high rate of recovery due to aluminum's high stacking-fault energy [101,105]. However, particle-simulated nucleation of DDRX is observed in alloys with large ($>0.6 \mu\text{m}$) secondary phases [101–106]. The DDRX is characterized by nucleation of new grains at old high-angle boundaries and gross grain boundary migration [97]. On the other hand, CDRX has been widely studied in commercial superplastic aluminum alloys [107–111] and two-phase stainless steels [112–114]. Several mechanisms of CDRX have been proposed whereby subgrains rotate and achieve a high misorientation angle with little boundary migration. For example,

mechanisms include subgrain growth [107], lattice rotation associated with sliding [108,111], and lattice rotation associated with slip [114].

As for dynamic nucleation process in the nugget zone of FSW aluminum alloys, CDRX [6,75,84], DDRX [67,95,98], GDRX [69,115], and DRX in the adiabatic shear bands [116] have been proposed to be possible mechanisms. Jata and Semiatin [6] were the first to propose CDRX as operative dynamic nucleation mechanism during FSW. They suggested that low-angle boundaries in the parent metal are replaced by high-angle boundaries in the nugget zone by means of a continuous rotation of the original low-angle boundaries during FSW. In their model, dislocation glide gives rise to a gradual relative rotation of adjacent subgrains. Similarly, Heinz and Skrotzki [75] also proposed that CDRX is operative during FSW/FSP. In this case, strain induces progressive rotation of subgrains with little boundary migration. The subgrains rotation process gradually transforms the boundaries to high-angle grain boundaries.

However, it is important to point out that many of the recrystallized grains in the nugget zone are finer than the original subgrain size. Thus, it is unlikely that the recrystallized grains in the nugget zone result from the rotation of original elongated subgrains in the base metal. Recently, Su et al. [84] conducted a detailed microstructural investigation of FSW 7050Al-T651. Based on microstructural observations, they suggested that the dynamic recrystallization in the nugget zone can be considered a CDRX on the basis of dynamic recovery. Subgrain growth associated with absorption of dislocation into the boundaries is the CDRX mechanism. Repeated absorption of dislocations into subgrain boundaries is the dominant mechanism for increasing the misorientation between adjacent subgrains during the CDRX.

Alternatively, DDRX has been recently proposed as an operative mechanism for dynamic nucleation process in FSW/FSP aluminum alloys based on recent experimental observations [95,98]. Su et al. [95] reported generation of recrystallized grains of $\sim 0.1 \mu\text{m}$ in a FSP 7075Al by means of rapid cooling behind the tool. Similarly, Rhodes et al. [98] obtained recrystallized grains of 25–100 nm in FSP 7050Al-T76 by using “plunge and extract” technique and rapid cooling. These recrystallized grains were significantly smaller than the pre-existing subgrains in the parent alloy, and identified as non-equilibrium in nature, predominantly high-angled, relatively dislocation-free [95,98]. Su et al. [95] and Rhodes et al. [98] proposed that DDRX mechanism is responsible for the nanostructure evolution.

The fact that recrystallized grains in the nugget zone of FSW/FSP aluminum alloys are significantly smaller than the pre-existing subgrains in the parent alloy strongly suggests that DDRX is the operative mechanism for recrystallization during FSW/FSP of aluminum alloys.

4.1.4. Precipitate dissolution and coarsening

As presented in Section 3.2, FSW/FSP results in the temperature increase up to 400–550 °C within the nugget zone due to friction between tool and workpieces and plastic deformation around rotating pin [4,5,41,60–63,67,68]. At such a high temperature precipitates in aluminum alloys can coarsen or dissolve into aluminum matrix depending on alloy type and maximum temperature.

Liu et al. [5] investigated the microstructure of a friction stir welded 6061Al-T6. They reported that the homogeneously distributed precipitates are generally smaller in the workpiece than in the nugget zone. However, there were far fewer large precipitates in the nugget zone than in the base material. This implies the occurrence of both dissolution and coarsening of precipitates during FSW. Recently, Sato et al. [61] examined the microstructural evolution of a 6063Al-T5 during FSW using TEM. They did not observe precipitates within the nugget zone, indicating that all the precipitates were dissolved into aluminum matrix during FSW. More recently, Heinz and Skrotzki [75] also reported complete dissolution of the precipitates in FSW 6013Al-T6 and 6013Al-T4 with a tool

rotation rate of 1400 rpm and a traverse speed of 400–450 mm/min. Similarly, in FSW 7XXX aluminum alloys (7075Al-T7451), Jata et al. [92] also observed the absence of strengthening precipitates in the nugget zone, indicating complete dissolution of the precipitates. The overall response includes a combination of dissolution, coarsening and reprecipitation of strengthening precipitates during FSW/FSP.

4.1.5. Texture

Texture influences a variety of properties, including strength, ductility, formability and corrosion resistance. As mentioned earlier, the FSW material consists of distinct microstructural zones, i.e., nugget, TMAZ, HAZ and base material. Each zone has different thermo-mechanical history. What is even more complicated for FSW is that the nugget region consists of sub-domains. For example, the top layer undergoes deformation by shoulder after the pin has passed through. In addition, depending on the tool rotation rate and traverse speed, the nugget region can contain ring pattern or other microstructural variations. A few texture studies of FSW aluminum alloys have been reported [117–120]. In the last decade, the use of microtexture using orientation imaging microscopy (OIM) has proved to be a very valuable tool in not only obtaining the texture information, but also establish the grain boundary misorientation distribution data from same set of experiments.

Sato et al. [118] and Field et al. [119] have reported detailed texture analysis through the FSW welds. The overall plots of grain boundary misorientation distribution showed that the nugget region predominantly consisted of high-angle grain boundaries. However, the microtexture results showed complex texture pattern. Sato et al. [118] noted that the Goss orientation in the parent 6063Al changed to shear texture component with two types of orientation in the center of the nugget. The pole figures were examined for the surface and center regions on both sides of the center line, i.e., on the advancing and retreating sides. An important observation that emerged, by comparing pole figures at 2.5, 3.3, and 4 mm away on both sides from the center, was that the weld center roughly contained $\{1\ 1\ 0\}\langle 0\ 0\ 1\rangle$ and $\{1\ 1\ 4\}\langle 2\ 2\ 1\rangle$ shear texture components. However, these components were rotated around the ‘normal direction’, the direction of the axis of pin. Both these components were also observed by Field et al. [119], including the rotational aspect of the texture component from the advancing side to the retreating side. During FSW, the material undergoes intense shearing and dynamic recrystallization concurrently. One of the key issues to understand is how nucleation of new grains and continuous deformation influence the final texture results. In addition, it is important to separate out the effect of final deformation by shoulder through the forging action after the pin has passed. The deformation under shoulder is likely to influence the final texture significantly. It adds a shear deformation component at lower temperature to the recrystallized volume processed by the pin.

4.2. Thermo-mechanically affected zone

Unique to the FSW/FSP process is the creation of a transition zone—thermo-mechanically affected zone (TMAZ) between the parent material and the nugget zone [4,15,41], as shown in Fig. 17. The TMAZ experiences both temperature and deformation during FSW/FSP. A typical micrograph of TMAZ is shown in Fig. 23. The TMAZ is characterized by a highly deformed structure. The parent metal elongated grains were deformed in an upward flowing pattern around the nugget zone. Although the TMAZ underwent plastic deformation, recrystallization did not occur in this zone due to insufficient deformation strain. However, dissolution of some precipitates was observed in the TMAZ, as shown in Fig. 24c and d, due to high-temperature exposure during FSW/FSP [61,84]. The extent of dissolution, of course, depends on the thermal cycle experienced by TMAZ. Furthermore, it was revealed that the grains in the TMAZ usually contain a high density of sub-boundaries [61].

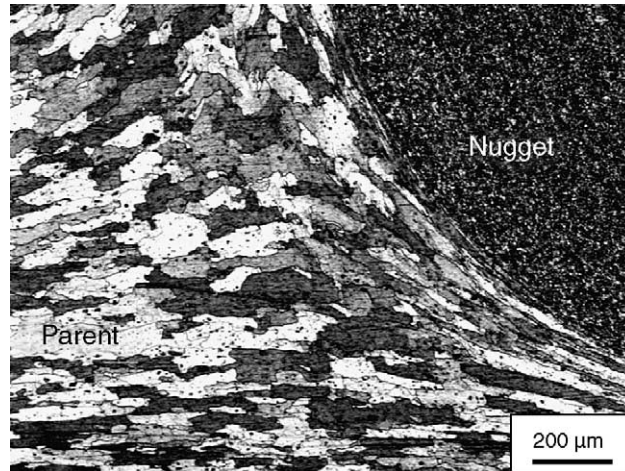


Fig. 23. Microstructure of thermo-mechanically affected zone in FSP 7075Al [15].

4.3. Heat-affected zone

Beyond the TMAZ there is a heat-affected zone (HAZ). This zone experiences a thermal cycle, but does not undergo any plastic deformation (Fig. 17). Mahoney et al. [61] defined the HAZ as a zone experiencing a temperature rise above 250 °C for a heat-treatable aluminum alloy. The HAZ retains

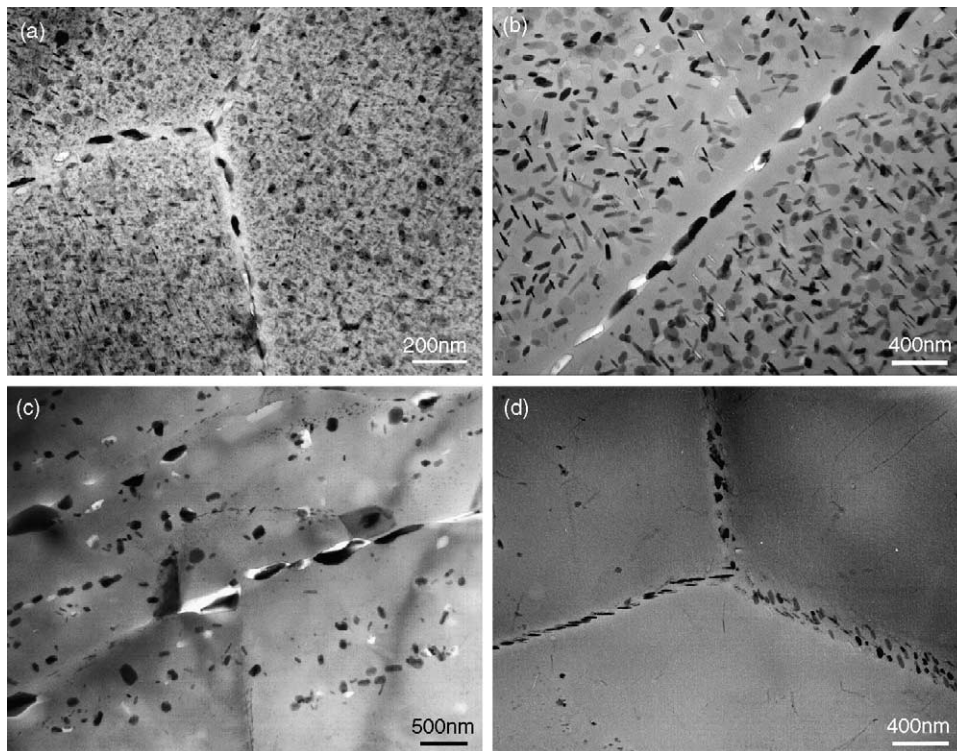


Fig. 24. Precipitate microstructures in the grain interior and along grain boundaries in: (a) base metal, (b) HAZ, (c) TMAZ near HAZ, and (d) TMAZ near nugget zone (FSW 7050Al-T651, tool rotation rate: 350 rpm, traverse speed: 15 mm/min) (after Su et al. [84]).

the same grain structure as the parent material. However, the thermal exposure above 250 °C exerts a significant effect on the precipitate structure.

Recently, Jata et al. [92] investigated the effect of friction stir welding on microstructure of 7050Al-T7451 aluminum alloy. They reported that while FSW process has relatively little effect on the size of the subgrains in the HAZ, it results in coarsening of the strengthening precipitates and the precipitate-free zone (PFZ) increases by a factor of 5. Similar observation was also made by Su et al. [84] in a detailed TEM examination on FSW 7050Al-T651 (Fig. 24b). The coarsening of precipitates and widening of PFZs is evident. Similarly, Heinz and Skrotzki [75] also observed significant coarsening of the precipitates in the HAZ of FSW 6013Al.

5. Properties

5.1. Residual stress

During fusion welding, complex thermal and mechanical stresses develop in the weld and surrounding region due to the localized application of heat and accompanying constraint. Following fusion welding, residual stresses commonly approach the yield strength of the base material. It is generally believed that residual stresses are low in friction stir welds due to low temperature solid-state process of FSW. However, compared to more compliant clamps used for fixing the parts in conventional welding processes, the rigid clamping used in FSW exerts a much higher restraint on the welded plates. These restraints impede the contraction of the weld nugget and heat-affected zone during cooling in both longitudinal and transverse directions, thereby resulting in generation of longitudinal and transverse stresses. The existence of high value of residual stress exerts a significant effect on the postweld mechanical properties, particularly the fatigue properties. Therefore, it is of practical importance to investigate the residual stress distribution in the FSW welds.

James and Mahoney [93] measured residual stress in the FSW 7050Al-T7451, C458 Al–Li alloy, and 2219Al by means of X-ray diffraction $\sin^2 \psi$ method. Typical results obtained in FSW 7050Al-T7451 by pinhole X-ray beam (1 mm) are tabulated in Table 4. This investigation revealed following findings. First, the residual stresses in all the FSW welds were quite low compared to those generated during fusion welding. Second, at the transition between the fully recrystallized and partially recrystallized regions, the residual stress was higher than that observed in other regions of the weld. Third, generally, longitudinal (parallel to welding direction) residual stresses were tensile and transverse (normal to welding direction) residual stresses were compressive. The low residual stress

Table 4

Residual stress measurement (MPa) in FSW 7050Al-T6541 weld by pinhole beam X-ray (after James and Mahoney [93])

Location	Distance from weld centreline (mm)	Longitudinal		Transverse	
		Retreating side	Advancing side	Retreating side	Advancing side
Top surface	2	22	19	–33	–41
	4	39	35	–14	–27
	6	55	72	–21	–24
	7	64	48	–40	–47
	8	101	76	–99	–43
Root surface	1	13	42	28 ± 52	–12
	3	36 ± 52	48 ± 54	–71	–19
	5	61 ± 30	55	–55 ± 103	–48

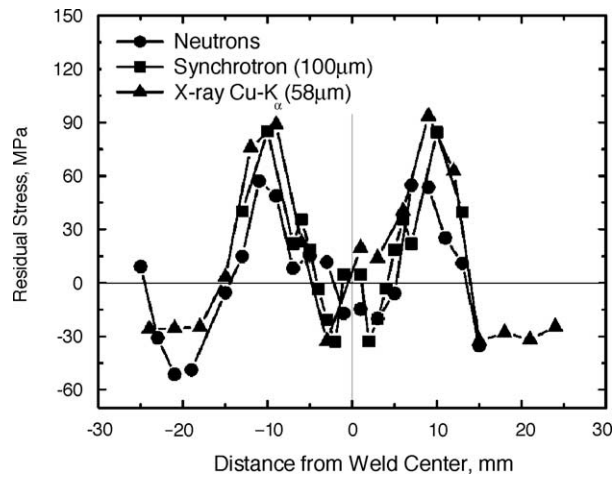


Fig. 25. Longitudinal residual stress distribution in FSW 6013Al-T4 welds determined by different measurement methods (tool rotation rate: 2500 rpm, traverse speed: 1000 mm/min, tool shoulder diameter: 15 mm) (after Donne et al. [121]).

in the FSW welds was attributed to the lower heat input during FSW and recrystallization accommodation of stresses [93].

Recently, Donne et al. [121] measured residual stress distribution on FSW 2024Al-T3 and 6013Al-T6 welds by using the cut compliance technique, X-ray diffraction, neutron diffraction and high-energy synchrotron radiation. Six important observations can be made from their study. First, the experimental results obtained by these measurement techniques were in good qualitative and quantitative agreement. Second, the longitudinal residual stresses were always higher than the transverse ones, independent on pin diameter, tool rotation rate and traverse speed. Third, both longitudinal and transverse residual stresses exhibited an “M”-like distribution across the weld. A typical longitudinal residual stress distribution is shown in Fig. 25. Fig. 25 reveals that maximum tensile residual stresses were located ~ 10 mm away from the weld centerline, i.e., the HAZ. Small compressive residual stresses were detected in the parent metal adjacent to the HAZ and the weld seam. Fourth, residual stress distribution across the welds was similar at the top and root sides of the welds. Fifth, large-diameter tool widened the M-shaped residual stress distribution. With decreasing welding speed and tool rotation rate, the magnitude of the tensile residual stresses decreased. Sixth, in the case of the small samples of $30 \text{ mm} \times 80 \text{ mm}$ and $60 \text{ mm} \times 80 \text{ mm}$, the maximum longitudinal tensile residual stresses were in the range of 30–60% of weld material yield strength and 20–50% of base material yield strength. Clearly, the residual stress values in the FSW welds are remarkably lower than those in the fusion welds. However, Wang et al. [122] reported that larger values of residual stress may be present in larger samples of $200 \text{ mm} \times 200 \text{ mm}$.

More recently, Peel et al. [123] investigated the residual stress distribution on FSW 5083Al using synchrotron X-ray diffraction. Following observations can be made from their investigation. First, while longitudinal residual stress exhibited a “M”-like distribution across the weld similar to the results of Donne et al. [121], transverse residual stresses exhibited a peak at the weld center. Second, the nugget zone was in tension in both longitudinal and transverse directions. Third, peak tensile residual stress was observed at ~ 10 mm from the weld centerline, a distance corresponding to the edge of the tool shoulder. Fourth, longitudinal residual stress increased with increasing tool traverse speed, whereas transverse residual stresses did not exhibit evident dependence on the traverse speed. Fifth, a mild asymmetry in longitudinal residual stress profile was observed within the nugget zone with the stresses being $\sim 10\%$ higher on the advancing side. Sixth, similar to the results of Donne et al. [121],

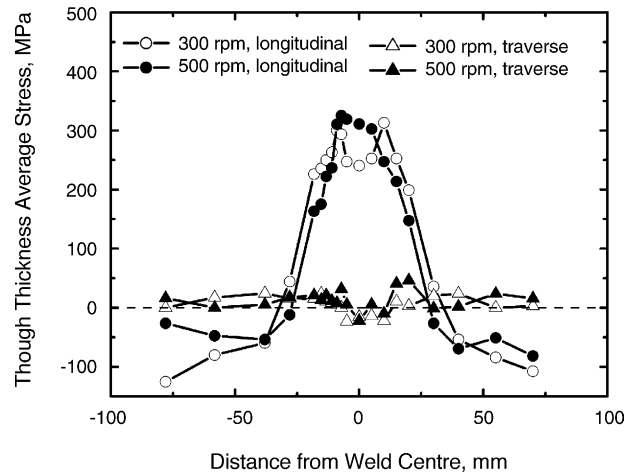


Fig. 26. Average, through thickness, longitudinal and transverse residual stress distribution as a function of distance from the weld centerline in FSW 204L stainless steel (tool traverse speed: 102 mm/min) (after Reynolds et al. [124]).

maximum residual stresses in longitudinal direction (40–60 MPa) were higher than those in transverse direction (20–40 MPa).

Clearly, maximum residual stresses observed in various friction stir welds of aluminum alloys were below 100 MPa [121–123]. The residual stress magnitudes are significantly lower than those observed in fusion welding, and also significantly lower than yield stress of these aluminum alloys. This results in a significant reduction in the distortion of FSW components and an improvement in mechanical properties.

On the other hand, Reynolds et al. [124] measured residual stress of 304L stainless steel FSW welds by neutron diffraction. Average, through thickness, longitudinal and transverse residual stresses are presented in Fig. 26 as a function of distance from the weld centerline. Fig. 26 revealed the following observations. First, the residual stress patterns observed for FSW are typical of most welding processes such as fusion welding, namely, high value of longitudinal tensile residual stress and very low transverse residual stress. Second, the maximum values of longitudinal residual stress were close to the base metal yield stress, and therefore similar in magnitude to those produced by fusion welding processes in austenitic stainless steels [125]. Third, increasing tool rotation rate from 300 to 500 rpm at a constant tool traverse speed of 102 mm/min did not exert marked effect on the residual stress distribution apart from slightly widening the range of high values of residual stress. Further, Reynolds et al. [124] reported that the longitudinal residual stress varied only slightly with depth, whereas the transverse stress varied significantly through the thickness. The sign of the transverse residual stress near the weld centerline was in general positive at the crown and negative at the root. This was attributed to rapid cooling experienced by the weld root due to the intimate contact between the weld root side and the backing plate. Clearly, the distribution and magnitude of residual stress in friction stir welds are different for aluminum alloy and steel. This is likely to be related to the temperature dependence of the yield strength and the influence of final deformation by the trailing edge of the tool shoulder.

5.2. Hardness

Aluminum alloys are classified into heat-treatable (precipitation-hardenable) alloys and non-heat-treatable (solid-solution-hardened) alloys. A number of investigations demonstrated that the change in hardness in the friction stir welds is different for precipitation-hardened and solid-solution-

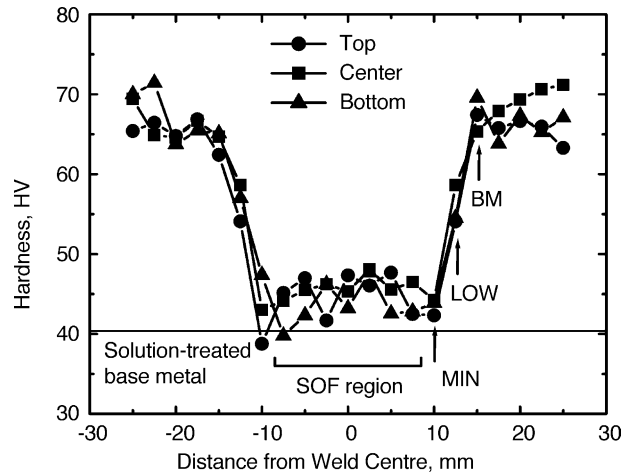


Fig. 27. Typical hardness curve across the weld of FSW 6063Al-T5 (after Sato et al. [61]).

hardened aluminum alloys. FSW creates a softened region around the weld center in a number of precipitation-hardened aluminum alloys [5,7,10,61,126,127]. It was suggested that such a softening is caused by coarsening and dissolution of strengthening precipitates during the thermal cycle of the FSW [5,7,10,61,126,127]. Sato et al. [61] have examined the hardness profiles associated with the microstructure in an FSW 6063Al-T5. They reported that hardness profile was strongly affected by precipitate distribution rather than grain size in the weld. A typical hardness curve across the weld of FSW 6063Al-T5 is shown in Fig. 27. The average hardness of the solution-treated base material is also included in Fig. 27 for comparison. Clearly, significant softening was produced throughout the weld zone, compared to the base material in T5 condition. Further, Fig. 27 shows that the lowest hardness does not lie in the center part of the weld zone, but is 10 mm away from the weld centerline. Sato et al. [61] labeled the hardness curves by BM (the same hardness region as the base material), LOW (the

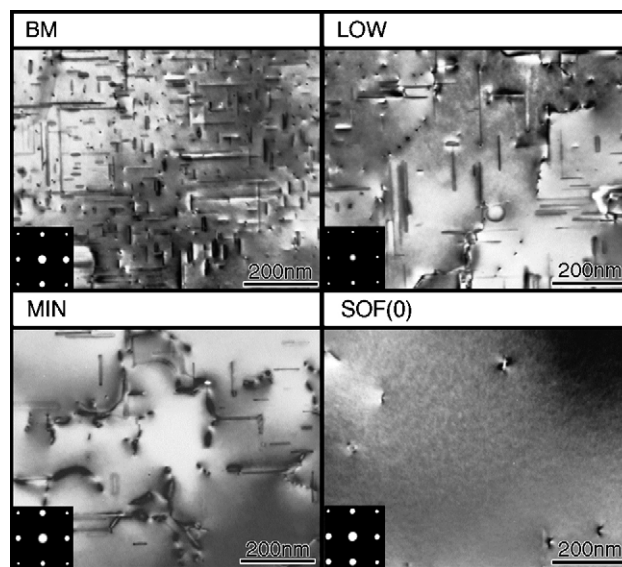


Fig. 28. TEM micrographs showing precipitate distribution in various microstructural zones in FSW 6063Al-T5 (after Sato et al. [61]).

region of lower hardness than base material), MIN (the minimum-hardness region), and SOF (the softened region) (Fig. 27), and examined the microstructure of these four regions. As shown in Fig. 28, two kinds of precipitates are observed in the BM, LOW, and MIN regions; needle-shaped precipitates of about 40 nm in length, which are partially or completely coherent with the matrix, and rod-shaped precipitates approximately 200 nm in length, which have low coherency with the matrix. The mechanical properties of 6063Al depend mainly on the density of needle-shaped precipitates and only slightly on the density of rod-shaped precipitates [128,129]. Sato et al. [61] reported that the microstructure (type, size and distribution of precipitates) in the BM region was basically the same as that in the base material (Fig. 28a), which explains the same hardness in the BM region and the base material. In the LOW region, the density of needle-shaped precipitates was substantially reduced, whereas the density of rod-shaped precipitates was increased (Fig. 28b). This resulted in a reduction in hardness of the LOW region. For the MIN region, only low density of rod-shaped precipitates remained (Fig. 28c). Thus, not only the hardening effect of needle-shaped disappeared completely, but also solid-solution-hardening effect of solutes was reduced due to the existence of rod-shaped precipitates, which leads to the minimum hardness in the MIN region. In the SOF region, no precipitates were detected due to complete dissolution of the precipitates (Fig. 28d). Sato et al. [61] suggested that the somewhat higher hardness in the SOF region than in the base material was explained by the smaller grain size and higher density of sub-boundaries.

For the solid-solution-hardened aluminum alloys, generally, FSW does not result in softening in the welds [9,78,130]. For 5083Al-O containing small particles, the hardness profile was roughly uniform in the weld [78,130], whereas for 1080Al-O without any second-phase particles, the hardness in the nugget zone was slightly higher than that in the base material, and the maximum hardness was located in the TMAZ [78]. Microstructural factors governing the hardness in the FSW welds of the solid-solution-hardened aluminum alloys were suggested by various investigators [9,78,130]. In an investigation on the microstructure and properties of FSW 5083Al-O, Svesson et al. [130] reported that the nugget zone had fine equiaxed grains with a lower density of large particles (1–10 μm) and a higher density of small particles (0.1–1 μm). They suggested that the hardness profile mainly depended on dislocation density, because the dominant hardening mechanism for 5083Al is strain hardening. On the other hand, Sato et al. [78] reported that FSW created the fine recrystallized grains in the nugget zone and recovered grains in the TMAZ in 5083Al-O with the nugget zone and the TMAZ having slightly higher dislocation densities than the base material. Both small and large $\text{Al}_6(\text{Mn,Fe})$ particles were detected in the nugget zone and the base material. They concluded that the hardness profile could not be explained by the Hall–Petch relationship, but rather by Orowan strengthening, namely, the hardness profile in the FSW 5083Al was dominantly governed by the dispersion strengthening due to distribution of small particles. In this case, the interparticle spacing is likely to be much lower than the grain size. For the FSW 1080Al-O, Sato et al. [78] reported that the nugget zone consisted of recrystallized grains with a low density of dislocations, while the TMAZ had recovered grains with a subgrain structure. The overall behavior is governed by the relative strengthening contributions from grain boundaries, particles and substructure.

5.3. Mechanical properties

FSW/FSP results in significant microstructural evolution within and around the stirred zone, i.e., nugget zone, TMAZ, and HAZ. This leads to substantial change in postweld mechanical properties. In the following sections, typical mechanical properties, such as strength, ductility, fatigue, and fracture toughness are briefly reviewed.

Table 5

Longitudinal tensile properties of weld nugget in friction stir welded 7075Al-T651 at room temperature (after Mahoney et al. [41])

Condition	UTS (MPa)	YS (MPa)	Elongation (%)
Base metal, T651	622	571	14.5
As-FSW	525	365	15
Postweld age treatment	496	455	3.5

5.3.1. Strength and ductility

Mahoney et al. [41] investigated the effect of FSW on room-temperature tensile properties of 7075Al-T651. Tensile specimens were machined from the nugget zone in two directions, parallel (longitudinal) and normal (transverse) to the weld. Longitudinal tensile specimens contained only fully recrystallized grains from the nugget zone, whereas transverse tensile specimens contained microstructures from all four zones, i.e., parent material, HAZ, TMAZ, and nugget zone. Table 5 summarizes the longitudinal tensile properties of nugget zone. As-welded samples show a reduction in yield and ultimate strengths in the weld nugget, while elongation was unaffected. Mahoney et al. [41] attributed the reduced strength to the reduction in pre-existing dislocations and the elimination of the very fine hardening precipitates [4]. In order to recover the lost tensile strength of the nugget zone, Mahoney et al. [41] conducted a postweld aging treatment (121 °C/24 h) on the FSW sample. As shown in Table 5, the aging treatment resulted in recovery of a large portion of the yield strength in the nugget, but at the expense of ultimate strength and in particularly ductility. The increase in the yield strength of postweld samples was attributed to the increase in the volume fraction of fine hardening precipitates, whereas the reduction in the ductility was accounted for by both the increase in the hardening precipitates and the development of precipitate-free zones (PFZs) at grain boundaries [41]. The tensile properties in transverse orientation of FSW 7075Al-T651 are summarized in Table 6. Compared to unwelded parent metal, samples tested in transverse direction show a significant reduction in both strength and ductility. Furthermore, the strength and ductility observed in transverse orientation are also substantially less than those in longitudinal orientation. The postweld aging treatment did not restore any of the strength to the as-welded condition and further reduced ductility. In both as-welded and aged condition, failures occurred as shear fracture in the HAZ. As reported before, the tensile specimens in the transverse orientation cover four different microstructures, i.e., parent material, HAZ, TMAZ, and nugget zone. The observed ductility is an average strain over the gage length including various zones. The different zones have different resistances to deformation due to differences in grain size and precipitate size and distribution as discussed in Section 4. The HAZ has the lowest strength due to significantly coarsened precipitates and the development of the FPZs. Thus, during tension, strain occurs mainly in the HAZ. As shown in Fig. 29, the low-strength HAZ locally elongated to high levels of strain (12–14%), eventually resulting in necking and fracture, whereas the nugget zone experiences only 2–5% strain. Therefore, fracture always occurred in the HAZ, resulting in a low strength and ductility along transverse orientation of the weld.

Table 6

Room-temperature tensile properties in transverse orientation of friction stir welded 7075Al-T651 (after Mahoney et al. [41])

Condition	UTS (MPa)	YS (MPa)	Elongation (%)
Base metal, T651	622	571	14.5
As-FSW	468	312	7.5
Postweld age treatment	447	312	3.5

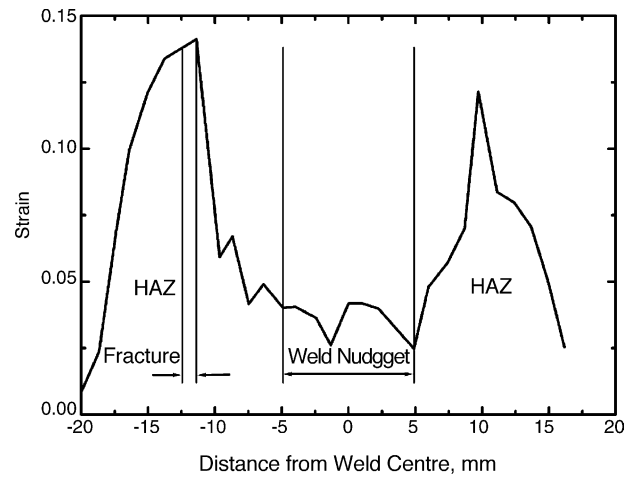


Fig. 29. Tensile strain distribution within the HAZs and weld nugget of FSW 7075Al-T651 weld (after Mahoney et al. [41]).

Recently, Sato et al. [78] investigated the transverse tensile properties of the friction stir weld of 6063-T5 aluminum. In order to reveal the effect of postweld treatment on the weld properties, postweld aging (175 °C/12 h) and postweld solution heat treatment and aging (SHTA, 530 °C/1 h + 175 °C/12 h) were conducted on the welds. Fig. 30 shows the tensile properties of the base material, the weld, aged weld, and the SHTA weld. Fig. 30 reveals that the strengths and elongation are lowest in the as-welded weld. The aged weld has slightly higher strengths than the base material with

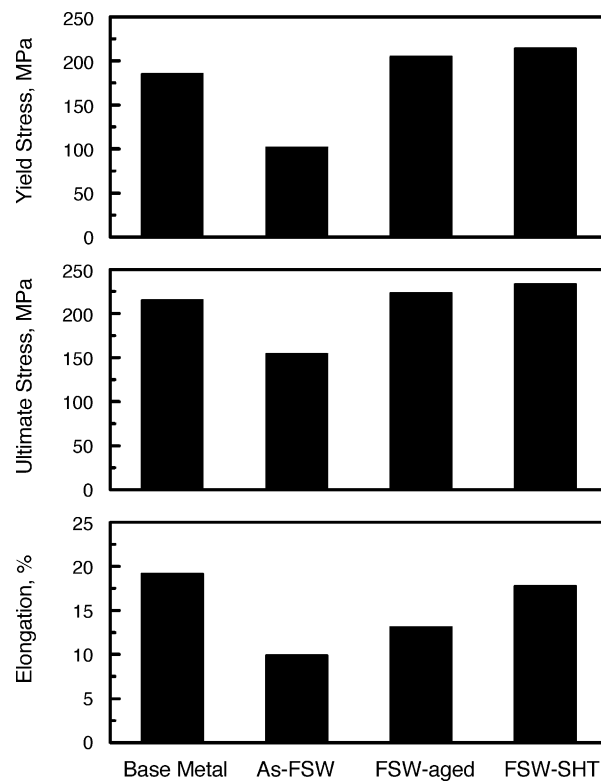


Fig. 30. Tensile properties of base metal, as-welded weld, aged weld, and SHTA weld for 6063Al-T5 (after Sato et al. [78]).

Table 7

Room-temperature tensile properties of base material and welded joints in both longitudinal (L) and transverse (T) orientations of FSW 2024Al-T3 plates of 4 and 1.6 mm thickness (after Biallas et al. [40])

Material	Rotation rate (rpm)	Traverse speed (mm/min)	YS (MPa)	UTS (MPa)	Elongation (%)	UTS _{FSW} /UTS _{base}
Base-4 mm-L			424	497	14.9	
FSW-4 mm-L	800	80	279	408	6.6	0.82
FSW-4 mm-L	1000	100	296	423	8.1	0.85
FSW-4 mm-L	1250	125	304	432	7.6	0.87
Base-1.6 mm-L			325	472	21.0	
FSW-1.6 mm-L	1200	120	301	424	6.3	0.90
FSW-1.6 mm-L	1800	180	315	434	6.9	0.92
FSW-1.6 mm-L	2400	240	325	461	11.0	0.98

concurrently improved ductility. The SHTA increases the strengths of the weld to above those of the base material with almost completely restored ductility. Sato et al. [78] reported that the strain of the as-welded weld was localized in a region 5–6 mm from the weld centerline, i.e. the minimum-hardness region (MIN) as discussed previously in Section 5.2, resulting in final fracture with low strength and ductility. Postweld aging leads to reprecipitation of the needle-shaped precipitates in the weld, resulting in a shift in the minimum hardness from the original MIN to low hardness (LOW) region. This is because the high density of large β' precipitates in the LOW region of as-welded weld consume large amount of the solutes, thereby reduced the density of the needle-shaped precipitates during the postweld aging. Thus, fracture occurred in a region 7–8 mm from the weld centerline, i.e., original LOW. On the other hand, the solution heat-treatment produces a supersaturated solid solution throughout the specimen, and the subsequent aging leads to the homogenous reprecipitation of the needle-shaped precipitates. This results in increased strength and homogeneous distribution of strain throughout the weld. In this case, the fracture occurred in the base material region. Further, fracture locations of all welds were at the retreating side.

Biallas et al. [40] studied the effect of FSW parameters on the tensile properties of FSW 2024Al-T4. The tensile properties are summarized in Table 7. It is evident from Table 7 that for a constant ratio of tool traverse speed/rotation rate, both yield and ultimate strengths increase with increasing tool rotation rate and ductility is also improved. Furthermore, Table 7 reveals that higher strength and joining efficiency were observed in thinner plates than in thicker plates.

Table 8 summarizes the transverse tensile strength of FSW welds and joining efficiency of FSW welds for various aluminum alloys. This table reveals that the joining efficiency of FSW welds ranges from 65 to 96% for heat-treatable aluminum alloys and is 95–119% for non-heat-treatable aluminum alloy 5083Al. The joining efficiency for FSW is significantly higher than that for conventional fusion welding, particularly for heat-treatable aluminum alloys.

It should be emphasized that the strengths obtained in the transverse tensile test of the FSW weld using large specimens represent the weakest region of the weld and the elongation is an average strain over the gage length including various zones. Although such a tensile test is meaningful for engineering applications, it does not provide an insight into the correlation between the intrinsic tensile properties and localized microstructure. Therefore, it is necessary to utilize a more suitable test technique to establish the intrinsic tensile properties of the weld associated with localized microstructure. Recently, two studies were conducted by von Strombeck et al. [135] and Mishra et al. [139] to determine the tensile properties at different locations of the FSW welds using mini tensile specimens. Similar experimental results were reported in these two studies. A typical variation of tensile properties with the position across the weld of FSW 7075Al alloy is shown in Fig. 31. Fig. 31

Table 8
Friction stir weld joint efficiency for various aluminum alloys

Alloy	Base metal UTS	Friction stir weld UTS	Joint efficiency (%)	References
AFC458-T8	544.7	362.0	66	[131]
2014-T651 (6 mm)	479–483	326–338	68–70	[131,134]
2024-T351 (5 mm)	483–493	410–434	83–90	[131,135]
2219-T87	475.8	310.3	65	[131]
2195-T8	593.0	406.8	69	[131]
5083-O (6–15 mm)	285–298	271–344	95–119	[12,131,132,134]
6061-T6 (5 mm)	319–324	217–252	67–79	[131,135]
7050-T7451 (6.4 mm)	545–558	427–441	77–81	[102,131,138]
7075-T7351	472.3	455.1	96	[131]
7075-T651 (6.4 mm)	622	468	75	[41]
6056-T78 (6 mm)	332	247	74	[133]
5005-H14 (3 mm)	158	118	75	[135]
7020-T6 (5 mm)	385	325	84	[135]
6063-T5 (4 mm)	216	155	72	[78]
2024-T3 (4 mm)	478	425–441	89–90	[136,137]
7475-T76		465	92	[136]
6013-T6 (4 mm)	394–398	295–322	75–81	[75,137]
6013-T4 (4 mm)	320	323	94	[75]
2519-T87 (25.4 mm)	480	379	79	[89]

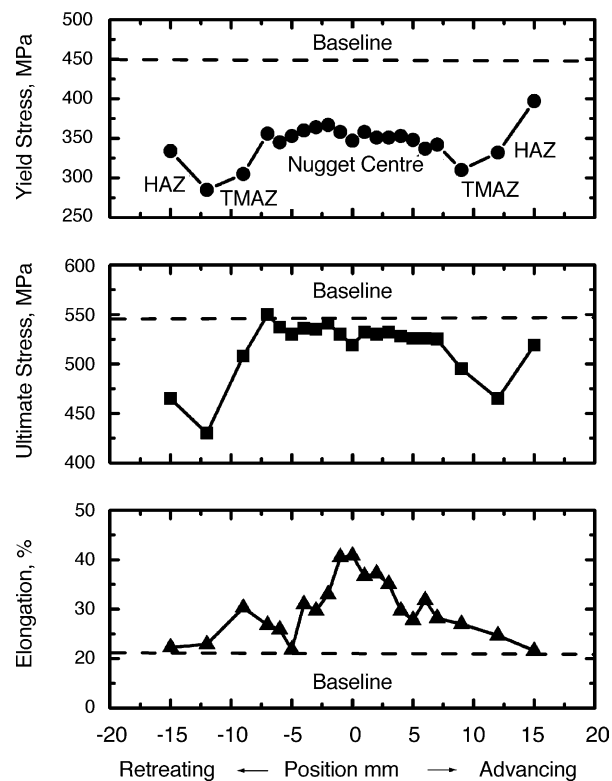


Fig. 31. Variation of tensile properties with the position across the weld in an FSW 7075Al alloy [139].

shows the following important findings. First, the strength is almost constant in the nugget zone. While the yield strength in the nugget zone is $\sim 80\%$ of the base material, the ultimate strength is close to 100% and the ductility is significantly improved. The combination of comparable ultimate strength and higher ductility was attributed to the fine-grained microstructure in the nugget zone [139]. Second, approaching the nugget/TMAZ transition region, the strength remains similar to the nugget zone, but the ductility starts decreasing toward the baseline. The decrease in ductility as compared to the nugget center can be correlated to the fact that the TMAZ retains the deformed structure. Third, both yield and ultimate strengths start to drop beyond ± 7 mm (TMAZ/HAZ) from the weld centerline. The lowest strength, $\sim 60\%$ of base material, was observed in the HAZ (12 mm away from the weld centerline on the retreating side). It is surprising that the drop in strength is not accompanied by an increase in ductility. These results provided additional insight to the large-specimen results of Mahoney et al. [41] and Sato et al. [78]. The locally concentrated strain of up to 14% occurred in the HAZ of large-specimen is due to low strength of the HAZ and did not mean that the HAZ has better ductility than other regions. Fourth, the intrinsic strength and ductility of retreating and advancing sides are different. The retreating side has lower strength. This is consistent with the previous observation that fracture always occurred on the retreating side [78].

5.3.2. Fatigue

For many applications, like aerospace structures, transport vehicles, platforms, and bridge constructions, fatigue properties are critical. Therefore, it is important to understand the fatigue characteristics of FSW welds due to potentially wide range of engineering applications of FSW technique. This has led to increasing research interest on evaluating the fatigue behavior of FSW welds, including stress–number of cycles to failure ($S-N$) behavior [40,89,140–145] and fatigue crack propagation (FCP) behavior [89,92,137,138,146,147].

5.3.2.1. $S-N$ behavior. In the past few years, several investigations were conducted on the $S-N$ behavior of FSW 6006Al-T5 [140,141], 2024Al-T351 [142], 2024Al-T3 [40], 2024Al-T3, 6013Al-T6, 7475Al-T76 [136], 2219Al-T8751 [145], and 2519Al-T87 [89]. These studies resulted in the following five important observations. First, the fatigue strength of the FSW weld at 10^7 cycles was lower than that of the base metal, i.e., the FSW welds are susceptible to fatigue crack initiation

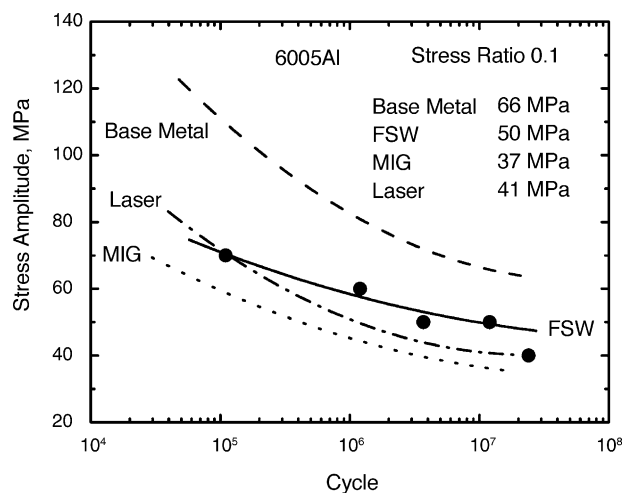


Fig. 32. $S-N$ curves of base metal, FSW weld, laser weld and MIG weld for 6005Al-T5 (after Hori et al. [140]).

[40,136,143–146]. Further, Bussu and Irving [147] showed that the transverse FSW specimens had lower fatigue strength than the longitudinal FSW specimens. However, the fatigue strength of the FSW weld was higher than that of MIG and laser welds [141,142]. Typical $S-N$ curves for FSW weld, laser weld, MIG weld, and base metal of 6005Al-T5 are shown in Fig. 32. The finer and uniform microstructure after FSW leads to better properties as compared to fusion (laser and MIG) welds. Second, surface quality of the FSW welds exerted a significant effect on the fatigue strength of the welds. Hori et al. [140] reported that the fatigue strength of the FSW weld decreased with increasing tool traverse speed/rotation rate (v/ω) ratio due to the increase of non-welded groove on the root side of the weld. However, when the non-welded groove was skimmed, the fatigue strength of the FSW weld remained unchanged by changing the v/ω ratio. Furthermore, Bussu and Irving [142] reported that skimming 0.5 mm thick layer from both root and top sides removed all the profile irregularities and resulted in fatigue strength, of both transverse and longitudinal FSW specimens, comparable to that of the base metal. Similarly, Magnusson and Källman [136] reported that the removal of 0.1–0.15 mm thick layer from top side by milling can result in a significant improvement in the fatigue strength of FSW welds. These observations suggest that the fatigue life is limited by surface crack nucleation and there are no inherent defects or internal flaws in successful FSW welds. Third, the effect of FSW parameters on the fatigue strength is complicated and no consistent trend is obtained so far. Hori et al. [140] reported that for a specific v/ω ratio, the fatigue strength of the FSW weld was not affected by the tool traverse speed. However, Biallas et al. [40] observed that for a constant v/ω ratio, the fatigue strength of FSW 2024Al-T3 welds with thickness of 1.6 and 4 mm was considerably enhanced with increasing tool rotation rate and traverse speed. The $S-N$ data of 1.6 mm thick FSW weld made at a high tool rotation rate of 2400 rpm and a traverse speed of 240 mm/min were even within the scatter band of the base metal. Fourth, low plasticity burnishing (LPB) after FSW can enhance the fatigue life of the FSW joints. Jayaraman et al. [145] reported that LPB processing increased the high cycle fatigue endurance of aluminum alloy FSW 2219Al-T8751 by 80% due to introduction of a deep surface layer of compressive residual stress. Also, the surface becomes highly polished after LPB and as noted earlier the fatigue life of FSW welds is limited by surface crack nucleation. Compressive residual stresses at surface and high-quality surface finish are desirable for good fatigue properties. Fifth, while the fatigue resistance of FSW specimens in air is inferior to that of the base metal, Pao et al. [89] reported that FSW 2519Al-T87 and base metal specimens have similar fatigue lives and fatigue thresholds in 3.5% NaCl solution. Again, the corrosion products at the surface are likely to influence the fatigue crack nucleation and the influence of FSW on corrosion adds to the complexity of corrosion–fatigue interaction. Overall, the fatigue results for FSW aluminum alloys are very encouraging.

5.3.2.2. *Fatigue crack propagation behavior.* In recent years, several investigations were undertaken to evaluate the effect of FSW on the fatigue crack propagation behavior [89,92,137,138,146,147]. The investigated materials and specimens geometries used are summarized in Table 9. Donne et al. [137]

Table 9

A summary of materials and methods used for evaluating fatigue crack growth of FSW welds

Materials	Testing method	Reference
2024Al-T3	Compact tension	[137]
6013Al-T6	Compact tension; middle cracked tension	[137]
7050Al-T7451	Eccentrically loaded single edge tension	[102]
7050Al-T7451	Compact tension	[138]
2519Al-T87	Wedge-opening-load tension	[89]
2024Al-T351	Surface crack tension; compact tension	[147]

investigated the effect of weld imperfections and residual stresses on the fatigue crack propagation (FCP) in FSW 2024Al-T3 and 6013Al-T6 welds using compact tension specimens. Their study revealed following important observations. First, the quality of the FSW welds only exerted limited effects on the $da/dN-\Delta K$ curve. Second, at lower loads and lower R -ratio of 0.1, the FCP properties of the FSW welds were superior to that of the base metal for both 2024Al-T3 and 6013Al-T6, whereas at higher loads or higher R -ratios of 0.7–0.8, base materials and FSW welds exhibited similar $da/dN-\Delta K$ behavior. This was attributed to the presence of compressive residual stresses at the crack tip region in the FSW welds, which decreases the effective stress intensity (ΔK_{eff}) at the crack front. In this case, fatigue crack propagation rates at lower loads and lower R -ratio were apparently reduced due to reduced effective stress intensity. However, at higher loads or higher R -ratios, the effect of the compressive residual stress becomes less important and similar base material and FSW $da/dN-\Delta K$ curves were achieved. Donne et al. [137] further showed that after subtracting the effect of the residual stress, the $da/dN-\Delta K_{\text{eff}}$ curves of the base materials and the FSW welds overlapped. Third, specimen geometry exhibited a considerable effect on the FCP behavior of the FSW welds. Donne et al. [137] compared the $da/dN-\Delta K$ curves obtained by compact tension specimens and middle cracked tension specimens for both base material and FSW weld at a lower R -ratio of 0.1. While the base material curves overlapped, a large discrepancy was found in the case of the FSW welds. This was attributed to different distribution of the residual stresses in two specimens with different geometries.

The improvement in the FCP properties after FSW was further verified in FSW 2519Al-T87 and 2024Al-T351 by Pao et al. [89] and Bussu and Irving [147]. Pao et al. [89] reported that the nugget zone and HAZ of FSW 2519Al-T87 exhibited lower fatigue crack growth rates and higher fatigue crack growth threshold, ΔK_{th} , at both $R = 0.1$ and 0.5, in air and in 3.5% NaCl solution, compared to the base metal. Furthermore, the FCP properties of the nugget zone were higher than those of the HAZ. Compared to the fatigue crack growth rates in air, the fatigue crack growth rates in 3.5% NaCl solution for the base metal, HAZ, and nugget zone, in the intermediate and high ΔK regions, were about two times higher than those observed in air. However, at crack growth rates below about 10^{-8} m/cycle, ΔK_{th} values in 3.5% NaCl solution were substantially higher than those in air because corrosion product wedging became increasingly prevalent and corrosion product induced crack closure progressively lowered the effective ΔK and eventually stopped the crack growth. The ΔK_{th} values obtained in both air and 3.5% NaCl solution are summarized in Table 10. Bussu and Irving [147] reported that crack growth behavior in the FSW 2024Al-T351 joints was generally dominated by the weld residual stress and that microstructure and hardness changes in the FSW welds had minor influence. Furthermore, they reported that fatigue crack growth rates in FSW 2024Al-T351 depended strongly on their location and orientation with respect to the weld centerline. However, in FSW weld

Table 10
Fatigue crack growth threshold, ΔK_{th} (MPa m^{1/2}) of FSW 2519Al and 7050Al alloys

Materials	Condition	Load ratio	Base	Nugget	HAZ	Reference
2519Al-T87	Air	0.10	2.2	6.2	4.8	[89]
	3.5% NaCl	0.10	4.8	8.6	7.2	[89]
7050Al-T7451	Air	0.10	2.0	2.0	5.0	[102] ^a
	3.5% NaCl	0.10	4.0	4.0	5.5	[102] ^a
7050Al-T7451	Air	0.33	1.8	1.0	3.2	[138] ^b

^a FSW weld is in as-FSW + aging (121 °C/12 h) condition.

^b FSW weld is in as-FSW + T6 condition.

which were mechanically stress relieved by application of 2% plastic strain, crack growth rates were almost identical to those of the base metal, irrespective of location and orientation.

On the other hand, in an investigation of fatigue-crack growth behavior of FSW 7050Al-T7451 in the as-FSW + T6 condition at the lower stress ratio of 0.33, Jata et al. [92] observed that the nugget zone had the lowest near-threshold resistance and the HAZ the highest near-threshold resistance (Table 10). At the higher stress ratio of 0.7, the differences in the fatigue crack growth rates of the base metal, nugget zone and HAZ were almost negligible. Jata et al. [92] suggested that the decrease in fatigue crack growth resistance of the nugget zone was due to an intergranular failure mechanism and in the HAZ, residual stresses were more dominant than the microstructure improving the fatigue crack growth resistance. Similarly, Pao et al. [138] found that the HAZ of FSW 7050Al-T7451 in as-FSW + aged (121 °C/12 h) condition exhibited significantly lower fatigue-crack growth and much higher ΔK_{th} at a stress ratio of 0.1 in both air and 3.5% NaCl solution. However, the FCP properties of the weld nugget region were basically identical to those of the base metal in both air and 3.5% NaCl solution. The low fatigue crack growth rate in the HAZ was attributed to residual stress and roughness induced crack closure. Furthermore, Pao et al. [138] reported a significant increase in the ΔK_{th} values in 3.5% NaCl solution for the nugget zone, HAZ, and base metal (Table 10). This observation is similar to that in FSW 2519Al-T87 and attributed to the corrosion product wedging phenomenon.

5.3.3. Fracture toughness

It is usually accepted that all welded structures go into service with flaws ranging from volume defects like porosity, non-metallic inclusions to different planar defects like cracks induced by hydrogen or hot tearing. There are standards for acceptability of the welds pertaining to different inspection codes. The non-acceptable flaws must be repaired before the weld is put into service. Most existing codes cater toward weldments made by conventional welding techniques. FSW is generally found to produce defect-free welds. However, no established code exists so far for FSW. Considering potential applications of FSW, there is a critical need for proper evaluation of the fracture behavior of the friction stir welds. The most commonly used parameters are the crack tip intensity factors (K) for linear elastic loading, and the J integral or the crack opening displacement (CTOD) for elastic–plastic loading [148].

Since the first international symposium on friction stir welding in 1999, several investigations have been conducted to evaluate the effect of FSW on the fracture toughness [40,134,135,149–152]. The materials investigated and the methods used to measure the fracture toughness are summarized in

Table 11
A summary of materials and methods used for evaluating fracture toughness of FSW welds

Materials	Testing method	References
2195Al-T8	Surface crack tension (SCT)	[149,150]
2024Al-T3	Compact tension	[40]
5005Al-H14	Compact tension	[135]
2024Al-T351	Compact tension	[135]
6061Al-T6	Compact tension	[135]
7020Al-T6	Compact tension	[135]
2014Al-T651	Single edge notched bend; Charpy V-notch impact	[134]
7075Al-T651	Single edge notched bend; Charpy V-notch impact	[134]
5083Al-O	Single edge notched bend; Charpy V-notch impact	[134]
6082Al	Constrained Charpy impact	[151]
7108Al	Constrained Charpy impact	[151]
2195Al-T8	Compact tension	[152]

Table 12

Fracture toughness (CTOD(δ_5)_m, mm) of FSW welds and respective base metals obtained by means of compact tension (after von Strombeck et al. [135])

Material	Plate thickness (mm)	Base	FSW	
			Nugget	TMAZ/HAZ
5005Al-H14	3	0.35	1.57	1.40
2024Al-T351	5	0.30	0.22	0.20
6061Al-T6	5	0.28	0.96	0.63
7002Al-T6	5	0.40	0.48	–

Table 11. von Strombeck et al. [135] investigated the fracture toughness behavior of several FSW aluminum alloy by means of compact tension (CT) tests. The fracture toughness values in term of δ_5 CTOD are summarized in Table 12. It is noted from Table 12 that the fracture toughness values of FSW 5005Al-H14, 6061Al-T6 and 7020Al-T6 are much higher than that of respective base metals, whereas FSW 2024Al-T6 exhibited a slightly reduced fracture toughness compared to the base metal (Table 12). Further, Table 12 demonstrates that the fracture toughness of the nugget zone was superior to that of the TMAZ/HAZ region for all alloys. Recently, Dawes et al. [134] measured the fracture toughness of FSW 2014Al-T651, 7075Al-RRA and 5083Al-O by means of single edge notched three-point bend tests as per ASTM E 399-90 and E 1820-99. The CTOD and J values indicate that fracture toughness of the FSW welds are considerably higher than that of the respective base metals for all three alloys (Table 13). The results of Dawes et al. [134] show that the fracture toughness of the nugget zone is not always higher than that of the HAZ/TMAZ region, which is different from the results reported by von Strombeck et al. [135]. More recently, Kroninger and Reynolds [152] studied the R -curve behavior of FSW 2195Al-T8 welds by using compact tension specimens and compared it

Table 13

Fracture toughness of FSW welds and respective base metals near the onset of stable crack extension obtained by means of single edge notched bend (after Dawes et al. [134])

Material	Notched region	CTOD (mm),	J (kJ/m ²),
		$\delta_{0.2BL}$ ^a	$J_{0.2BL}$ ^a
2014Al-T651	Base metal	0.011	6.6
	Center of weld nugget	0.060	22
	HAZ/TMAZ	0.065	27
	HAZ/TMAZ	0.049	20
	TMAZ 0.5 mm from the edge of weld nugget on advancing side	0.051	17
7075Al-RRA ^b	Base metal	0.012	9.5
	Center of weld nugget	0.024	12.7
	HAZ/TMAZ	0.082	30
	HAZ/TMAZ	0.084	31
	TMAZ 0.5 mm from the edge of weld nugget on advancing side	0.036	17.2
5083Al-O	Base metal	0.159	47
	Center of weld nugget	0.201	64
	HAZ/TMAZ	0.177	50
	HAZ/TMAZ	0.201	59

^a $\delta_{0.2BL}$ and $J_{0.2BL}$ are very similar to the δ_{Ic} and J_{Ic} fracture toughness, respectively, in the ASTM E 1820-99 test method.

^b RRA refers to retrogression and re-aging (rapid heating to 220 °C, kept for 5 min, cold water quenched, re-aged at 120 °C for 24 h).

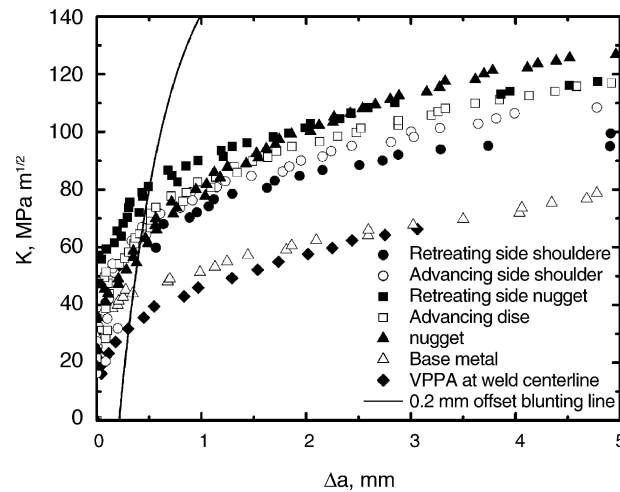


Fig. 33. Representative R —curves for all 2195Al FSW crack planes, 2195 base metal, and centerline crack in the VPPA weld (after Kroninger and Reynolds [152]).

with that of the weld made by a variable polarity plasma arc (VPPA). Representative R -curves are shown in Fig. 33 for the FSW welds, base metal, and VPPA weld. It is evident from Fig. 33 that the FSW specimens exhibited higher crack resistance than the base metal at both large and small crack extensions (initiation and tearing resistance). By comparison, the VAAP weld R -curve exhibited a very low initiation resistance but achieved similar tearing resistance to the base metal at larger crack extensions. The reason for higher fracture toughness associated with the FSW welds is attributed to the fracture and rounding of large primary particles by the stirring process [150], and the softening of the matrix [152].

On the other hand, Oosterkamp et al. [151] investigated the initiation fracture toughness behavior of FSW 6082Al and 7108Al welds by means of constrained Charpy impact test (CCIT). The CCIT is a variation of instrumented Charpy impact test with deep side grooves as a constraint to plasticity. Two types of notches (machined V-notch and machined V-notch extended in fatigue) and two impact speeds (3 and 10 m/s) were used in CCIT. It was reported that the fracture toughness of FSW 6082 Al welds is similar to the base metal, whereas FSW 7108Al exhibited much higher values of fracture toughness as compared to the base material.

It should be pointed out that no detailed microstructure–property correlation has been established so far for the fracture toughness of FSW welds. Since microstructures are changed significantly during FSW, it is important to understand the influence of microstructural characteristics on the fracture toughness of friction stir welds. For commercial precipitation-strengthened high-strength aluminum alloys, three types of particles are identified, i.e., large constituent particles (5–30 μm), dispersoids (0.2–0.5 μm), and precipitates in the nanometric size range [153]. In the absence of constituent particles and dispersoids, the deformation behavior becomes strongly influenced by shearing of precipitates, thus, leading to strain localization. Jata and Starke [154] developed an equation to relate plane strain fracture toughness (K_{Ic}) and strain localization in the matrix given by

$$K_{Ic} = \left[8 \sin \alpha E \sigma_y W \left(\frac{D}{S_{SB}} \right) \varepsilon_{SB}^c \right]^{1/2}, \quad (4)$$

where α is the average angle between the microscopic crack path and direction of the slip band extending from the crack tip, E the Young's modulus, σ_y the yield stress, W the width of the slip band, S_{SB} the slip band spacing, and ε_{SB}^c is the critical strain for fracture. Further, Graf and Hornborg [155]

proposed a relation for 7075Al, which fails by pseudo-intercrystalline fracture, given by

$$K_{Ic} = \left[\frac{E\sigma_{PFZ}\varepsilon_f d_{PFZ}}{CS_{SB}} \right]^{1/2}, \quad (5)$$

where d_{PFZ} is the width of precipitate-free zone at the grain boundaries, ε_f the fracture strain, σ_{PFZ} the yield stress at PFZ, and C is a constant. Like the conditions of strain localization in the matrix, it was found that low fracture toughness results from the presence of a narrow and soft PFZ and a large grain size.

Van Stone et al. [156] suggested that the most critical stage in controlling fracture toughness is the control of the initiation of voids. It is considered that particles provide interfaces that are easy initiation sites for voids. Critical stress for particle cracking, σ , is related to their size, d , and surface energy, γ , by the form [157]:

$$\sigma = \left(\frac{6\gamma E}{q^2 d} \right)^{1/2}, \quad (6)$$

where q is the stress concentration factor at the particle. Clearly, both the increase in the bonding strength between matrix and particles and the decrease in particle size tend to increase critical stress for particle cracking, thereby enhancing the fracture toughness. Improvement in fracture toughness is often achieved by reducing iron and silicon content in aluminum alloys, thus, reducing the volume fraction and size of constituent particles.

Apart from above-mentioned factors, the nature of grain boundaries is considered as another important factor influencing fracture behavior of a material. For example, Watanabe [158] suggested that a large fraction of low energy grain boundaries might toughen the material by changing the failure mode from intergranular to transgranular fracture. However, these concepts are still evolving and no quantitative relation is available to predict fracture toughness based on grain boundary character distribution.

Based on above-mentioned microstructural analyses, the fracture toughness of FSW aluminum alloys can be rationalized. FSW results in generation of a nugget zone characterized by: (a) very fine grain size [4–6,75–89], (b) fine precipitates and constituent particles [88], (c) lower yield stress [41], and (d) high ratio of high-angle boundaries [14]. Fine grain structure and small particles tend to enhance the fracture toughness of nugget zone, whereas low yield stress and high ratio of high-angle boundaries tend to reduce the fracture toughness. The overall impact of these factors is that the fracture toughness of nugget zone is higher than or comparable to that of base material, depending on the alloy chemistry and FSW parameters [134,135,151,152]. The lower fracture toughness in the HAZ/TMAZ region than in the nugget zone is attributed to widened PFZ and coarsened particles [75,84,98].

5.4. Corrosion behavior

As discussed in Section 4, FSW results in generation of various microstructural zones, i.e., the nugget zone, the TMAZ, and the HAZ. These zones exhibit different microstructural characteristics such as grain size and dislocation density, residual stress and texture, and precipitate size and distribution. Therefore, it is expected that the various microstructural zones will exhibit different corrosion susceptibility. For practical applications, it is very important to understand corrosion behavior of the FSW welds and elucidate the prevailing mechanisms for corrosion in various FSW alloys and various microstructural zones. In the past few years several studies were conducted with the

Table 14
Investigated FSW materials and used corrosive solutions by various investigators

FSW material	Corrosive solution	Reference
5454Al-O, 5454Al-H34	0.1 M NaCl, 0.5 M NaCl	[77]
2024Al-T4, 2195Al	0.6 M NaCl	[159]
5083Al-T3	EXCO (4 M NaCl–0.5 M KNO ₃ –0.1 M HNO ₃), 3.5% NaCl–0.3 g/l H ₂ O ₂	[160]
7075Al-T6, 2219Al-T87, 2195Al-T87	3.5% NaCl	[161]
7075Al-T651	Modified EXCO (4 M NaCl–0.5 M KNO ₃ –0.1 M HNO ₃ diluted to 10%)	[162]
7010Al-T7651, 2024Al-T351	0.1 M NaCl, 0.1 M HCl, ASTM G85 salt spray	[163]
7075Al-T651, 7050Al-T7451	NaCl + H ₂ O ₂ , 3.5%NaCl	[164]
7075Al-T6	3.5% NaCl	[165]
2024Al-T3	3.5% NaCl	[40]
7050Al-T7651	Modified EXCO (4 M NaCl–0.5 M KNO ₃ –0.1 M HNO ₃ diluted to 10%)	[166]
Al–Li–Cu AF/C458	57 g NaCl + 10 ml H ₂ O ₂ + 1 l H ₂ O	[167]

aim to understand the effect of FSW on the corrosion and stress corrosion cracking (SCC) [40,77,159–167]. The alloys and corrosive solutions used in various studies are summarized in Table 14.

5.4.1. Corrosion characteristics

Frankel and Xia [77] were first to investigate pitting and stress corrosion cracking behaviors of FSW 5454Al and compare them with those of base alloy and GTAW samples. Their study revealed following important observations. First, the pits in FSW samples formed in the HAZ, whereas in GTAW samples the pits formed in the large dendritic region just inside the fusion zone. Second, FSW welds showed a pitting resistance higher than those of base alloy and GTAW welds as shown in Table 15. Frankel and Xia [77] pointed out that although the differences in pitting potential were not very large, the trend of higher pitting potential for FSW samples was observed consistently. Third, in stress corrosion cracking (SCC) tests using U-bent specimens, base alloy and FSW welds did not show SCC susceptibility in 20 days tests in 0.5 M NaCl solution, even if polarized at +60 mV in respect to corrosion potential. However, GTAW U-bent specimens cracked at the same conditions. Fourth, slow strain rate tests (SSRT) revealed that both base metals and FSW and GTAW welds, anodically polarized, exhibited a reduction in ductility, indicating a certain SCC susceptibility. However, the reduction in ductility for FSW welds was lower than that for GTAW welds. The lowest ductility of FSW 5454Al-H34 in both air and solution was attributed to a defect associated with some remnant of original interface. The breakup of the original interface depends on the process parameters as well as tool design. It is important to completely breakup and distribute the oxide surface layer to avoid crack nucleation sites.

The experimental observations that the pitting and SCC resistances of FSW welds were superior or comparable to those of the base material were also recently reported by Corral et al. [159], Zucchi et al. [160], and Meletis et al. [161]. Corral et al. [159] investigated the effect of FSW on the corrosion behavior of a very common heat-treatable aircraft aluminum alloy (2024Al-T4) and a so-called third-

Table 15
Pitting potentials of 5454Al-O base and welds ground with 600 grit in 0.1 M NaCl solution (mV_{SCE}) (after Frankel and Xia [77])

Condition	Base-L	FSW top	FSW bottom	GTAW top	GTAW bottom	5356Al filler metal
Deaerated	–680	–650	–650	–740	–690	–730
Aerated	–680	–670	–690	–730	–	–

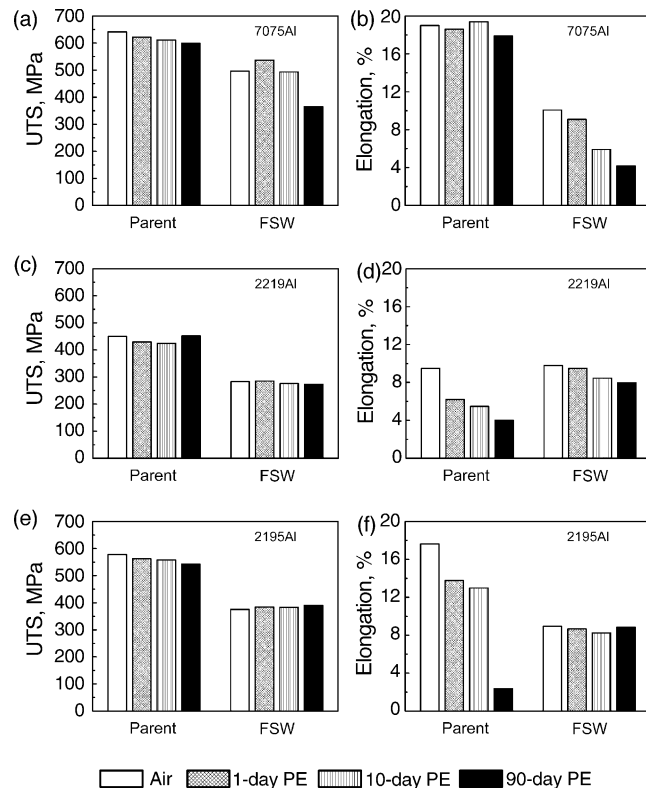


Fig. 34. Tensile strength and ductility from SSRT for FSW aluminum alloys and base metals: (a, b) 7075Al, (c, d) 2219Al, and (e, f) 2195Al (after Meletis et al. [161]).

generation Al–Li alloy (2195Al). Anodic polarization curves showed that the diffusion-limiting current densities and corrosion potentials of both 2024Al and 2195Al FSW welds were nearly identical to those of the base alloys for a 0.6 M NaCl solution. Furthermore, static immersion tests for 20 h and 25 days showed an even amount of by-product build-up both on the FSW zones and base metal sections.

Similarly, Zucchi et al. [160] reported that the 5083Al FSW weld exhibited a higher corrosion resistance in EXCO solution (4 M NaCl–0.5 M KNO_3 –0.1 M HNO_3) and a lower pitting tendency than the base alloy. Further, a higher pitting potential and a lower cathodic current were observed in the FSW weld than in the base alloy. Additionally, SSRT showed that FSW joint was not susceptible to SCC in both EXCO and 3.5% NaCl + 0.3 g/l H_2O_2 solutions. In comparison, MIG joints were susceptible to SCC in both solutions.

More recently, Meletis et al. [161] investigated SCC behavior of FSW 7075Al-T6, 2219Al-T87, and 2195Al-T87 by two types of experiments: (a) four-point bending at different loading levels under alternate immersion (AI) conditions in 3.5% NaCl solution for 90 days, and (b) slow strain rate tension of specimens pre-exposed (PE) under AI in 3.5% NaCl solution. Four-point bending results revealed that no stress corrosion cracks were present in these samples, indicating no SCC susceptibility for any of the FSW alloys for the given exposure period and loading levels. The SSRT results are shown in Fig. 34. Fig. 34 shows that under more severe SSRT experiments, FSW 2219Al and 2195Al still showed no SCC susceptibility, whereas FSW 7075Al showed a reduced ductility with increasing PE time. Meletis et al. [161] suggested that the observed environmental susceptibility in FSW 7075Al was due to hydrogen embrittlement.

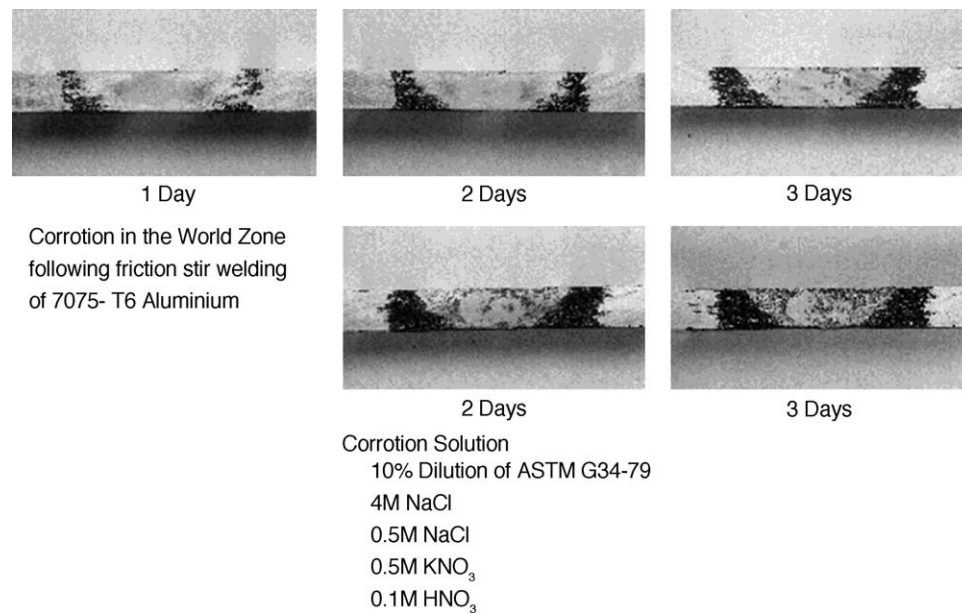


Fig. 35. Corrosion attack of FSW 7075Al-T651 following extended exposure to a solution of 4 M NaCl–0.5 M KNO₃–0.1 M HNO₃ diluted to 10% (after Lumsden et al. [162]).

The investigations by Lumsden et al. [162,166], Hannour et al. [163] and Paglia et al. [164] demonstrated that FSW welds of 7075Al, 7010Al, 2024Al, and 7050Al were more susceptible to intergranular attack than the base alloy. Fig. 35 showed a typical example of corrosion attack of 7075Al-T651 following extended exposure to a modified EXCO solution (4 M NaCl–0.5 M KNO₃–0.1 M HNO₃ diluted to 10%). It is evident that after 24 h exposure to the modified EXCO solution, the corrosion was very localized in the HAZ, including the outer edges of the TMAZ, and neither the base alloy nor the weld nugget showed evidence of corrosive attack (Fig. 35a). For extended exposure times, the intergranular attack became more severe in the initial attack region and attack region spread to whole TMAZ previously unattacked (Fig. 35b and c). Finally, the intergranular attack was also developed in the nugget zone (Fig. 35d and e). However, no intergranular corrosion was detected in the parent metal. Similar results were also reported by other investigators in FSW 7075Al-T651, 2024Al-T351, 7010Al-T7651 [163,164], namely intergranular attack occurred preferentially in the HAZ adjacent to the TMAZ. Paglia et al. [165] further verified that the HAZ in the retreating side exhibited higher susceptibility than that in the advancing side. However, Biallas et al. [40] and Paglia et al. [164] reported that preferential corrosion attack occurred in the TMAZ for FSW 2024Al-T3 and in the TMAZ-nugget interface for FSW 7050Al-T7451. Table 16 summarizes the comparison between pitting potentials of several FSW aluminum welds in different locations. Clearly, the pitting potential of corrosion zone was not only significantly lower than that of the base alloy, but also lower than that of

Table 16
Pitting potentials of FSW aluminum alloy welds in different locations (mV_{SCE})

Material	Corrosion zone	Weld nugget	Base metal	Reference
7075Al-T651	–798	–772	–758, –713 ^a	[75]
7010Al-T7651	–712	–704	–686	[159]
2024Al-T351	–638	–566	–540	[159]

^a 7075Al base has two pitting potentials.

the nugget zone for all FSW aluminum welds. These studies indicated that the hottest regions within the HAZ were the most susceptible to intergranular corrosion and had the lowest pitting potential followed by the nugget. Microstructural examinations on the hottest regions of the HAZ revealed significant Cu depletion at grain boundaries. Based on the experimental observations, Lumsden et al. [162] attributed the mechanism of intergranular corrosion to a Cu depletion model linking intergranular corrosion with pitting corrosion. This is consistent with previous studies that the pitting potential decreases with a decrease of Cu [168,169]. Furthermore, widened PFZs, coarse grain boundary phases and coarse intragranular precipitates in the HAZ were also considered responsible for the preferential corrosion in the HAZ [163,164].

It should be pointed out that in addition to alloy chemistry, both residual microstructure in FSW welds and corrosion medium exert a significant effect on the corrosion behavior of FSW aluminum alloys. This is why contradictory trends were reported for 2024Al [40,159,163]. This requires further research to establish the dominating factors influencing corrosion properties of FSW welds.

5.4.2. Treatments to improve corrosion resistance

The corrosion susceptibility of the high-strength aluminum FSW welds is a concern for wide range of engineering applications of FSW. A few postweld treatments have been evaluated to improve the corrosion resistance of FSW welds [166,170–173]. Hannour et al. [170] and Williams et al. [171] investigated the effect of postweld surface laser treatment on corrosion resistance of FSW aluminum welds. Corrosion tests and electrochemical studies indicated that the excimer laser treatment led to a remarkable improvement of the corrosion resistance of FSW welds in 2024Al-T351 and 7010Al-T651 with lower cathodic current density and higher pitting potential [170,171]. Intergranular corrosion within the HAZ was suppressed with corrosion occurring instead through the general pitting attack of the untreated parent material [171]. This was attributed to the development of a more homogenous surface layer of $\sim 10 \mu\text{m}$ with a reduction in the undesirable precipitate and a change in the grain boundary chemistry [170,171].

Recently, Paglia et al. [172] studied the effect of postweld heat treatment on the corrosion resistance of FSW 7075Al alloy. A torch treatment (exposing each side of the FSW weld to a torch flame for 1 min at a distance of $\sim 20 \text{ mm}$ and water quench) resulted in a slight disappearance of the

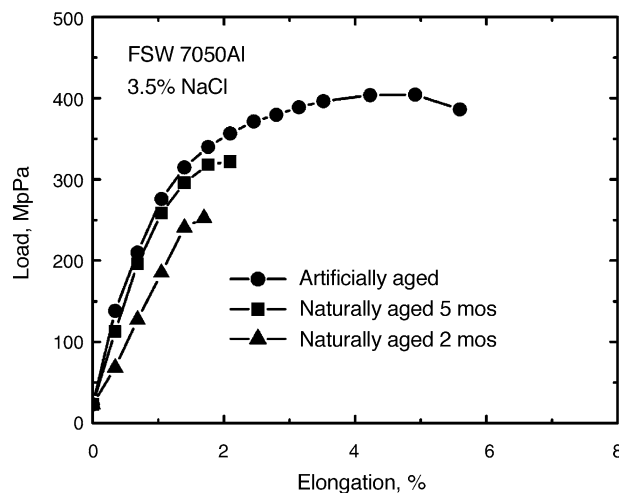


Fig. 36. Stress–strain curves for naturally and artificially aged FSW AA7050Al-T7651 tested at slow strain rate of $1 \times 10^{-6} \text{ s}^{-1}$ in a 3.5% NaCl solution (after Lumsden et al. [166]).

intragranular precipitates and the general disappearance of the grain boundary phases, in particular for the HAZ, thereby decreasing the intergranular corrosion susceptibility and increasing the stress corrosion cracking resistance.

More recently, Lumsden et al. [166,173] investigated the effect of postweld heat treatment on the corrosion properties of FSW 7050Al-T7651. Fig. 36 shows typical stress-strain results for naturally and artificially aged FSW joints tested at 10^{-6} s^{-1} in a 3.5% NaCl solution. Clearly, an artificial aging at 100 °C for 1 week restored a significant amount of the SCC resistance. Other artificial aging treatments investigated also restored the SCC resistance, but caused an unacceptable loss in mechanical properties under ambient conditions. Similarly, Merati et al. [174] reported that a local heat treatment (stabilization heat treatment + retrogression and re-aging) was the most promising type of heat treatment to restore SCC resistance.

6. Material specific issues

The rapid development of the FSW process in aluminum alloys and its successful implementation into commercial applications has motivated its application to other non-ferrous materials (Mg, Cu, Ti, as well as their composites), steel, and even thermoplastics. However, a possible obstacle to the commercial success of FSW in high-temperature materials such as titanium and steel is in the identification and/or development of suitable tool materials and advantages over the current welding methods. Unlike high-strength aluminum alloys which are unweldable by most fusion welding techniques, titanium alloys and steels can be welded by various fusion techniques and high welding efficiencies can be achieved. Therefore, it is not only important to show the feasibility of FSW, but also to delineate its advantages over other techniques. Furthermore, FSW of dissimilar alloys/metals has attracted extensive research interest due to potential engineering importance and problems associated with conventional welding. In the following sections, the development of FSW in other materials and material specific issues are reviewed.

6.1. Copper alloys

Welding of copper is usually difficult by conventional fusion welding techniques because of its high thermal diffusivity, which is 10–100 times higher than that of steels and nickel alloys. Therefore, the heat input required for welding is much higher, resulting in quite low welding speeds. Recently, several attempts have been made to join pure copper and 60/40 brass via FSW process [175–179]. Table 17 summarizes plate thickness, tool materials, and FSW parameters for FSW. Copper plates of 1.5–50 mm thickness were successfully friction stir welded [175–179].

Some important observation can be made from the above studies. First, tool material and tool geometry exerted a significant effect on feasibility of FSW of thick copper plates. Andersson and coworkers [175,176] showed that the pin made from high-temperature tool steel with a parallel profile could be used to join 3 mm thick copper plate, but was unsuitable for FSW of 10 mm thick plate due to the filling of the finely machined features with copper and the softening of the tool steel above 540 °C. A sintered tungsten-based alloy tool with improved geometry was much more effective for FSW of 10–25 mm thick copper plates. Furthermore, they tried a new pin design and used different high-temperature tool materials. The tool was strong enough to weld the copper plates of >30 mm thickness. However, Andersson and Andrews [175] did not provide the details of tool material and tool design. Hautala and Tiainen [177] reported that steel (QRO90) and Inconel were suitable tool materials for FSW of copper, but sintered carbide (K40UF) was too brittle for FSW of copper.

Table 17
A summary of FSW of copper alloys

Materials	Plate thickness (mm)	Tool materials	Rotation rate (rpm)	Traverse speed (mm/min)	References
Pure copper	3.0	Tool steel			[175,176]
Pure copper	10–25	Sintered tungsten-based alloy			[175,176]
Pure copper	10–50	High-temperature materials with specific geometry design			[175,176]
Oxygen-free copper	1.5–5.0	Sintered carbide ISO K40UF (WC–Co), Ni-based superalloy (Inconel 718), Cr–Mo–V type hot work tool steel (QRO90)	375–1250	250–400	[177]
Pure copper	4	–	1250	61	[178]
60/40 brass	2	–	250–1500	500–2000	[179]

Second, welding parameters had a considerable influence on joint quality of FSW copper. Park et al. [179] reported that while sound joints of FSW 60/40 brass can be achieved in a relatively wide range of FSW parameters, it is found that the frequency of generation of FSW defects of a groove-type void increased with increasing welding speed at a constant tool rotation rate of 500 rpm or with a decrease in tool rotation rate from 500 to 250 rpm.

Third, the observations on microstructural zones differ. While Andersson and Andrews [175] and Hautala and Tiainen [177] reported the existence of three microstructural zones in FSW pure copper joints, i.e., the nugget zone with fine recrystallized grains, the TMAZ with deformed large grains, and the HAZ with equiaxed grains larger than those of the base metal, Lee and Jung [178] reported that no distinct TMAZ was identified in copper welds. Furthermore, in FSW 60/40 brass joints, Park et al. [179] reported that no distinct HAZ was observed.

Fourth, FSW copper alloys exhibited tensile strengths comparable to that of the base materials. For FSW pure copper, it was reported that transverse tensile strength of the welds was slightly lower than that of base metal [175–178]. However, FSW joints showed a slightly higher tensile strength compared to the EBW joint [180]. Further, the strength of FSW copper increased with decreasing tool shoulder diameter and tool rotation rate or increasing tool traverse speed [177]. For FSW 60/40 brass, Park et al. [179] reported an increase in tensile strength of the welds compared to the base metal. With increasing welding speed, the tensile strength of the welds increased and the percent elongation decreased.

Fifth, some properties of the welds achieved by FSW and GTAW are similar [177]. For example, the amount of dissolved gases (O_2 and H_2) is similar for both FSW and GTAW welds, though the GTAW was conducted with a shielding gas (helium) and in FSW no shielding gas was used [177]. Both FSW and GTAW reduced the conductivity by the same amount ($\sim 5\%$). The thermal stability of FSW copper is similar to that of base copper and GTAW copper.

From the limited preliminary investigations, it is clear that FSW has potential for joining of copper.

6.2. Titanium alloys

Although many titanium alloys are readily welded using conventional fusion processes such as GTAW, they may also require postweld heat treatment, an added process step that increases production costs [181]. As a solid-state welding process, FSW is expected to eliminate the necessity for postweld heat treatment. Unfortunately, information on FSW of titanium alloy is very limited so far [182–186].

Juhas et al. [182,183] and Lienert et al. [184] examined the effect of FSW on microstructural evolution and properties of Ti–6Al–4V. Juhas et al. [182,183] obtained Ti–6Al–4V friction stir welds

from the Edison Welding Institute (EWI) and TWI, and reported results without details of tool material and geometry or the welding conditions, whereas Lienert et al. [184] only reported results for welding speed of 101.6 mm/min. These studies revealed following important observations. First, defect-free Ti–6Al–4V FSW joints were produced. Second, generally, there is an absence of an apparent TMAZ [182–184], which is typically observed in the FSW aluminum alloys [4,41,61], though Ramirez and Juhas [185] identified the existence of very narrow TMAZ of $\sim 30 \mu\text{m}$. Third, thermocouple attached to the circumference of the tool at 3.2 mm above the shoulder recorded a peak temperature of 990°C [184]. This implied that the peak temperature in the nugget zone could exceed 1000°C , which is above the β transus temperature of 995°C . Microstructural characteristics of the nugget zone also suggested that the peak temperature surpassed the β transus temperature [182–185]. However, the peak temperature experienced in the HAZ was believed to be below the β transus temperature [182–185]. Fourth, allotropic phase transformation in titanium alloys coupled with deformation and continuous cooling produces complex weld microstructures compared to those observed in aluminum alloy friction stir welds. Juhas et al. [182,183] reported that while the microstructure of the nugget from EWI was characterized by a combination of equiaxed α phase and colonies of α laths (transformed β) bounded by β ribs [182], the weld from TWI exhibited a typical Widmanstätten structure [183]. The former indicated that the welds experienced a relatively slow cooling rate from a temperature above the β transus, whereas for the latter cooling occurred rapidly enough to produce a refined Widmanstätten structure. On the other hand, Lienert et al. [184] reported that the nugget zone consisted of equiaxed grains of fine acicular α phase resulting from a relatively rapid cooling rate. Fifth, no hardness troughs were observed in the HAZ of FSW Ti–6Al–4V. The hardness troughs are usually observed in the HAZ of titanium alloy fusion welds in which softening is produced due to localized growth of the prior β grains [187]. However, the hardness profiles across the Ti–6Al–4V FSW joints were different for various studies. Juhas et al. [182,183] reported that for the FSW weld from the EWI the hardness profiles showed a slight softening trend in the nugget zone, whereas for the weld from TWI a distinct increase in hardness over the base metal was observed across the nugget zone. On the other hand, Lienert et al. [184] reported that microhardness increased from approximately 340 VHN in the base metal and nugget zone to 370 in the HAZ. Clearly, different hardness profiles across the weld nugget should be associated with the different microstructural characteristics revealed in these studies. Sixth, tool wear took place with the greatest amount of wear and deformation of the tool occurring during plunging [186].

Table 18 shows the transverse tensile properties of FSW Ti–6Al–4V and base metal reported by Lienert et al. [184]. Clearly, the welds exhibited 100% joint efficiency with respect to both yield and tensile ultimate strengths. Furthermore, the ductility of the welds compares favorably with that of the base metal. Standard deviations were relatively small for strength and elongation values indicating repeatable results. Failure of transverse tensile specimens occurred in the base metal. More recently, Trap et al. [186] reported that the strength of Ti 17/Ti 6-4 FSW welds were as strong or stronger than the Ti 6-4 base metal at both room temperature and 316°C .

While preliminary investigations indicate that FSW is potentially an effective welding technique for joining of titanium alloys, obviously more research is needed to understand the microstructural evolution of titanium alloys during FSW and operative mechanisms. Two critical issues should be

Table 18

Transverse tensile properties of FSW Ti–6Al–4V and base metal at room temperature (after Lienert et al. [184])

Material	YS (MPa)	UTS (MPa)	Elongation (%)	Failure location
Base metal	897.0 ± 0.7	957.7 ± 3.4	12.7 ± 0.5	NA
FSW	912.9 ± 8.3	1013.6 ± 8.3	12.7 ± 0.9	Base

specifically investigated. First, control of process temperatures and cooling rates is required for FSW of α/β titanium alloys to optimize the microstructure. Second, tool materials suitable for high-temperature (~ 1000 °C) FSW process should be selected and tool geometry design optimized.

6.3. Steels

While most of FSW efforts to date have focused on aluminum alloys, there is a considerable interest in it for steels. The lower heat inputs associated with FSW (relative to fusion welding processes) are expected to produce less metallurgical changes in the HAZ and to minimize distortion and residual stresses in steels, which is extremely important in welding of thick-section components, such as in the shipbuilding and heavy manufacturing industries. Furthermore, problems with hydrogen cracking in steels would be eliminated due to the solid-state nature of the FSW process. Additionally, the solid-state FSW process eliminates the welding fumes, especially those containing hexavalent Cr, to allow compliance with OSHA standards [188]. These advantages are likely to make FSW attractive for joining steel in many applications.

Some FSW studies were recently conducted on low carbon steel and 12% chromium alloy steel [189], mild steel AISI 1010 [190,191], austenitic stainless steel 304L [105,192–195] and 316L [195], superaustenitic stainless steel Al 6XN [192,196], HSLA-65 (ASTM A945) [197], DH-36 [196,198], and C–Mn [199]. The plate thickness and the FSW parameters and tool materials for FSW process are summarized in Table 19. These studies resulted in following important observations. First, generally, argon was used as the shielding gas to protect both the tool and the weld area from oxidation in FSW of steels [107,191,194–197]. However, some investigations did not reveal if shielding gas was used [189,190,192,196,199]. Further, no study was reported on the effect of shielding gas on quality of FSW steel joints. Second, Thomas et al. [189] reported that the temperature of the tool shoulder was over 1000 °C and that of the ensuing weld track behind the trailing edge of the rotation tool was 900–1000 °C. Similarly, peak temperature of >1000 °C was observed by Lienert et al. [191] just above the tool shoulder by both thermocouples and infrared camera. Based on extrapolation of measured temperature and microstructural evidence, Lienert et al. [191] suggested that the peak temperature of the stirred zone exceeded 1100 °C and likely surpassed 1200 °C. Furthermore, the thermal model by Lienert and Gould [190] also predicted that temperature throughout the weld zone exceeded 1000 °C. Third, while most of 3.2–6.4 mm thick steel plates can be successfully welded in a single pass, welds in 6.4 mm thick 304L steel plate and steel plates of >6.4 mm were usually made with two passes from

Table 19
FSW parameters and tool materials for FSW of steels

Materials to be welded	Plate thickness (mm)	Tool rotation rate (rpm)	Tool traverse speed (mm/min)	Tool materials	References
12% Cr steel	12	–	240	–	[189]
Low carbon steel	12, 15	–	102	–	[189]
AISI 1010	6.4	450–650	25–102	Mo and W-based alloys	[190,191]
304L	3.2, 6.4	300, 500	102	W alloy	[104,192,193]
304	6.0	550	78	Polycrystalline cubic boron	[194]
304L, 316L	5, 10	300–700	150, 180	–	[195]
Al 6XN	6.4, 12.7	–	102	W alloy	[192,196]
HSLA-65	6.4, 12.7	400–450	99–120	W	[197]
DH-36	6.4	–	102–457	W alloy	[196,198]
C–Mn	6.4	–	–	Polycrystalline cubic boron nitride	[199]

two sides because the range of influence of the tool is relatively small in the steels compared to aluminum alloys [107,189–195]. Preheating of both the tool and steel plates to ~ 300 °C facilitated joining of 6.4 mm thick HSLA-65 steel plates in a single pass [196]. Fourth, generally, the TMAZ typically observed in FSW aluminum alloys is not evident in FSW steels due to transformations during FSW thermal cycle [191,197,199]. However, Park et al. [194] and Johnson and Threadgill [195] identified an existence of the TMAZ in FSW 304 and 316L. Park et al. [194] reported that the TMAZ in FSW 304 was characterized by recovered microstructure, whereas Johnson and Threadgill [195] observed the evidence of partial recrystallization in the TMAZ of FSW 304L and 316L. Fifth, the microstructural evolution of steels during FSW is more complicated than that of aluminum alloys due to the occurrence of transformation, recrystallization, as well as grain growth at a high temperature of 1000 °C or above. These changes are significantly influenced by alloy chemistry. For austenitic stainless steels [192], it was reported that equiaxed grain structure developed within the weld nugget with significant grain refinement, up to one order of magnitude relative to the base metal. However, for mild steel, 12% chromium steel, and HSLA-65 steel, depending on FSW temperature and alloy composition, different microstructures were observed in the welds [189,190,197,198]. For example, Konkol et al. [197] reported that FSW resulted in a microstructural change from fine equiaxed ferrite with a small amount pearlite in the base HSLA-65 steel to coarse blocky ferrite, Widmanstätten ferrite, and pockets of ferrite/carbide aggregate in the stirred zone. Furthermore, fine equiaxed ferrite grain structure with fine and randomly distributed pearlite packets was revealed in the HAZ between the stirred zone and the base metal [197]. On the other hand, Reynolds et al. [198] reported that for FSW DH-36 steel, the nugget zone was made up of bainite and martensite. The inner HAZ, which borders the nugget zone, had a grain-refined ferrite structure with small amount of pearlite and martensite. The outer HAZ, between the inner HAZ and the unaffected base metal, had an equiaxed grain structure with a grain size substantially larger than the inner HAZ and slightly larger than the base metal. Sixth, in general, the friction stir welds exhibited satisfactory hardness, transverse tensile properties, bend properties, and Charpy V-notch toughness [189–191,193,196–198]. Transverse tensile tests showed that the yield and ultimate tensile strengths of the welds are generally higher than those of the base metal with failure occurring in the parent metal, well away from the joint or the HAZ, whereas the ductility is comparable to that of the base metal (Table 20). The hardness of the welds is also much higher than that of the base metal [189–193,196], which is consistent with the tensile strength values. Furthermore, transverse 180° side bends of the welds can be easily achieved, indicating good bend properties [189–191]. On the other hand, Sterling et al. [199] reported that in a quenched and tempered C–Mn steel, FSW resulted in decrease of hardness in the weld nugget and tensile properties, with fracture occurring at the HAZ. However, the as-welded strengths of FSW C–Mn steel were superior to those observed in GMAW using ER100S-1 filler metal.

The early investigations on the FSW feasibility of steels have demonstrated a promising prospect for application of FSW for joining of various types of steels. In addition to continuous efforts to optimize the FSW parameters and understand the microstructural evolution during FSW, a critical issue is to identify the choice of suitable tool materials for FSW of steels. An essential requirement for FSW is to maintain a suitable differential between the hardness and elevated-temperature properties of the tool and the workpiece material. Because steels have much higher hardness and elevated-temperature properties, it is important to select tool materials with good wear resistance and toughness at temperatures of 1000 °C or higher. While Thomas et al. [189], Lienert and Gould [190], and Johnson and Threadgill [195] did not identify the tool materials in their studies, tungsten alloy, molybdenum alloy, and polycrystalline cubic boron nitride (PCBN) were used as tool materials by other investigators [107,191–194,196–198]. Lienert and Gould [190] and Lienert et al. [191] reported that most of the tool wear appeared to occur during the initial plunge period at the start of each weld, and

Table 20
Transverse tensile properties of FSW welds in various steels at room temperature

Materials	Conditions	UTS (MPa)	YS (MPa)	Elongation (%)	Reduction in area	References
12% Cr steel	Base metal	–	–	–	–	[189]
	FSW welds	539–541	–	–	–	
Low carbon steel	Base metal	–	–	–	–	[189]
	FSW welds	453–457	–	–	–	
AISI 1010	Base metal	463	310	33.9	22	[190,191]
	FSW welds	476	331	22	31	
304L	Base metal	483	172	–	–	[196]
	FSW welds	621	340	–	–	
HD-36	Base metal	579	428	–	–	[196]
	FSW welds	624	566	–	–	
HSLA-65	Base metal	537	448	20	–	[196]
	FSW welds (12.7 mm)	569	493	30	–	
	FSW welds (6.4 mm)	569	483	18.5	–	
C–Mn steel	Base metal	248	204	9.5	–	[199]
	FSW welds	179	151	2.6	–	
	GMA welds	136	126	5.5	–	

both rubbing wear and deformation of the tool were suggested as the origin of the changes in tool dimensions. Furthermore, Lienert and Gould [190] reported that the tools were replaced after they were used to produce 1.5–2.0 m of weld. However, Sterling et al. [199] reported that PCBN FSW tool only exhibited very little wear after 6 m of welding of a quenched and tempered C–Mn steel. Clearly, more research efforts should be directed to the tool wear and identification/development of suitable tool materials/geometries. Furthermore, as pointed out previously by Thomas et al. [189], preheating of workpieces before welding should be beneficial for improving welding speed and minimizing tool wear. It may be more simple and practical to preheat the initial plunge region of the workpieces before plunging the pin into the workpieces because the tool wear mainly occurred during the initial plunge period at the start of each weld [190,191].

6.4. Magnesium alloys

As magnesium alloys generally have inferior formability, sheet material of magnesium alloys is made commercially by casting or die casting processes except some wrought alloys such as AZ31. It is usually difficult to weld these cast magnesium alloys due to the porosity formation in the weld [200]. Furthermore, relatively large coefficient of expansion of magnesium alloy causes large deformation/distortion of the weld. Therefore, solid-state welding technique should be the optimum choice for joining cast magnesium alloy sheets.

FSW studies have been recently reported on AM50, AM60, AZ91 AZ61, and AZ31. The FSW parameters and the plate thickness for FSW process are summarized in Table 21. These studies resulted in following important observations. First, the quality of FSW welds of magnesium alloys is highly sensitive to tool rotation rate and traverse speed. Nakata et al. [203] reported that optimum parameter for FSW of thixomolded AZ91D sheet is limited to a narrow range of FSW parameters, i.e., higher tool rotation rates and lower traverse speeds. Square butt welding was successfully done at the

Table 21
FSW parameters and tool geometries for FSW of magnesium alloys and resultant grain sizes in stirred zone

Materials/plate thickness (mm)	Tool geometry	Tool rotation rate (rpm)	Tool traverse speed (mm/min)	Grain size in stirred zone (μm)	Reference
Cast AM50, AM60, AZ91/6	Plain threaded pin or MX Triflute TM	250–500	160–450	–	[202]
Wrought AZ31/6.4	Plain threaded pin or MX Triflute TM	250–500	160–450	–	[202]
Thixomolded AZ91D/2	Screw pin	880–1750	50–500	2–5	[203]
Wrought AZ31B-H24/4	Simple tool	1250–2500	87–507	~90	[204]
Cast AZ91D/4	–	1098–3600	32–187	7–19	[205]
Thixomolded AZ91D/2	–	800–2450	90–750	0.9–5.4	[206]
Wrought AZ31B/6.4	Screw pin	800–1000	60	25	[207]
Thixomolded AM60/2	Screw pin	2000	120	10–15	[208]
Cast AZ91D/5	–	–	55	–	[209]
Wrought AZ61/6.3	–	1220	90	<14	[210]

optimum parameter combinations of traverse speed of 50 mm/min and tool rotation rate of 1240–1750 rpm. Higher traverse speeds or lower rotation rates than the optimum parameters caused the formation of inner voids or a lack of bonding in the weld, which is due to the inherent poor formability of cast AZ91D magnesium alloy with a lot of intermetallic compounds, $\beta\text{-Al}_{12}\text{Mg}_{17}$ at grain boundaries. Similarly, Lee et al. [204] also reported that sound joints were produced only at higher tool rotation rates and lower traverse speeds in hot-rolled AZ31B-H24. On the other hand, the investigations by Lee et al. [205] and Park et al. [206] indicated that sound FSW welds of AZ91D can be produced at relatively high tool rotation rate of 800–1600 rpm for a wide range of tool traverse speed. For example, Park et al. [206] showed that at a tool rotation rate of 800 rpm, good weld was achieved in thixomolded AZ91D even for tool traverse speeds up to 750 mm/min. Furthermore, Lee et al. [205] and Park et al. [206] reported that very high tool rotation rate caused the formation of inner cavity and surface crack and the lack of bonding in both as-cast AZ91D and thixomolded AZ91D.

Second, FSW of magnesium alloy usually did not result in generation of liquid phase [201–208]. For example, Nagasawa et al. [210] reported a peak temperature up to 460 °C in the stirred zone of FSW AZ31. Similarly, based on microstructural features in the stirred zone, the peak temperature was estimated to be between 370 and 500 °C during FSW by Lee et al. [205] and Park et al. [206]. However, Kohn et al. [209] reported the occurrence of melting in FSW of cast AZ91D alloy and the generation of a complex microstructure in the weld. A melted and re-solidified region with a central heavily stirred zone and a thin melted layer at the top of the welded plates was observed. It is noted that Kohn et al. [209] did not report the tool rotation rate for FSW. Further, a relative low tool traverse speed of 55 mm/min was used. It is very likely that a high heat input resulted in generation of liquid phase.

Third, generally, as in FSW/FSP aluminum alloys, three microstructural zones are identified in FSW magnesium alloys, i.e., stirred zone (SZ), HAZ, and TMAZ [203,205,206]. The stirred zone with a basin or elliptical shape was characterized by fine recrystallized grains. However, Lee et al. [204] reported that the stirred zone can be divided into two subzones, SZ I and SZ II, in FSW hot-rolled AZ31B-H24. The SZ I, located at the center and upper side of the stirred zone, was characterized by partial dynamic recrystallization, and deformation layers were observed throughout the grains. In the SZ II, full dynamic recrystallization and grain growth had occurred, and no deformation structure such as twins and deformation layer was observed.

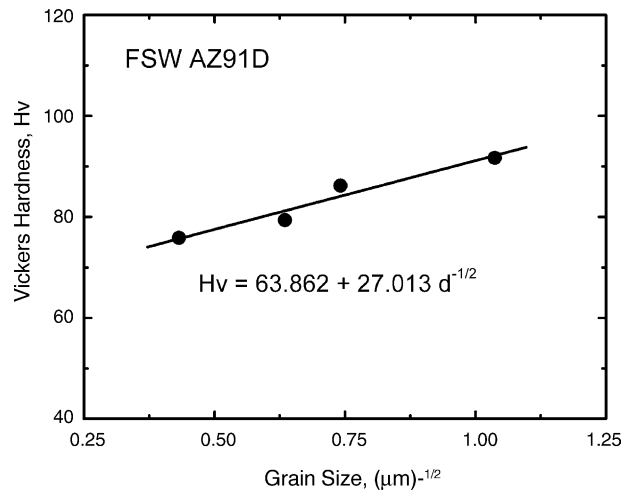


Fig. 37. Variation of hardness with grain size in friction stir welds of AZ91D (tool rotation rate: 1220 rpm, traverse speed: 90 mm/min) (after Park et al. [206]).

Fourth, generally, FSW resulted in generation of fine recrystallized grains in the stirred zone in magnesium alloys [203,205,206]. For as-cast magnesium alloy, the coarse α -Mg phase and β - $\text{Al}_{12}\text{Mg}_{17}$ intermetallic compound disappeared after FSW [203–205]. Further, Nakata et al. [203], Lee et al. [205], and Park et al. [206] reported that the grain size in the weld nugget became larger with increasing tool rotation rate and decreasing traverse speed due to increasing heat input, which promoted the growth of recrystallized grains. This observation is consistent with that in FSW aluminum alloys [10,15,63,67,90,91]. The coarse grains observed in some FSW magnesium alloys were attributed to significant grain growth during FSW thermal cycle due to high heat input [204,207].

Fifth, the hardness of the stirred zone is generally higher than that of the base materials due to refined grain structure in the stirred zone. Variation of hardness with grain size was identified to follow the Hall–Petch relationship (Fig. 37), i.e. hardness increases with decreasing grain size [205,206]. However, a reduction in hardness was revealed in the stirred zone of FSW hot-rolled AZ31B-H24 due to coarsening of grains [204].

Sixth, FSW resulted in an improvement in tensile properties of cast magnesium alloys such as AZ91 [203,205,206], whereas a reduction in tensile properties was observed in wrought magnesium alloys AZ31B-H24 and AZ61 [204,211]. Fig. 38 shows a comparison of tensile properties between the base metal, the weld joint for FSW thixomolded AZ91D in transverse direction, and the weld nugget in longitudinal direction (1220 rpm and 90 mm/min) [206]. In case of transverse test of the weld joint, all the test specimens fractured in the base metal [203,205,206]. This implies that the joint efficiency of these FSW joints was 100%. Longitudinal tensile tests indicated that the strengths and elongation of the weld nugget were significantly improved compared to those of the base metal [203,205,206]. Further, Park et al. [206] reported that at a constant tool rotation rate of 1251 rpm, the transverse strength of FSW cast AZ91D exhibited no dependence on the tool rotation rate, whereas the longitudinal strength increases with increasing tool rotation rate. On the other hand, Lee et al. [204] reported a reduction in tensile properties of FSW AZ31B-H24 with fracture occurring close to the stirred zone, which is attributed to significantly coarsened grain structure in the stirred zone. Similar results were also observed by Park et al. [211]. Transverse tensile test revealed that FSW AZ61 weld exhibited a much lower yield strength and elongation than the base metal. Further, ultimate tensile strength of the weld is slightly lower than that of the base metal. The weld fractured in the stirred zone near the transition region. Because there is no significant difference in both grain size and dislocation density

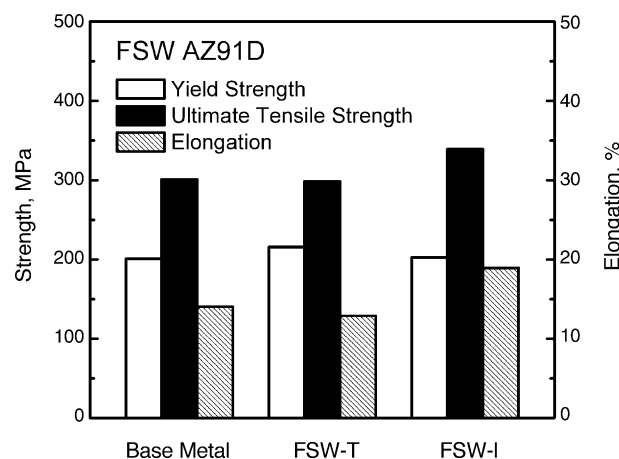


Fig. 38. Comparison of tensile properties of base metal, transverse weld, and weld nugget tested along longitudinal direction for AZ91D thixomolded sheet (tool rotation rate: 1220 rpm, traverse speed: 90 mm/min) (after Park et al. [206]).

between the stirred zone and the base metal, Park et al. [211,212] attributed the decrease in yield strength and ductility to heterogeneously distributed crystallographic microtextures with an accumulated (0 0 0 1) plane. In the fracture region, there is a strong tendency for the (0 0 0 1) basal plane to tilt to about 45° from the TD. This basal plane texture probably causes preferential plastic deformation in this region because the maximum resolved shear stress operates on (0 0 0 1) basal plane when these planes lie at 45° to the tensile direction.

6.5. Metal matrix composites

Metal matrix composites offer increased stiffness, strength and wear resistance over monolithic matrix materials. However, the weldability of these composites is significantly reduced due to the addition of ceramic reinforcements. Although low power tungsten-inert-gas (TIG) arc welding along with the concentration of heat on the unreinforced filler metal can produce sound welds, this technique relies heavily on operator skill and cannot avoid the matrix/reinforcement reaction completely. The drawbacks associated with the fusion welding include: (a) the incomplete mixing of the parent and filler materials, (b) the presence of porosity as big as $100\ \mu\text{m}$ in the fusion zone, (c) the excess eutectic formation, and (d) the formation of undesirable deleterious phases such as Al_4C_3 . Therefore, a solid-state welding technique is highly desirable for joining the metal matrix composites. Inertia or friction welding has been applied to particle reinforced aluminum matrix composites for the last 10 years. This technique relies on relative motion between the parts being joined to generate heat while pressure is applied. It is shown that conventional friction welding produces sound welds with good mechanical properties. However, it is limited to relatively simple geometries, typically rod or tube configurations. By comparison, friction stir welding shows potential for joining metal matrix composites due to its successful application in aluminum alloys.

Recently, several investigations were conducted on the feasibility of FSW of aluminum matrix composites such as 6092Al–SiC [213], 6061Al– B_4C [214], A339–SiC [215], 6061Al– Al_2O_3 [215–217], and 7093Al–SiC [218,219]. The processing parameters and tool materials for FSW of these composites together with the particle volume fraction (V_f) are summarized in Table 22. The following significant results emerged from this study. First, high-quality welds without visible defects could be generated by FSW in aluminum matrix composites reinforced with 10–30 vol.% ceramic particles. No

Table 22
FSW parameters and tool materials for FSW of aluminum matrix composites

Materials	Particle V_f (%)	Plate thickness (mm)	Tool rotation rate (rpm)	Tool traverse speed (mm/min)	Tool materials	References
6092-SiC	17		–	102	–	[213]
6061-B ₄ C	15–30		670	114–138	H13 tool steel (Rc > 52)	[214]
A339-SiC	10		650	60	20-Carbon steel	[215]
6061-Al ₂ O ₃	20		650	60	20-Carbon steel	[215,216]
6061-Al ₂ O ₃	10, 20	2, 4	500–3000	100–2500	–	[217]
7093-SiC	25		–	–	–	[218]
7093-SiC	25		–	150	–	[219]

evidence of any chemical reaction between reinforcements and matrix alloy was detected. However, compared to unreinforced aluminum alloys, the optimum FSW parameter for producing sound welds was limited to lower tool traverse speed [217]. Second, the ceramic particle distribution in the FSW welds was uniform (Fig. 39). However, while it was reported by several investigators [214–216,219] that the particles size distribution in the FSW composites was essentially identical to that in the base composites, other investigations [213,217,218] revealed significant breakdown of reinforcement particles in the weld nugget compared to the base composite. For example, Baxter and Reynolds [218] reported that the number of SiC particles in the FSW 7093Al–SiC composite is more than twice compared to the base composite, though basically same particle volume fractions were observed in both conditions. This indicated the occurrence of particle breakage during FSW. It was suggested that the particle damage occurred mainly by knocking of corners and sharp edges off large particles, rather than shattering of large particles [213,218]. Third, the composite welds made by friction stir welding exhibited improved mechanical properties over that made by the TIG. Table 23 summarizes the tensile properties of the base 6061Al–B₄C composite and the welds made by FSW and TIG. The tensile properties of the FSW composite are considerably superior to those of TIG composite. The yield strength of the FSW composite is even higher than that of the base material. This indicates that FSW is an effective welding technique for joining metal matrix composites.

A critical problem associated with FSW of the metal matrix composites is severe wear on the FSW tool due to the presence of hard ceramic reinforcements [213,214,216]. Nelson et al. [214] observed that for the threaded tool made from H13 tool steel, heat-treated to Rc > 52, on friction stir

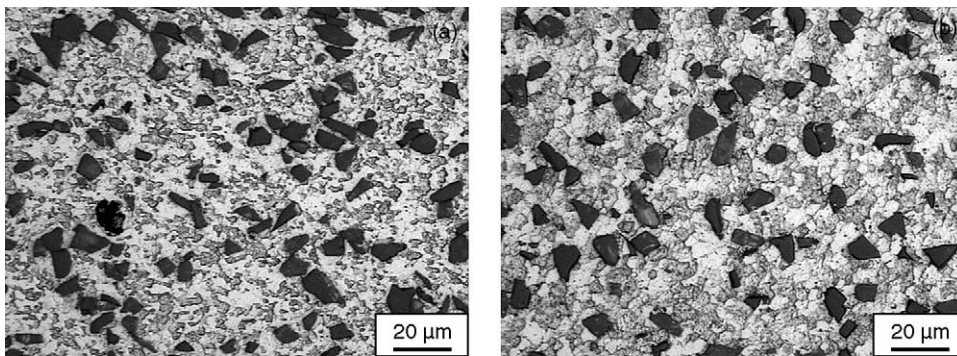


Fig. 39. Optical micrographs showing SiC particle distribution in (a) base metal and (b) the weld nugget in 7093Al–15 vol.% SiCp composite.

Table 23

Comparison between room-temperature tensile properties of FSW, TIG, and base 6061Al–B₄C composites (after Nelson et al. [214])

Materials	UTS (MPa)	YS (MPa)	Elongation (%)
Base material	248.0	124.0	12.0
FSW (114 mm/min traverse speed)	202.5	134.3	5.0
FSW (138 mm/min traverse speed)	209.4	136.4	4.0
TIG	157.7	119.9	4.0

welding of 6061Al–B₄C composite at a tool rotation rate of 670 rpm and a traverse speed of 114–138 mm/min, there are no threads left on the tool and approximately 2 mm was lost from the shoulder in less than 254 mm of weld. SEM backscattered images revealed that the wear debris from the tool was deposited through the thickness of the 6061Al–B₄C composite weld and on the surface of the weld in particular. It can be foreseen that the wear debris would affect the quality of the weld and reduce the properties. More recently, Prado et al. [216] investigated the tool wear behavior in friction stir welding of 6061Al–20% Al₂O₃ composite. For O1 tool-steel threaded pin heat-treated to an Rc hardness of 62, at a tool rotation rate of 500–2000 rpm and a traverse speed of 60 mm/min, while no apparent tool wear was noted for FSW of 6061Al, severe tool wear occurred for FSW of 6061Al–20% Al₂O₃ composite. The wear rate of the tool increases linearly with increasing linear welding distance. The largest wear rate was observed at a tool rotation rate of 1000 rpm. This means that the wear rate of tool did not increase when tool rotation rate was increased above 1000 rpm. A possible reason for this is the improvement of flow properties of the composite at high tool rotation rate because high tool rotation rate resulted in higher temperature as discussed in Section 3.2.

The wear of tool during FSW occurs at high temperature. Therefore, tools made from alloys with high-temperature wear resistance would reduce damage to the tool. Furthermore, the design of tool geometry is also important to reduce the tool wear. Active heating of composite workpiece before welding may also contribute to reducing tool wear due to improved flow properties of composites at high temperature.

6.6. Dissimilar alloys and metals

FSW is generally identified as a new welding technology that can be used to weld dissimilar alloys and metals. A few studies have been undertaken to friction stir weld dissimilar aluminum alloys, copper alloys or aluminum alloys to other metals [9,10,36–38,79,215,220–225]. Table 24 summarizes the materials and FSW parameters for FSW of dissimilar alloys/metals. However, most of these studies were previously focused on material flow visualization [10,36–38,79,215,220,221] and no optimum FSW parameters and tool geometry were identified in these systems. The resultant welds were usually with an unwelded seam, large open (void) zones, and oxide inclusions at the root of plates [10,36–38,79,215,220,221]. The weld efficiency was observed to reduce if a very hard aluminum alloy was stirred with a very soft aluminum alloy [79]. Furthermore, it was reported that the locations of two dissimilar alloys exerted a significant effect on material flow pattern and the resultant weld quality. For example, FSW of 5083Al to 6082Al and 6061Al to Cu showed that the low-strength material should be placed on the advancing side to produce better welds [220,222], whereas Lederich et al. [223] demonstrated that superior welds of 2024Al/D357 were obtained when high-strength 2024Al was placed on the advancing side of the weld. Although sound friction stir welds of 2024Al/D357 were produced, very little interpenetration between the advancing side 2024Al and retreating side D357,

Table 24
A summary of dissimilar alloys/metals FSW

Materials	Plate thickness (mm)	Rotation rate (rpm)	Traverse speed (mm/min)	References
2024Al to 6061Al	6.0	400–1200	60	[10,38,220]
6061Al to 2024Al	12.7	637	133	[36]
2024Al to 1100Al	0.65	650	60	[215]
5052Al to 2017Al	~5.3, 3	1000, 1250	60	[79,221]
7075Al to 2017Al	~5.3, 3	1000, 1250	60	[79,221]
7x1xAl (Sc) to 7x5xAl (Sc)	~5.3	1000	60	[221]
7075Al to 2017Al	3	1250	60	[79]
7075Al to 1100Al	3	1250	60	[79]
5083Al to 6082Al	5.0	–	170–500	[222]
2024Al to D357	–	–	–	[223]
6061Al to A356	4.0	1600	87–267	[225,226,228]
2024Al to 7075Al	25.4	150–200	76.2–127	[227]
20 vol.% Al ₂ O ₃ /6061Al to 10 vol.% SiC/A339	6.5	800	60	[215]
20 vol.% Al ₂ O ₃ /2014Al to 2024Al	4	1120	120	[224]
6061Al to copper	6.0	400–1200	60–180	[37,220]
2024Al to copper	6.5	650	60	[215]
2024Al to silver	6.0	650	60	[9]
Copper to brass	6.2	1000	60	[221]
1050Al to AZ31	6	2450	75	[229]
6061Al to AZ31B		800	75	[230]
6061Al to AZ91D		800	75	[230]
AZ91D to AM60B		2000	75	[230]
5083 Al to mild steel	2	100–1250	25	[231]
6061Al to AISI 1018	6	914	140	[232]

which is characteristic of a “cold weld” [223], was observed for the tool design and FSW parameters used in this study. In this case, friction stir weld of 2024Al/D357 exhibited reduced strength and poor ductility [223]. Wert [224] reported that in FSW of 2024Al to 20 vol.% Al₂O₃/2014Al, when harder composite was on the advancing side, the macrointerface span was larger. Furthermore, Wert [224] observed eutectic melting, which was attributed to unusually high tool rotation rate of 1120 rpm and higher flow stress of the composite. It is important to note that while a few studies have reported ‘localized’ or ‘incipient’ melting during FSW of aluminum alloys, the fundamentals of the process indicate that significant melting cannot be sustained. The tool transfers shear loads from pin surface to workpiece. As is well known, a liquid surface cannot support shear forces. The FSW process is therefore likely to be self-regulating in that if higher tool rotations lead to excessive heating, and the surface undergoes partial melting, the tool/workpiece coupling will drop limiting the temperature rise. Nevertheless, partial melting can occur, which is undesirable and sets the upper limit for the tool rotation rate. This is particularly critical for joining of dissimilar alloys or materials.

Two recent studies on friction stir welding of A356/6061Al and 2024Al/7075Al showed promise for joining dissimilar aluminum alloys via FSW [225–227]. Lee et al. [225,226] conducted friction stir welding of dissimilar A356 and 6061Al alloys at a tool rotation rate of 1600 rpm, traverse speeds of 87–267 mm/min, and a 3° tool tilt angle. They demonstrated defect-free friction stir welds of A356/6061Al. Microstructural examinations and property evaluations revealed following important observations. First, the microstructure of weld nugget was mainly governed by retreating side materials. When A356 was at the retreating side, the Si particles were dispersed over the weld center, whereas in case of 6061Al at the retreating side, the microstructure of 6061Al in the weld center showed fine and

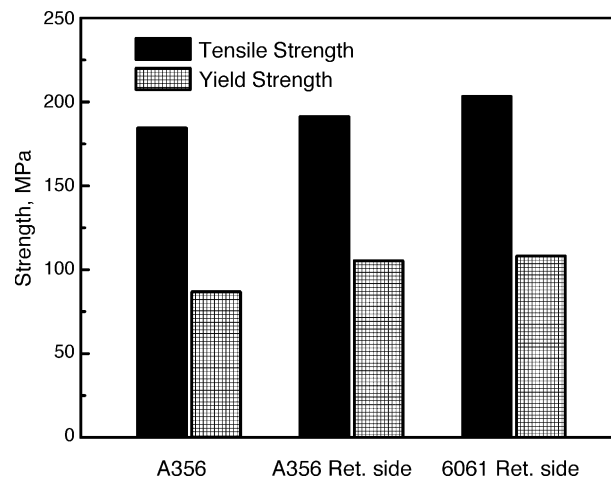


Fig. 40. Longitudinal tensile strength of A356/6061Al and A356 FSW joints (after Lee et al. [225]).

equiaxed recrystallized grains. Second, hardness of nugget zone was lower than that of 6061Al base metal due to the dissolution or coarsening of precipitates and it was higher than that of A356 base metal because of dispersion of Si particles. Third, the transverse strength of FSW joint was identical to that of A356 base metal and fracture occurred at the A356 base metal regardless of welding conditions. However, when strength of only nugget zone was tested by using the longitudinal tensile specimens, the strength of the weld zone of dissimilar A356/6061Al was consistently higher than that of FSWA356 (Fig. 40). Highest strength of weld nugget was obtained when 6061Al was fixed at the retreating side, though this strength was lower than that of 6061Al base metal due to the dissolution or coarsening of precipitates in the nugget zone. More recently, Baumann et al. [227] evaluated properties of 2024Al/7075Al bi-alloy friction stir weld. Defect-free 2024Al/7075Al FSW joints of 25.4 mm thick were successfully achieved at tool rotation rate of 150–200 rpm and traverse speed of 76.2–127 mm/min. The tensile properties of 2024Al/7075Al FSW joints and base materials are summarized in Table 25. The strength of 2024Al/7075Al FSW joints is 76–82% of 2024Al base material. Fracture always occurred in overaged HAZs. The reduced ductility in 2024Al/7075Al FSW joints was attributed to localized deformation in the low-strength HAZs. It is evident from Table 25 that the strength and ductility of 2024Al/7075Al FSW joints are comparable to those of 7050Al FSW joint. Additionally, tensile properties are consistent from the start to finish of the weld and also with depth in the weldments. Further, Baumann et al. [227] reported that the fatigue lifetimes ($K_t = 1.5$, $R = 0.06$) of 2024Al/7075Al FSW joints are comparable to the base materials.

Although previous investigations showed that FSW of dissimilar metals, such as aluminum to copper, did not result in generation of sound welds [37,215,220], some recent attempts have demonstrated a success in joining dissimilar metals using FSW, such as aluminum to steel and aluminum to magnesium [228–230]. For example, Kimapong and Watanabe [231] investigated the feasibility of joining 6061Al to mild steel via FSW, with aluminum plate on the retreating side and tool rotated clockwise. They reported that both tool rotation rate and pin position relative to butt line exerted a significant effect on the microstructure and tensile properties of the joints. Tool rotation rate of 250 rpm was identified as the optimal. Tool rotation rates below or above 250 rpm resulted in a considerable decrease in tensile strength. At the optimum tool rotation rate of 250 rpm, it was reported that pin position relative to butt line exerted a significant effect on weld quality. Unlike in FSW aluminum alloys, the position of pin axis on the butt line did not result in good weld quality for FSW of aluminum and steel. By moving the pin towards the aluminum side, the tensile strength of the welds

Table 25

Tensile properties of 2024Al/7075Al FSW joints (aged at 250 °F for 24 h prior testing) and base materials (after Baumann et al. [227])

Alloy	Rotation rate (rpm)	Traverse speed (mm/min)	Location of specimen	YS (MPa)	UTS (MPa)	Elongation (%)	Joint efficiency ^c (%)
2024Al-T351				348.9	488.2	17.5	
7075Al-T7351				422.0	509.5	10.8	
7050Al-T7451				470.2	533.7	13.5	
FSW 7050Al ^a	150	114.3	Start	265.5	388.2	5.6	72.7
			Finish	270.3	394.4	5.0	73.9
FSW 2024Al/7075Al ^a	150	114.3	Start	262.0	391.6	6.7	80.2
			Finish	257.9	388.9	6.7	79.7
FSW 2024Al/7075Al ^b	200	76.2	Start	246.2	371.6	5.7	76.1
			Finish	251.7	379.2	5.6	77.7
	200	101.6	Start	268.2	391.9	5.3	79.2
			Finish	262.7	391.2	5.9	79.1
	200	127	Start	278.7	397.8	5.8	81.5
			Finish	277.2	405.1	5.6	81.9

^a Produced by the Edison Welding Institute (EWI) in Columbus, OH, USA.

^b Produced by Boeing Phantom Works (HB) in Huntington Beach, CA, USA.

^c Joint efficiency for 2024Al/7075Al FSW joints was calculated relative to 2024Al-T351.

increased gradually. When 90% of the pin diameter was offset into the aluminum side, the weld exhibited maximum tensile strength of ~240 MPa, which was ~86% of the aluminum base metal tensile strength. When the pin was moved into the aluminum side completely, the tensile strength of the welds decreased substantially. Similarly, Chen and Kovacevic [232] showed that an offset of 68% of the pin diameter into the aluminum side led to a better weld quality. In such FSW aluminum/steel joints, steel fragments and intermetallics between iron and aluminum were identified [231,232]. Furthermore, the evidence of the melting of aluminum during FSW was revealed, which was attributed to higher thermal input [232]. Similarly, Sato et al. [229] reported constitutional liquation during FSW of aluminum to magnesium alloys.

7. Application highlights

7.1. Aerospace

It is well known that high-strength aluminum alloys such as 2XXX and 7XXX series are widely used for aerospace structures such as fuselage, fins, wings, etc. Unfortunately, such high-strength aluminum alloys are difficult to join by conventional fusion welding due to the occurrence of hot cracking during welding. Therefore, conventionally, a great amount of joining in the aerospace structures is achieved by means of riveting. This results in increased manufacturing complexity and cost. The emergence of friction stir welding provides an opportunity to alter traditional approach for producing lightweight assemblies for pervasive cost savings at the system level.

Eclipse Aviation is revolutionizing aircraft manufacturing by adopting FSW for joining skins components and structure in Eclipse 500 aircraft. Other remarkable successes include adoption of

FSW by Boeing for its Delta rocket tanks and C17 internal structures. The combined efforts of aerospace industries have produced miles of FSW welds in commercial set-up without defects.

7.2. Armor

High-strength aluminum alloys have been used as armor due to a combination of high ballistic performance and static strength. For example, in the UK, an armor aluminum alloy Def Stan 95-22 Class 1, based on the 7017 Al–4.5Zn–2Mg alloy composition, has been used by the Ministry of Defense since the early 1970s. Such an armor alloy was conventionally welded by MIG using Al–Mg filler. However, the major problems associated with the MIG welds are: (a) stress corrosion initiating at the weld toe, (b) exfoliation occurring in the solution treated and naturally aged part of the HAZ, and (c) liquation due to the formation of low melting point grain boundary films. With the emergence of new solid-state FSW process, a defense research agency in the UK started a program to evaluate FSW for aluminum armor in 1995. Preliminary investigations on exfoliation corrosion and stress corrosion cracking tests verified the advantages of FSW over MIG in terms of weld quality [233]. Further research is focused on the development of real joint designs for property verification and the application of techniques to increase the speed of welding and the thickness of plate that can be joined [233].

In the US, armor aluminum alloy 2519-T87 is being used as the main structural alloy in the Advanced Amphibious Assault Vehicle (AAAV) because it offers higher ballistic protection and static strength than the mainstay aluminum armor alloy, 5083Al-H131. AAAV is an armored personnel carrier under development for the U.S. Marine Corps. The welded aluminum structure allows the AAAV to carry up to 18 fully outfitted combatants, at high speed, over land or sea to their destinations. Currently, gas metal arc welding (GMAW) and gas tungsten arc welding (GTAW) are the primary processes for building the hull structure of the AAAV. However, GMAW and GTAW produce low ductility in butt welds in 2519Al alloy, with the result that the welds do not pass the ballistic shock test required for combat vehicle applications. This prevents many simple butt weld designs from being used in the vehicle structure. Although other joint types in areas where plates must be joined have been resorted, this results in greater complexity and concomitant higher manufacturing costs. FSW, being a solid-state process, has been shown to produce superior as-welded mechanical properties when compared to typical arc welding processes in other aluminum alloys such as 5083Al, 6061Al, and 2219Al. Therefore, in the past few years, attempts were made in General Dynamics Land Systems (GDLS) [234] and Concurrent Technologies Corporation (CTC) [235] to friction stir weld 2519Al-T87. It was shown that sound-quality one inch thick flat-butt weld and 1–2-in. thick 90° corner welds can be successfully made by friction stir welding [235]. FSW 2519Al-T87 exhibited an ultimate tensile strength of 389 MPa while maintaining a ductility of nearly 14%, representing an increase of 124 MPa in tensile strength and 300% increase in ductility over GMAW minimum properties. Further, Colligan et al. [235] demonstrated that both flat and 90° corner weld panels passed the ballistic shock test with less than 12 in. of cracking, even though the impacting velocities were about 30% over the specification requirement. Currently, mine-blast testing of FSW article is under progress to further evaluate the suitability of FSW for joining armor aluminum alloys.

8. Development of friction stir processing

Friction stir welding has a number of attributes that can be used to develop a generic tool for microstructural modification and manufacturing. Friction stir processing was developed based on

basic concept of FSW [13,14]. This has led to several applications for microstructural modification in metallic materials, including superplasticity [13–15,85–88,100,236,237], surface composite [14,238], homogenization of nanophase aluminum alloys and metal matrix composites [239,240], and microstructural refinement of cast aluminum alloys [19,43,241].

8.1. Superplasticity

It is well known that two basic requirements are necessary for achieving structural superplasticity. The first is a fine grain size, typically less than 15 μm . The second is thermal stability of the fine microstructure at high temperatures. Conventionally, thermo-mechanical processing (TMP) is used to produce fine-grained microstructure in commercial aluminum alloys [242–244]. A typical TMP for heat-treatable aluminum alloys consists of solution treatment, overaging, multiple pass warm rolling (200–220 $^{\circ}\text{C}$) with intermittent re-heating, and a recrystallization treatment [244]. Clearly, TMP is complex and time-consuming and results in increased material cost. More importantly, the optimum superplastic strain rate of 1×10^{-4} to $10 \times 10^{-3} \text{ s}^{-1}$ obtained in TMP commercial aluminum alloys such as 7075 and 7475 [242–244] is too slow for superplastic forging/forming of components in the automotive industry. To advance superplastic forming (SPF) into mass production oriented industries, there is a need to develop new processing techniques and/or aluminum alloys to shift the optimum superplastic strain rate to high-strain rate ($>10^{-2} \text{ s}^{-1}$).

As presented in Section 4.1.2, FSW/FSP results in generation of fine microstructure of 0.1–18 μm in various aluminum alloys [4–7,15,63,75–91,95,96,98]. The grain size range in the FSW/FSP aluminum alloys is within the grain size range required for attaining structural superplasticity. Therefore, it is expected that the fine-grained aluminum alloys prepared by FSP would exhibit superplastic behavior. Mishra et al. [13] were the first to investigate the superplastic behavior of FSP 7075Al alloy. They observed that FSP 7075Al alloy with a grain size of $\sim 3.3 \mu\text{m}$ exhibited high-strain rate superplasticity. A maximum elongation of above 1000% was obtained at a strain rate of $1 \times 10^{-2} \text{ s}^{-1}$ and 490 $^{\circ}\text{C}$.

Recently, Ma et al. [15,85,236], Mahoney et al. [100], Charit et al. [86,88,237] further examined the effect of FSP on superplastic deformation behavior of a few aluminum alloys. The grain size produced by FSP along with optimum strain rate and temperature for superplastic deformation are summarized in Table 26. These investigations reveal following observations. First, high-strain rate superplasticity (HSRS) was observed in several aluminum alloys. For example, a superplastic elongation of 1280% was obtained in FSP Al–4Mg–1Zr alloy at a high-strain rate of $1 \times 10^{-1} \text{ s}^{-1}$ and a temperature of 525 $^{\circ}\text{C}$ [85]. This demonstrated the effectiveness of FSP for processing fine-grained materials that are amenable to HSRS. Second, the microstructural refinement in FSP aluminum alloys can be controlled by adjusting

Table 26
Maximum superplastic ductility obtained in FSP aluminum alloys

Alloy	As-received condition	Grain size (μm)	Temperature ($^{\circ}\text{C}$)	Strain rate (s^{-1})	Elongation (%)	Reference
7075Al	As-rolled	3.8	480	3×10^{-3}	1440	[15]
7075Al	As-rolled	7.5	500	3×10^{-3}	1040	[15]
7050Al	As-rolled	4.2	450	2×10^{-4}	550	[100]
2024Al	As-rolled	2.0	430	1×10^{-2}	525	[86]
5083Al	As-rolled	6.0	530	3×10^{-3}	590	[88]
Al–4Mg–1Zr	As-extruded	1.5	525	1×10^{-1}	1280	[85]
A356	As-cast	~ 3.0	530	1×10^{-3}	650	[236]
Al–Zn–Mg–Sc	As-cast	1.8	510	3×10^{-2}	1800	[237]

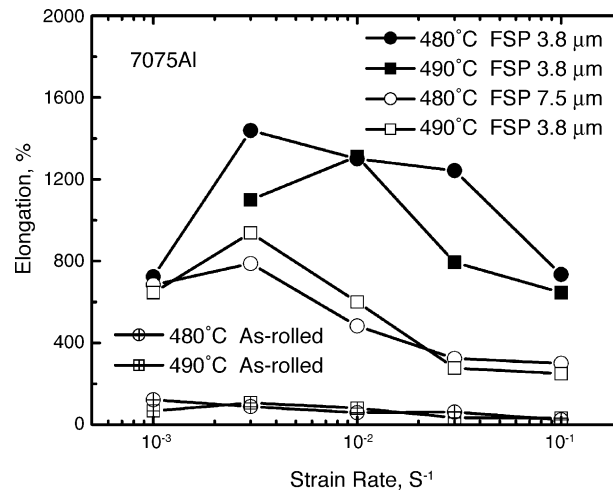


Fig. 41. Variation of elongation with initial strain rate for as-rolled and FSP 7075Al alloys [15].

FSP parameter, resulting in significantly enhanced superplasticity and decreased flow stress, and a shift to higher optimum strain rates and lower temperature. Fig. 41 shows the effect of grain size on the superplasticity of FSP 7075Al alloys as a function of initial strain rate. Third, one-step FSP can induce superplasticity in as-cast aluminum alloys. For example, 650% of superplasticity was obtained in as-cast A356 via FSP [236]. This is the first time to achieve superplasticity in A356. Fourth, enhanced superplastic deformation kinetics was observed in several FSP aluminum alloys. For example, the superplastic behavior of FSP 7075Al and Al–4Mg–1Zr can be described by a unified equation (Fig. 42):

$$\dot{\varepsilon} = 700 \frac{D_0 E b}{kT} \exp\left(\frac{-84000}{RT}\right) \left(\frac{b}{d}\right)^2 \left(\frac{\sigma - \sigma_0}{E}\right)^2, \quad (7)$$

where $\dot{\varepsilon}$ is the strain rate, D_0 the pre-exponential constant for diffusivity, E the Young's modulus, b the Burger's vector, k the Boltzmann's constant, T the absolute temperature, R the gas constant, d the grain size, σ the applied stress, and σ_0 is the threshold stress. The constitutive relationship for superplasticity in fine-grained aluminum alloys can be expressed as [245]:

$$\dot{\varepsilon} = 40 \frac{D_0 E b}{kT} \exp\left(\frac{-84000}{RT}\right) \left(\frac{b}{d}\right)^2 \left(\frac{\sigma - \sigma_0}{E}\right)^2. \quad (8)$$

Clearly, the dimensionless constant in Eq. (8) is more than one order of magnitude larger than that in Eq. (7). Ma et al. [15,246] attributed the enhanced deformation kinetics in the FSP aluminum alloys to the high percent of high-angle boundaries produced by friction stir processing [14].

Salem et al. [80] investigated the effect of FSW on the microstructure and superplasticity of a superplastic 2095 sheet. It was reported that the dynamically recrystallized 2095 SP sheets were successfully friction stir welded at 1000 rpm and welding speed of 3.2 and 4.2 mm/s, with fine-grained microstructure formed in the weld nugget. Superplasticity was retained after FSW and increased with increasing welding speed. This demonstrates that FSW is an effective technique to join superplastic alloy plates/sheets while retaining superplasticity. By comparison, conventional fusion welding techniques would destroy the desired microstructure in the welded region and the superplastic flow behavior would be lost after fusion welding. Joining superplastic alloy plates/sheets prior to forming would provide design flexibility for integrally stiffened structures.

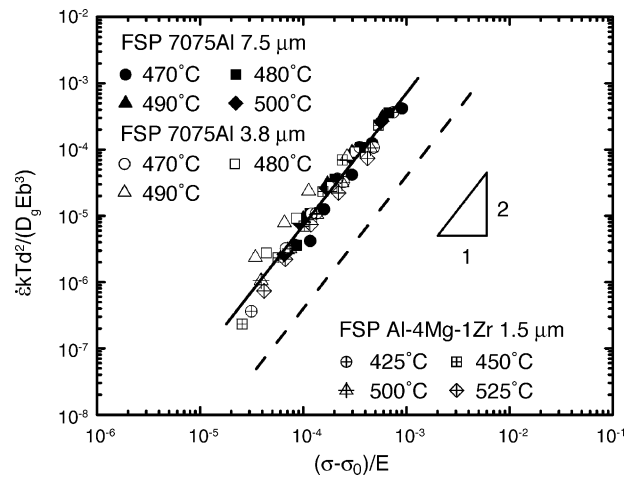


Fig. 42. Variation of $(\epsilon k T d^2 / D_g E b^3)$ with normalized effective stress for FSP 7075Al alloys (dashed line represents Eq. (8)) [15].

It should be pointed out that the basic requirement of fine grain size is a necessary but not always sufficient condition to obtain superplasticity. If the fine grain microstructure is not stable at high temperature, superplastic elongation will be significantly reduced. A recent investigation showed that FSP 7475Al exhibited no superplastic elongation due to abnormal grain growth at high temperatures, though this alloy had a very fine original grain size of 2–3 μm [87]. Similarly, abnormal grain growth was also observed at high temperature in FSP 7050 and 2519 aluminum alloys [247]. The thermal stability in FSP 7075Al alloy and Al–4Mg–1Zr alloy was attributed to the effective pinning of grain growth by fine Cr-bearing dispersoids and MgZn_2 -type precipitates, and Al_3Zr dispersoids, respectively. Therefore, it is important to understand the effect of alloy chemistry, FSP parameters on the thermal stability of fine microstructure of FSP aluminum alloys.

8.2. Surface composites

Compared to unreinforced metals, metal matrix composites reinforced with ceramic phases exhibit high strength, high elastic modulus, improved resistance to wear, creep and fatigue, which make them promising structural materials for aerospace and automobile industries. However, these composites also suffer from a great loss in ductility and toughness due to incorporation of non-deformable ceramic reinforcements, which limits their applications to a certain extent. For many applications, the useful life of components often depends on their surface properties such as wear resistance. In these situations, it is desirable that only the surface layer of components is reinforced by ceramic phases while the bulk of components retain the original composition and structure with higher toughness.

In recent years, several surface modification techniques, such as high-energy laser melt treatment [248–255], high-energy electron beam irradiation [256,257], plasma spraying [258], cast sinter [259,260], and casting [261], have been developed to fabricate surface metal matrix composites. Among these techniques, laser melt treatment (also called laser processing or laser surface engineering (LSE)) is widely used for surface modification. However, it should be pointed out that the existing processing techniques for forming surface composites are generally based on liquid phase processing at high temperatures. In this case, it is hard to avoid the interfacial reaction between reinforcement and

Table 27

Effect of processing parameters on formation of 5083Al–SiC surface composite (300 rpm tool rotation rate and 1.0 mm pin height) [16]

Target depth (mm)	Tool traverse speed (mm/min)	
	25.4	101.6
1.78	No particles was incorporated into aluminum	–
2.03	Surface composite was formed with well-distributed particles and very good bonding with metal substrate	Surface composite has poor bonding with metal substrate
2.28	No particles was incorporated into aluminum	–

metal matrix and formation of some detrimental phases. Furthermore, critical control of processing parameters is necessary to obtain ideal solidified microstructure in surface layer. Obviously, if processing of surface composite is carried out at temperatures below melting point of substrate, the problems mentioned above can be avoided.

Recently, studies were conducted by Mishra et al. [16,238] to incorporate ceramic particles into surface layer of aluminum alloy (5083Al and A356) to form surface composite by means of FSP. They reported that the processing parameters (tool geometry, tool rotation rate, traverse speed, and target depth) exhibit significant effects on formation of surface composite layer. Table 27 summarizes the effects of tool traverse speed and target depth on the formation of surface composite layer when processing was conducted using a tacking tool of 1.0 mm pin height at a constant tool rotation rate of 300 rpm. Table 27 shows that at a constant of tool traverse speed of 25.4 mm/min, when the target depth is too large (2.28 mm), the shoulder of tool pushed away all the preplaced SiC particles, and, basically no surface composite formed. Too small target depth (1.78 mm) was also ineffective to mix SiC particles into aluminum alloy. A target depth of 2.03 mm resulted in incorporation of SiC particles into aluminum matrix (Fig. 43a). However the bonding of surface composite layer and substrate plate was influenced by the traverse speed. At higher traverse speed (101.6 mm/min), the surface composite layer was usually separated from the aluminum alloy substrate and the bonding was poor as shown in Fig. 43b.

Table 28 summarizes the microhardness of Al–SiC surface composites with different volume fraction of SiC particles and aluminum substrate. Table 28 reveals that the incorporation of SiC particles into surface layer of aluminum alloy can increase significantly the hardness of aluminum substrates.

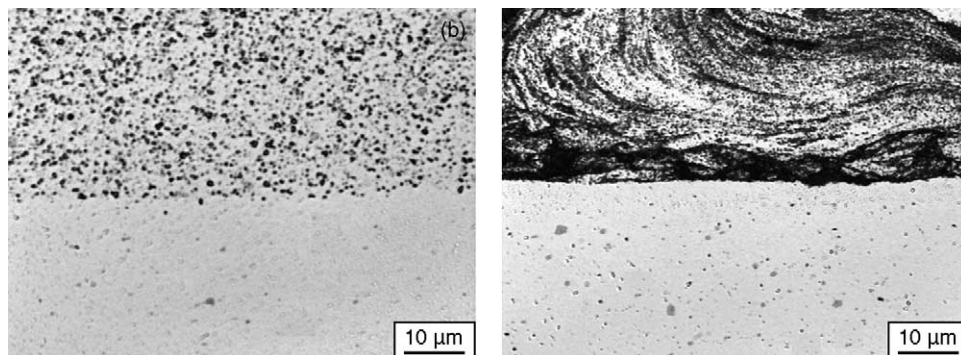


Fig. 43. Optical micrograph showing surface composites on 5083Al substrate produced at a tool rotation rate of 300 rpm and a traverse speed of: (a) 25.4 mm/min and (b) 101.6 mm/min [16].

Table 28
Microhardness of Al–SiC surface composites and aluminum substrates [238]

Location	Volume % of SiC particles	Hardness (HV)
A356 substrate	0	88 (region without Si particles), 108 (region with coarse Si particles)
A356 surface composite	15 ± 2	171
5083 substrate plate	0	85
5083 surface composite	5 ± 1	110
	13 ± 2	123
	27 ± 3	173

8.3. Microstructural modification

Al–7 wt.% Si–Mg alloys are widely used to cast high-strength components in the aerospace and automobile industries because they offer a combination of high strength [262–264] with good casting characteristics [265]. However, some mechanical properties of cast alloys, in particular ductility, toughness and fatigue resistance, are limited by porosity, coarse acicular Si particles, and coarse primary aluminum dendrites [266–269].

Various modification and heat-treatment techniques have been developed to refine the microstructure of cast Al–Si–Mg alloys. The first category of research is aimed at modifying the morphology of Si particles. For example, eutectic modifiers such as sodium, strontium, and antimony are widely used to spheroidize Si particles [270,271]. However, there are some drawbacks with these modifiers. For sodium, the benefits fade rapidly on holding at high temperature and the modifying action practically disappears after only two remelts. For strontium, the density of microshrinkage porosity is increased after the addition of strontium due to owing to increased gas pickup from the dissolution difficulty [272] and a depression in the eutectic transformation temperature [273]. For antimony, environmental and safety concerns have precluded its use in most countries. Alternatively, heat treatment of cast alloys at high temperature, usually at the solid solution temperature around 540 °C for long time, is also used to modify the morphologies of Si particles [269]. Solution heat-treatment results in a substantial degree of spheroidization of Si particles and also coarsens Si particles. However, solution treatment at high temperature for long time increases material cost. The second research category refines the coarse primary aluminum phases. Heat treatment at an extremely high temperature of 577 °C for a short time of 8 min resulted in a substantial refinement in the aluminum dendrites in a semi-solid processed (SSP) A356 [264]. Furthermore, it was reported that a melt thermal treatment led to a remarkable refinement of the aluminum phase in A356, thereby resulting in a significant improvement in both strength and ductility [274].

It is important to point out that none of the modification and heat-treatment techniques mentioned above can eliminate the porosity effectively in Al–Si–Mg castings and redistribute the Si particles uniformly into the aluminum matrix. As presented above, during FSP, tool transports materials from the front to the back of the tool in a complex way, resulting in intense deformation and mixing of material. It is expected that such a process can refine effectively the microstructure of Al–Si–Mg castings.

Recently, Ma et al. [19,43] investigated the effect of FSP on microstructure and properties of A356. Typical microstructure of A356 before and after FSP is shown in Fig. 9. Table 29 summarizes the size and aspect ratio of Si particles and porosity level in both as-cast and FSP A356 alloys. FSP

Table 29

Size and aspect ratio of Si particles and porosity volume fraction in FSP and as-cast A356 (tri-flute pin, tool rotation rate of 700 rpm and traverse speed of 203 mm/min) [43]

Material	Particle size (μm)	Aspect ratio	Porosity volume fraction (%)
As-cast	16.75 ± 9.21	5.92 ± 4.34	0.95
FSP	2.50 ± 2.02	1.94 ± 0.88	0.024

Table 30

Room-temperature tensile properties of as-cast and FSP A356 (tri-flute pin, tool rotation rate of 700 rpm and traverse speed of 203 mm/min) [43]

Materials	As-cast or as-FSP			Aged (155 °C/4 h)			T6 (540 °C/4 h + 155 °C/4 h)		
	UTS (MPa)	YS (MPa)	Elongation (%)	UTS (MPa)	YS (MPa)	Elongation (%)	UTS (MPa)	YS (MPa)	Elongation (%)
As-cast	169 ± 8	132 ± 3	3 ± 1	153 ± 6	138 ± 4	2 ± 1	220 ± 10	210 ± 8	2 ± 1
FSP	251 ± 4	171 ± 12	31 ± 1	281 ± 4	209 ± 2	26 ± 2	301 ± 6	216 ± 11	28 ± 2

resulted in a significant breakup of coarse acicular Si particles and primary aluminum dendrites, created a homogeneous distribution of Si particles in the aluminum matrix, and nearly eliminated all casting porosity. These microstructural modifications significantly improved the mechanical properties of cast A356, in particular ductility and fatigue lifetime. Table 30 summarizes the room-temperature tensile properties of FSP and as-cast A356 samples. FSP resulted in a significant improvement in tensile properties, particularly in the ductility. The elongation-to-failure was increased by one order of magnitude after FSP. Furthermore, FSP results in an improvement in fatigue threshold stress by >80% as shown by Fig. 44. The significant improvement in mechanical properties of FSP A356 is attributed to microstructural refinement (both aluminum matrix and Si particles) and homogenization and elimination of porosity [19,43,241].

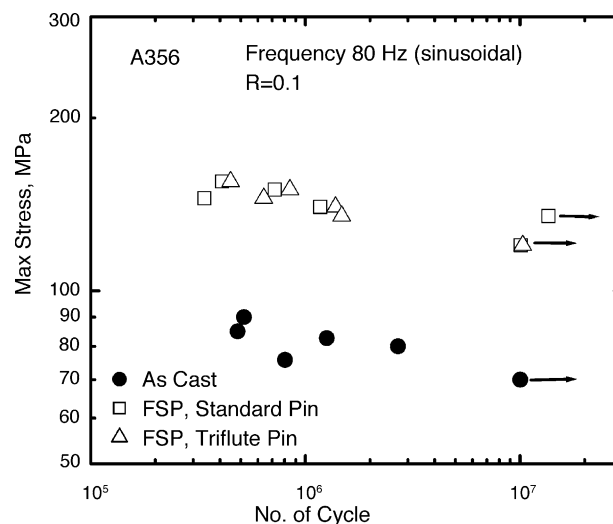


Fig. 44. Influence of FSP on fatigue properties of A356 [241].

9. Critical research issues

9.1. Material flow

As discussed in Section 3.1, material flow process during FSW is quite complicated and poorly understood. Clearly, complete understanding of material transport around rotating tool is crucial to the optimization of FSW parameters and design of tool geometry. The optimization of FSW parameters and geometry will be beneficial to the increase in weld quality and productivity. New experimental techniques, theoretical and computational models are needed to understand the material flow pattern during FSW.

9.2. Tool material and shape

Wear of tool is generally not considered as a severe issue in friction stir welding of aluminum alloys [216,275]. For friction stir welding of high melting point materials (steel and titanium) and wearable materials (metal matrix composites), tool wear has been identified as a serious problem [190,191,216]. However, very limited studies on the tool wear during FSW have been reported. Most of tool designs are based on intuitive concepts. Integration of computational tools is important for visualization and optimization. Furthermore, as for selection of tool material, although it is considered to be important for friction stir welding of steel, titanium, and composites, no systematical studies have been reported so far. It is very likely that tool wear and shape optimization are associated with the tool materials. Clearly, further research is needed to understand the tool wear, optimization of tool geometry and selection of tool material.

9.3. Microstructural stability

Normally the friction stir welds are used in the as-welded condition or with stabilization aging when base material is in the hardened conditions (T6 and T4 tempers). However, when welding is conducted with the base material in soft condition, there are some advantages. For example, it was found that the welding force is lower if the base material was in soft “O” (annealing) condition compared to T6 condition [276]. Furthermore, if the welding is conducted under O condition, the forming operation after FSW can be much more easily performed. In the case of the FSW under O condition, it is necessary to conduct post weld heat treatment (PWHT) to strengthen the component. Therefore, it is important to understand the effect of PWHT on the microstructure and properties of FSW joints. A few studies reported so far indicate that PWHT (solution treatment + aging) results in abnormal grain growth, thereby leading to the reduced properties of welds [83,277,278].

A recent investigation showed that the processing parameters exert significant effect on the stability of grain structure in the nugget zone of FSP 7075Al [279]. In an optimum processing window, combination of tool rotation rate and traverse speed [279], no abnormal grain growth is observed. Therefore, it is important to understand the effect of alloy chemistry, FSW/FSP parameters on the thermal stability of fine-grained microstructure of FSW/P aluminum alloys.

10. Summary and future outlook

In this review article current developments in process modeling, microstructure and properties, material specific issues, applications of friction stir welding/processing have been addressed.

Tool geometry is very important factor for producing sound welds. However, at the present stage, tool designs are generally proprietary to individual researchers and only limited information is available in open literature. From the open literature, it is known that a cylindrical threaded pin and concave shoulder are widely used welding tool features. Besides, tri-fluted pins such as MX Trifute™ and Flared-Trifute™ have also been developed.

Welding parameters, including tool rotation rate, traverse speed, spindle tilt angle, and target depth, are crucial to produce sound and defect-free weld.

As in traditional fusion welding, butt and lap joint designs are the most common joint configurations in friction stir welding. However, no special preparation is needed for the butt and lap joints of friction stir welding. Two clean metal plates can be easily joined together in the form of butt or lap joints without concern about the surface conditions of the plates.

It is widely accepted that material flow within the weld during FSW is very complex and still poorly understood. It has been suggested by some researchers that FSW can be generally described as an in situ extrusion process and the stirring and mixing of material occurred only at the surface layer of the weld adjacent to the rotating shoulder.

FSW results in significant temperature rise within and around the weld. A temperature rise of 400–500 °C has been recorded within the weld for aluminum alloys. Intense plastic deformation and temperature rise result in significant microstructural evolution within the weld, i.e., fine recrystallized grains of 0.1–18 μm, texture, precipitate dissolution and coarsening, and residual stress with a magnitude much lower than that in traditional fusion welding.

Three different microstructural zones have been identified in friction stir weld, i.e., nugget region experiencing intense plastic deformation and high-temperature exposure and characterized by fine and equiaxed recrystallized grains, thermo-mechanically affected region experiencing medium temperature and deformation and characterized by deformed and un-recrystallized grains, and heat-affected region experiencing only temperature and characterized by precipitate coarsening.

Compared to the traditional fusion welding, friction stir welding exhibits a considerable improvement in strength, ductility, fatigue and fracture toughness. Moreover, 80% of yield stress of the base material has been achieved in friction stir welded aluminum alloys with failure usually occurring within the heat-affected region, whereas overmatch has been observed for friction stir welded steel with failure location in the base material. Fatigue life of friction stir welds are lower than that of the base material, but substantially higher than that of laser welds and MIG welds. After removing all the profile irregularities from the weld surfaces, fatigue strengths of FSW specimens were improved to levels comparable to that of the base material. The fracture toughness of friction stir welds is observed to be higher than or equivalent to that of base material. As for corrosion properties of friction stir welds, contradicting observations have been reported. While some studies showed that the pitting and SCC resistances of FSW welds were superior or comparable those of the base material, other reports indicate that FSW welds of some high-strength aluminum alloys were more susceptible to intergranular attack than the base alloys with preferential occurrence of intergranular attack in the HAZ adjacent to the TMAZ.

In addition to aluminum alloys, friction stir welding has been successfully used to join other metallic materials, such as copper, titanium, steel, magnesium, and composites. Because of high melting point and/or low ductility, successful joining of high melting temperature materials by means of FSW was usually limited to a narrow range of FSW parameters. Preheating is beneficial for improving the weld quality as well as increase in the traverse rate for high melting materials such as steel.

Based on the basic principles of FSW, a new generic processing technique for microstructural modification, friction stir processing (FSP) has been developed. FSP has found several applications for microstructural modification in metallic materials, including microstructural refinement for high-

strain rate superplasticity, fabrication of surface composite on aluminum substrates, and homogenization of microstructure in nanophase aluminum alloys, metal matrix composites, and cast Al–Si alloys.

Despite considerable interests in the FSW technology in past decade, the basic physical understanding of the process is lacking. Some important aspects, including material flow, tool geometry design, wear of welding tool, microstructural stability, welding of dissimilar alloys and metals, require understanding. However, as pointed out by Prof. Thomas W. Eagar of Massachusetts Institute of Technology, “New welding technology is often commercialized before a fundamental science emphasizing the underlying physics and chemistry can be developed”. This is quite true with the FSW technology. Although it is only 14 years since FSW technology was invented at The Welding Institute (Cambridge, UK) in 1991, quite a few successful industrial applications of FSW have been demonstrated.

Acknowledgements

The authors gratefully acknowledge the support of: (a) the National Science Foundation through grant DMR-0076433 and the Missouri Research Board for the acquisition of a friction stir welding and processing machine, (b) the National Science Foundation through grants DMI-0085044 and DMI-0323725, Dr. Jian Cao, Program Manager, and (c) the DARPA under contract No. MDA972-02-C-0030; Dr. Leo Christodoulou, program manager.

References

- [1] W.M. Thomas, E.D. Nicholas, J.C. Needham, M.G. Murch, P. Templesmith, C.J. Dawes, G.B. Patent Application No. 9125978.8 (December 1991).
- [2] C. Dawes, W. Thomas, TWI Bulletin 6, November/December 1995, p. 124.
- [3] B. London, M. Mahoney, B. Bingel, M. Calabrese, D. Waldron, in: Proceedings of the Third International Symposium on Friction Stir Welding, Kobe, Japan, 27–28 September, 2001.
- [4] C.G. Rhodes, M.W. Mahoney, W.H. Bingel, R.A. Spurling, C.C. Bampton, *Scripta Mater.* 36 (1997) 69.
- [5] G. Liu, L.E. Murr, C.S. Niou, J.C. McClure, F.R. Vega, *Scripta Mater.* 37 (1997) 355.
- [6] K.V. Jata, S.L. Semiatin, *Scripta Mater.* 43 (2000) 743.
- [7] S. Benavides, Y. Li, L.E. Murr, D. Brown, J.C. McClure, *Scripta Mater.* 41 (1999) 809.
- [8] L.E. Murr, Y. Li, R.D. Flores, E.A. Trillo, *Mater. Res. Innovat.* 2 (1998) 150.
- [9] Y. Li, E.A. Trillo, L.E. Murr, *J. Mater. Sci. Lett.* 19 (2000) 1047.
- [10] Y. Li, L.E. Murr, J.C. McClure, *Mater. Sci. Eng. A* 271 (1999) 213.
- [11] H.B. Cary, *Modern Welding Technology*, Prentice-Hall, New Jersey, 2002.
- [12] C.J. Dawes, W.M. Thomas, *Weld. J.* 75 (1996) 41.
- [13] R.S. Mishra, M.W. Mahoney, S.X. McFadden, N.A. Mara, A.K. Mukherjee, *Scripta Mater.* 42 (2000) 163.
- [14] R.S. Mishra, M.W. Mahoney, *Mater. Sci. Forum* 357–359 (2001) 507.
- [15] Z.Y. Ma, R.S. Mishra, M.W. Mahoney, *Acta Mater.* 50 (2002) 4419.
- [16] R.S. Mishra, Z.Y. Ma, I. Charit, *Mater. Sci. Eng. A* 341 (2002) 307.
- [17] P.B. Berbon, W.H. Bingel, R.S. Mishra, C.C. Bampton, M.W. Mahoney, *Scripta Mater.* 44 (2001) 61.
- [18] J.E. Spowart, Z.Y. Ma, R.S. Mishra, in: K.V. Jata, M.W. Mahoney, R.S. Mishra, S.L. Semiatin, T. Lienert (Eds.), *Friction Stir Welding and Processing II*, TMS, 2003, pp. 243–252.
- [19] Z.Y. Ma, S.R. Sharma, R.S. Mishra, M.W. Mahoney, *Mater. Sci. Forum* 426–432 (2003) 2891.
- [20] M.R. Johnsen, *Weld. J.* 78 (2) (1999) 35.
- [21] E.D. Nicholas, W.M. Thomas, *Int. J. Mater. Prod. Technol.* 13 (1998) 45.
- [22] S.W. Kallee, J. Davenport, E.D. Nicholas, *Weld. J.* 81 (10) (2002) 47.
- [23] S. Kallee, A. Mistry, in: Proceedings of the First International Symposium on Friction Stir Welding, Thousand Oaks, CA, USA, June 14–16, 1999.

- [24] W.M. Thomas, E.D. Nicholas, S.D. Smith, in: S.K. Das, J.G. Kaufman, T.J. Lienert (Eds.), *Aluminum 2001—Proceedings of the TMS 2001 Aluminum Automotive and Joining Sessions*, TMS, 2001, p. 213.
- [25] W.M. Thomas, K.I. Johnson, C.S. Wiesner, *Adv. Eng. Mater.* 5 (2003) 485.
- [26] W.M. Thomas, A.B.M. Braithwaite, R. John, in: *Proceedings of the Third International Symposium on Friction Stir Welding*, Kobe, Japan, September 27–28, 2001.
- [27] W.M. Thomas, R.E. Dolby, in: S.A. David, T. DebRoy, J.C. Lippold, H.B. Smartt, J.M. Vitek (Eds.), *Proceedings of the Sixth International Conference on Trends in Welding Research*, Pine Mountain, GA, ASM International, 2003, pp. 203–211.
- [28] A.P. Reynolds, T.U. Seidel, M. Simonsen, in: *Proceedings of the First International Symposium on Friction Stir Welding*, Thousand Oaks, CA, USA, June 14–16, 1999.
- [29] A.P. Reynolds, *Sci. Technol. Weld. Joining* 5 (2000) 120.
- [30] T.U. Seidel, A.P. Reynolds, *Metall. Mater. Trans. A* 32 (2001) 2879.
- [31] M. Guerra, J.C. McClure, L.E. Murr, A.C. Nunes, in: K.V. Jata, M.W. Mahoney, R.S. Mishra, S.L. Semiatin, D.P. Filed (Eds.), *Friction Stir Welding and Processing*, TMS, Warrendale, PA, USA, 2001, p. 25.
- [32] K. Colligan, in: *Proceedings of the First International Symposium on Friction Stir Welding*, Thousand Oaks, CA, USA, June 14–16, 1999.
- [33] K. Colligan, *Weld. J.* 78 (1999) 229S–237S.
- [34] B. London, M. Mahoney, W. Bingel, M. Calabrese, R.H. Bossi, D. Waldron, in: K.V. Jata, M.W. Mahoney, R.S. Mishra, S.L. Semiatin, T. Lienert (Eds.), *Friction Stir Welding and Processing II*, TMS, 2003, p. 3.
- [35] O.T. Midling, in: T.H. Sanders, Jr., E.A. Strake, Jr. (Eds.), *Proceedings of the Fourth International Conference on Aluminum Alloys*, vol. 1, Georgia Institute of Technology, School of Materials Science and Engineering, Atlanta, GA, USA, 1994, pp. 451–458.
- [36] J.H. Ouyang, R. Kovacevic, *J. Mater. Eng. Perform.* 11 (2002) 51.
- [37] L.E. Murr, R.D. Flores, O.V. Flores, J.C. McClure, G. Liu, D. Brown, *Mater. Res. Innovat.* 1 (1998) 211.
- [38] Y. Li, L.E. Murr, J.C. McClure, *Scripta Mater.* 40 (1999) 1041.
- [39] K.N. Krishnan, *Mater. Sci. Eng. A* 327 (2002) 246.
- [40] G. Biallas, R. Braun, C.D. Donne, G. Staniek, W.A. Kaysser, in: *Proceedings of the First International Symposium on Friction Stir Welding*, Thousand Oaks, CA, USA, June 14–16, 1999.
- [41] M.W. Mahoney, C.G. Rhodes, J.G. Flintoff, R.A. Spurling, W.H. Bingel, *Metall. Mater. Trans. A* 29 (1998) 1955.
- [42] M.A. Sutton, B. Yang, A.P. Reynolds, R. Taylor, *Mater. Sci. Eng. A* 323 (2002) 160.
- [43] Z.Y. Ma, S.R. Sharma, R.S. Mishra, M.W. Mahoney, Unpublished results.
- [44] Z.Y. Ma, S.C. Tjong, L. Geng, *Scripta Mater.* 42 (2000) 367.
- [45] Z.Y. Ma, S.C. Tjong, L. Geng, Z.G. Wang, *J. Mater. Res.* 15 (2000) 2714.
- [46] S.C. Tjong, Z.Y. Ma, *Mater. Sci. Technol.* 15 (1999) 429.
- [47] S. Xu, X. Deng, A.P. Reynolds, T.U. Seidel, *Sci. Technol. Weld. Joining* 6 (2001) 191.
- [48] P. Dong, F. Lu, J.K. Hong, Z. Cao, *Sci. Technol. Weld. Joining* 6 (2001) 281.
- [49] P. Colegrove, H. Shercliff, in: K.V. Jata, M.W. Mahoney, R.S. Mishra, S.L. Semiatin, T. Lienert (Eds.), *Friction Stir Welding and Processing II*, TMS, Warrendale, PA, USA, 2003, p. 13.
- [50] C.B. Smith, G.B. Bendzsak, T.H. North, J.F. Hinrichs, J.S. Noruk, R.J. Heideman, *Ninth International Conference on Computer Technology in Welding*, Detroit, Michigan, USA, 28–30 September 1999, 2000, p. 475.
- [51] G.J. Bendzsak, C.B. Smith, in: *Proceedings of the Second International Symposium on Friction Stir Welding*, Gothenburg, Sweden, June 26–28, 2000.
- [52] A. Askari, S. Silling, B. London, M. Mahoney, in: K.V. Jata, M.W. Mahoney, R.S. Mishra, S.L. Semiatin, D.P. Filed (Eds.), *Friction Stir Welding and Processing*, TMS, Warrendale, PA, USA, 2001, p. 43.
- [53] R.L. Goetz, K.V. Jata, in: K.V. Jata, M.W. Mahoney, R.S. Mishra, S.L. Semiatin, D.P. Filed (Eds.), *Friction Stir Welding and Processing*, TMS, Warrendale, PA, USA, 2001, p. 35.
- [54] M.B. Stewart, G.P. Adamas, A.C. Nunes Jr., P. Romine, *Developments in Theoretical and Applied Mechanics*, Florida Atlantic University, USA, 1998, pp. 472–484.
- [55] A.C. Nunes Jr., in: S.K. Das, J.G. Kaufman, T.J. Lienert (Eds.), *Aluminum 2001*, TMS, Warrendale, PA, USA, 2001, p. 235.
- [56] L. Ke, L. Xing, J.E. Indacochea, *Joining of Advanced and Specialty Materials IV*, ASM International, Materials Park, USA, 2002, pp. 125–134.
- [57] W.J. Arbegast, in: Z. Jin, A. Beaudoin, T.A. Bieler, B. Radhakrishnan (Eds.), *Hot Deformation of Aluminum Alloys III*, TMS, Warrendale, PA, USA, 2003, p. 313.
- [58] J.M. McGlaun, S.L. Thompson, L.N. Kmetyk, M.G. Elrick, *Int. J. Impact. Eng.* 10 (1990) 351.

- [59] DEFORM-2D Version 7.0, Users Manual, Scientific Forming Technologies Corporation, January 30, 2000.
- [60] L.E. Murr, G. Liu, J.C. McClure, *J. Mater. Sci.* 33 (1998) 1243.
- [61] Y.S. Sato, H. Kokawa, M. Enmoto, S. Jogan, *Metall. Mater. Trans. A* 30 (1999) 2429.
- [62] W. Tang, X. Guo, J.C. McClure, L.E. Murr, *J. Mater. Process. Manufact. Sci.* 7 (1998) 163.
- [63] Y.J. Kwon, N. Saito, I. Shigematsu, *J. Mater. Sci. Lett.* 21 (2002) 1473.
- [64] J.A. Wert, *Scripta Metall.* 15 (1981) 445.
- [65] G.W. Lorimer, in: K.C. Russell, H.I. Aaronson (Eds.), *Precipitation Processes in Solids*, Met. Soc. AIME, Warrendale, PA, 1978, p. 87.
- [66] R.H. Brown, L.A. Willey, in: K.R. Van Horn (Ed.), *Aluminum*, vol. 1: Properties, Physical Metallurgy, and Phase Diagrams, ASM, Metals Park, OH, 1967, p. 31.
- [67] Y.S. Sato, M. Urata, H. Kokawa, *Metall. Mater. Trans. A* 33 (2002) 625.
- [68] T. Hashimoto, S. Jyogan, K. Nakata, Y.G. Kim, M. Ushio, in: *Proceedings of the First International Symposium on Friction Stir Welding*, Thousand Oaks, CA, USA, June 14–16, 1999.
- [69] O. Frigaad, O. Grong, O.T. Midling, *Metall. Mater. Trans. A* 32 (2001) 1189.
- [70] Y.J. Chao, X. Qi, *J. Mater. Process. Manufact.* 7 (1998) 215.
- [71] M.Z.H. Khandkar, J.A. Khan, *J. Mater. Process. Manufact.* 10 (2001) 91.
- [72] W.J. Arbegast, P.J. Hartley, in: *Proceedings of the Fifth International Conference on Trends in Welding Research*, Pine Mountain, GA, USA, June 1–5, 1998, p. 541.
- [73] H. Schmidt, J. Hattel, J. Wert, *Model. Simul. Mater. Sci. Eng.* 12 (2004) 143.
- [74] S.R. Sharma, R.S. Mishra, Unpublished research, 2005.
- [75] B. Heinz, B. Skrotzki, *Metall. Mater. Trans. B* 33 (6) (2002) 489.
- [76] L.E. Murr, G. Liu, J.C. McClure, *J. Mater. Mater. Lett.* 16 (1997) 1081.
- [77] G.S. Frankel, Z. Xia, *Corrosion* 55 (1999) 139.
- [78] Y.S. Sato, S.H.C. Park, H. Kokawa, *Metall. Mater. Trans. A* 32 (2001) 3023.
- [79] S.H. Kazi, L.E. Murr, in: K.V. Jata, M.W. Mahoney, R.S. Mishra, S.L. Semiatin, D.P. Field (Eds.), *Friction Stir Welding and Processing*, TMS, Warrendale, PA, USA, 2001, p. 139.
- [80] H.G. Salem, A.P. Reynolds, J.S. Lyons, *Scripta Mater.* 46 (2002) 337.
- [81] R. Braun, L. Litynska-Dobrzynska, *Mater. Sci. Forum* 396–402 (2002) 1531.
- [82] A.F. Norman, I. Brough, P.B. Prangnell, *Mater. Sci. Forum* 331–337 (2000) 1713.
- [83] K.A.A. Hassan, A.F. Norman, P.B. Prangnell, *Mater. Sci. Forum* 396–402 (2002) 1549.
- [84] J.Q. Su, T.W. Nelson, R.S. Mishra, M.W. Mahoney, *Acta Mater.* 51 (2003) 713.
- [85] Z.Y. Ma, R.S. Mishra, M.W. Mahoney, R. Grimes, *Mater. Sci. Eng. A* 351 (2003) 148.
- [86] I. Charit, R.S. Mishra, *Mater. Sci. Eng. A* 359 (2003) 290.
- [87] I. Charit, R.S. Mishra, M.W. Mahoney, *Scripta Mater.* 47 (2002) 631.
- [88] I. Charit, Z.Y. Ma, R.S. Mishra, in: Z. Jin, A. Beaudoin, T.A. Bieler, B. Radhakrishnan (Eds.), *Hot Deformation of Aluminum Alloys III*, TMS, 2003, pp. 331–342.
- [89] P.S. Pao, E. Lee, C.R. Feng, H.N. Jones, D.W. Moon, in: K.V. Jata, M.W. Mahoney, R.S. Mishra, S.L. Semiatin, T. Lienert (Eds.), *Friction Stir Welding and Processing II*, TMS, Warrendale, PA, USA, 2003, p. 113.
- [90] Y.J. Kwon, I. Shigematsu, N. Saito, *Mater. Trans.* 44 (2003) 1343.
- [91] Y.J. Kwon, I. Shigematsu, N. Saito, *Scripta Mater.* 49 (2003) 785.
- [92] K.V. Jata, K.K. Sankaran, J.J. Ruschau, *Metall. Mater. Trans. A* 31 (2000) 2181.
- [93] M. James, M. Mahoney, in: *Proceedings of the First International Symposium on Friction Stir Welding*, Thousand Oaks, CA, USA, June 14–16, 1999.
- [94] Z.Y. Ma, R.S. Mishra, M.W. Mahoney, in: K.V. Jata, M.W. Mahoney, R.S. Mishra, S.L. Semiatin, T. Lienert (Eds.), *Friction Stir Welding and Processing II*, TMS, 2003, pp. 221–230.
- [95] J.Q. Su, T.W. Nelson, C.J. Sterling, *J. Mater. Res.* 18 (2003) 1757.
- [96] I. Charit, R.S. Mishra, in: Y.T. Zhu, T.G. Langdon, R.Z. Valiev, S.L. Semiatin, D.H. Shin, T.C. Lowe (Eds.), *Ultrafine Grained Materials III*, TMS, 2004.
- [97] F.J. Humphreys, M. Hotherly, *Recrystallization and Related Annealing Phenomena*, Pergamon Press, New York, 1995.
- [98] C.G. Rhodes, M.W. Mahoney, W.H. Bingel, M. Calabrese, *Scripta Mater.* 48 (2003) 1451.
- [99] I. Charit, R.S. Mishra, Unpublished research, 2005.
- [100] M. Mahoney, R.S. Mishra, T. Nelson, J. Flintoff, R. Islamgaliev, Y. Hovansky, in: K.V. Jata, M.W. Mahoney, R.S. Mishra, S.L. Semiatin, D.P. Field (Eds.), *Friction Stir Welding and Processing*, TMS, Warrendale, PA, USA, 2001, p. 183.
- [101] A.W. Bowen, *Mater. Sci. Technol.* 6 (1990) 1058.

- [102] J. Hirsch, K. Lücke, *Acta Metall.* 36 (1998) 2863.
- [103] K. Lücke, O. Engler, in: L. Arnberg, et al. (Eds.), *Proceedings of the Third International Conference on Aluminum Alloys*, Norwegian Institute of Technology, Trondheim, Norway, 1992, p. 439.
- [104] R.D. Doherty, D.A. Hughes, F.J. Humphreys, J.J. Jonas, D.J. Jensen, M.E. Kassner, W.E. King, T.R. McNelley, H.J. McQueen, A.D. Rollett, *Mater. Sci. Eng. A* 238 (1997) 219.
- [105] S. Gourder, E.V. Konopleva, H.J. McQueen, F. Montheillet, *Mater. Sci. Forum* 217–222 (1996) 441.
- [106] H.J. McQueen, E. Evangelista, M.E. Kassner, *Z. Metallkd.* 82 (1991) 336.
- [107] R.H. Bricknell, J.W. Edington, *Acta Metall. A* 22 (1991) 2809.
- [108] S.J. Hales, T.R. McNelley, *Acta Metall.* 36 (1988) 1229.
- [109] Q. Liu, X. Huang, M. Yao, J. Yang, *Acta Metall. Mater.* 40 (1992) 1753.
- [110] K. Matsuki, T. Iwaki, M. Tokizawa, Y. Murakami, *Mater. Sci. Technol.* 7 (1991) 513.
- [111] H. Gudmundsson, D. Brooks, J.A. Wert, *Acta Metall. Mater.* 39 (1991) 19.
- [112] K. Ameyama, H. Matsuoka, A. Miyazaki, M. Tokizane, *J. Jpn. Inst. Met.* 53 (1989) 991.
- [113] X. Huang, K. Tsuzaki, T. Maki, *Acta Metall. Mater.* 43 (1995) 3375.
- [114] K. Tsuzaki, X. Huang, T. Maki, *Acta Mater.* 44 (1996) 4491.
- [115] K.A.A. Hassan, A.F. Norman, P.B. Prangell, in: *Proceedings of the Third International Symposium on Friction Stir Welding*, Kobe, Japan, September 27–28, 2001.
- [116] L.E. Murr, E.A. Trillo, S. Pappu, C. Kennedy, *J. Mater. Sci.* 37 (2002) 3337.
- [117] Y. Hovanski, T.W. Nelson, D.P. Field, in: *Proceedings from Joining of Advanced and Specialty Materials*, St. Louis, MO, October 9–11, ASM International, 2000, p. 167.
- [118] Y.S. Sato, H. Kokawa, K. Ikeda, M. Enomoto, S. Jogan, T. Hashimoto, *Metall. Mater. Trans. A* 32 (2001) 941.
- [119] D.V. Field, T.W. Nelson, Y. Hovanski, K.V. Jata, *Metall. Mater. Trans. A* 32 (2001) 2869.
- [120] H. Jin, S. Saimoto, M. Ball, P.L. Threadgill, *Mater. Sci. Technol.* 17 (2001) 1605.
- [121] C.D. Donne, E. Lima, J. Wegener, A. Pyzalla, T. Buslaps, in: *Proceedings of the Third International Symposium on Friction Stir Welding*, Kobe, Japan, September 27–28, 2001.
- [122] X.L. Wang, Z. Feng, S. David, S. Spooner, C.S. Hubbard, in: *Proceedings of the Sixth International Conference on Residual Stresses (ICRS-6)*, IOM Communications, Oxford, UK, 2000, pp. 1408–1420.
- [123] M. Peel, A. Steuwer, M. Preuss, P.J. Withers, *Acta Mater.* 51 (2003) 4791.
- [124] A.P. Reynolds, W. Tang, T. Gnaupel-Herold, H. Prask, *Scripta Mater.* 48 (2003) 1289.
- [125] *ASM Handbook*, vol. 6: *Welding, Brazing, and Soldering*, ASM International, USA, 1995, p. 1097.
- [126] Y.S. Sato, H. Kokawa, M. Enmoto, S. Jogan, T. Hashimoto, *Metall. Mater. Trans. A* 30 (1999) 3125.
- [127] Y.S. Sato, H. Kokawa, M. Enmoto, S. Jogan, T. Hashimoto, *Metall. Mater. Trans. A* 32 (2001) 941.
- [128] D.L. Zhang, L. Zheng, *Metall. Mater. Trans. A* 27 (1996) 3983.
- [129] D.H. Bratland, O. Grong, H. Shercliff, O.R. Myhr, S. Tjøtta, *Acta Mater.* 45 (1997) 1.
- [130] L.E. Svensson, L. Karlsson, H. Larsson, B. Karlsson, M. Fazzini, J. Karlsson, *Sci. Technol. Weld. Joining* 5 (2000) 285.
- [131] B.J. Dracup, W.J. Arbegast, in: *Proceedings of the 1999 SAE Aerospace Automated Fastening Conference & Exposition*, Memphis, TN, October 5–7, 1999.
- [132] L.E. Svensson, L. Karlsson, H. Larsson, B. Karlsson, M. Fazzini, J. Karlsson, *Sci. Technol. Weld. Joining* 5 (2000) 285.
- [133] A. Denquin, D. Allehaux, M.H. Campagnac, G. Lapasset, *Mater. Sci. Forum* 3 (402) (2002) 1199.
- [134] M.G. Dawes, S.A. Karger, T.L. Dickerson, J. Przydatek, in: *Proceedings of the Second International Symposium on Friction Stir Welding*, Gothenburg, Sweden, June 26–28, 2000.
- [135] A. von Strombeck, J.F. dos Santos, F. Torster, P. Laureano, M. Koçak, in: *Proceedings of the First International Symposium on Friction Stir Welding*, Thousand Oaks, CA, USA, June 14–16, 1999.
- [136] L. Magnusson, L. Källman, in: *Proceedings of the Second International Symposium on Friction Stir Welding*, Gothenburg, Sweden, June 26–28, 2000.
- [137] C.D. Donne, G. Biallas, T. Ghidini, G. Raimbeaux, in: *Proceedings of the Second International Symposium on Friction Stir Welding*, Gothenburg, Sweden, June 26–28, 2000.
- [138] P.S. Pao, S.J. Gill, C.R. Feng, K.K. Sankaran, *Scripta Mater.* 45 (2001) 605.
- [139] R.S. Mishra, S.R. Sharma, N.A. Mara, M.W. Mahoney, in: *Proceedings of the International Conference on Joining of Advanced and Specialty Materials III*, ASM International, 2000, p. 157.
- [140] H. Hori, S. Makita, H. Hino, in: *Proceedings of the First International Symposium on Friction Stir Welding*, Thousand Oaks, CA, USA, June 14–16, 1999.
- [141] M. Kumagai, S. Tanaka, in: *Proceedings of the First International Symposium on Friction Stir Welding*, Thousand Oaks, CA, USA, June 14–16, 1999.

- [142] G. Bussu, P.E. Irving, in: *Proceedings of the First International Symposium on Friction Stir Welding*, Thousand Oaks, CA, USA, June 14–16, 1999.
- [143] J.Z. Zhang, R. Pedwell, H. Davies, in: *Proceedings of the Second International Symposium on Friction Stir Welding*, Gothenburg, Sweden, June 2000.
- [144] M. Erisson, R. Sandstrom, J. Hagstrom, in: *Proceedings of the Second International Symposium on Friction Stir Welding*, Gothenburg, Sweden, June 2000.
- [145] N. Jayaraman, P. Prevey, M. Mahoney, in: K.V. Jata, M.W. Mahoney, R.S. Mishra, S.L. Semiatin, T. Lienert (Eds.), *Friction Stir Welding and Processing II*, TMS, 2003, p. 259.
- [146] R. Braun, G. Biallas, C.D. Donne, G. Staniek, in: P.J. Winkler (Ed.), *Materials for Transportation Technology EUROMAT'99*, vol. 1, Wiley/VCH, 1999, pp. 150–155.
- [147] G. Bussu, P.E. Irving, *Int. J. Fatigue* 25 (2003) 77.
- [148] J.R. Gordon, *ASM Handbook*, vol. 6, 1993, p. 1108.
- [149] W.J. Arbegast, K.S. Baker, P.J. Hartley, in: *Proceedings of the Fifth International Conference on Trends in Welding Research*, Pine Mountain, GA, USA, June 1–5, 1998, pp. 558–562.
- [150] D.G. Kinchen, Z. Li, G.P. Adams, in: *Proceedings of the First International Symposium on Friction Stir Welding*, Thousand Oaks, CA, USA, June 1999.
- [151] L.D. Oosterkamp, A. Ivankovic, A. Oosterkamp, in: *Proceedings of the Second International Symposium on Friction Stir Welding*, Gothenburg, Sweden, June 26–28, 2000.
- [152] H.R. Kroninger, A.P. Reynolds, *Fatigue Fract. Eng. Mater. Struct.* 25 (2002) 283.
- [153] E. Hornborg, E.A. Starke Jr., *Acta Metall. Mater.* 41 (1993) 1.
- [154] K.V. Jata, E.A. Starke Jr., *Metall. Trans. A* 17 (1986) 1011.
- [155] M. Graf, E. Hornborg, *Acta Metall.* 25 (1977) 883.
- [156] R.H. Van Stone, T.B. Cox, J.R. Low Jr., J.A. Psioda, *Int. Met. Rev.* 30 (1985) 157.
- [157] J. Gurland, *Plateau*, *Trans. ASM* 56 (1963) 442.
- [158] T. Watanabe, *Texture Microstruct.* 20 (1993) 195.
- [159] J. Corral, E.A. Trillo, Y. Li, L.E. Murr, *J. Mater. Sci. Lett.* 19 (2000) 2117.
- [160] F. Zucchi, G. TrabANELLI, V. Grassi, *Mater. Corros.* 52 (2001) 853.
- [161] E.I. Meletis, P. Gupta, F. Nave, in: K.V. Jata, M.W. Mahoney, R.S. Mishra, S.L. Semiatin, T. Lienert (Eds.), *Friction Stir Welding and Processing II*, TMS, Warrendale, PA, USA, 2003, p. 107.
- [162] J.B. Lumsden, M.W. Mahoney, G. Pollock, C.G. Rhodes, *Corrosion* 55 (1999) 1127.
- [163] F. Hannour, A.J. Davenport, M. Strangwood, in: *Proceedings of the Second International Symposium on Friction Stir Welding*, Gothenburg, Sweden, June 26–28, 2000.
- [164] C.S. Paglia, L.M. Ungaro, B.C. Pitts, M.C. Carroll, A.P. Reynolds, R.G. Buchheit, in: K.V. Jata, M.W. Mahoney, R.S. Mishra, S.L. Semiatin, T. Lienert (Eds.), *Friction Stir Welding and Processing II*, TMS, Warrendale, PA, USA, 2003, p. 65.
- [165] C.S. Paglia, M.C. Carroll, B.C. Pitts, A.P. Reynolds, R.G. Buchheit, *Mater. Sci. Forum* 396–402 (2002) 1677.
- [166] J. Lumsden, G. Pollock, M. Mahoney, in: K.V. Jata, M.W. Mahoney, R.S. Mishra, S.L. Semiatin, T. Lienert (Eds.), *Friction Stir Welding and Processing II*, TMS, Warrendale, PA, USA, 2003, p. 99.
- [167] B.N. Padgett, C. Paglia, R.G. Buchheit, in: K.V. Jata, M.W. Mahoney, R.S. Mishra, S.L. Semiatin, T. Lienert (Eds.), *Friction Stir Welding and Processing II*, TMS, Warrendale, PA, USA, 2003, p. 55.
- [168] J.R. Galvele, S.M. de Micheli, *Corros. Sci.* 10 (1970) 179.
- [169] I.L. Muller, J.R. Galvele, *Corros. Sci.* 17 (1977) 995.
- [170] F. Hannour, A.J. Davenport, S.W. Williams, P.C. Morgan, C.C. Figgures, in: *Proceedings of the Third International Symposium on Friction Stir Welding*, Kobe, Japan, September 27–28, 2001.
- [171] S. Williams, R. Ambat, D. Price, M. Jariyaboon, A. Davenport, A. Wescott, *Mater. Sci. Forum* 426–432 (2003) 2855.
- [172] C.S. Paglia, B.C. Pitts, M.C. Carroll, A.P. Reynolds, R.G. Buchheit, in: S.A. David, T. DebRoy, J.C. Lippold, H.B. Smartt, J.M. Vitek (Eds.), *Proceedings of the Sixth International Conference on Trends in Welding Research*, Pine Mountain, GA, ASM International, 2003, p. 279.
- [173] J.B. Lumsden, G. Pollock, M.W. Mahoney, *Mater. Sci. Forum* 426–432 (2003) 2867.
- [174] A. Merati, K. Sarda, D. Raizenne, C.D. Donne, in: K.V. Jata, M.W. Mahoney, R.S. Mishra, S.L. Semiatin, T. Lienert (Eds.), *Friction Stir Welding and Processing II*, TMS, Warrendale, PA, USA, 2003, p. 77.
- [175] C.G. Andersson, R.E. Andrews, in: *Proceedings of the First International Symposium on Friction Stir Welding*, Thousand Oaks, CA, USA, June, 1999.
- [176] C.G. Andersson, R.E. Andrews, B.G.I. Dance, M.J. Russell, E.J. Olden, R.M. Sanderson, in: *Proceedings of the Second Symposium on Friction Stir Welding*, Gothenburg, Sweden, June 2000.

- [177] T. Hautala, T. Tianien, in: S.A. David, T. DebRoy, J.C. Lippold, H.B. Smartt, J.M. Vitek (Eds.), Proceedings of the Sixth International Conference on Trends in Welding Research, Pine Mountain, GA, ASM International, 2003, p. 324.
- [178] W.B. Lee, S.B. Jung, The joint properties of copper by friction stir welding, *Mater. Lett.* 58 (2004) 1041–1046.
- [179] H.S. Park, T.K. Kimura, T. Murakami, Y. Nagano, K. Nakata, M. Ushio, Microstructure and mechanical properties of friction stir welds of 60%Cu–40%Zn copper alloy, *Mater. Sci. Eng. A* 371 (2004) 160–169.
- [180] K. Okamoto, M. Doi, S. Hirano, K. Aota, H. Okamura, Y. Aono, T.C. Ping, in: Proceedings of the Third International Symposium on Friction Stir Welding, Kobe, Japan, September 27–28, 2001.
- [181] W.A. Baeslack, D.W. Becker, F.H. Froes, *J. Met.* 5 (1984) 46.
- [182] M.C. Juhas, G.B. Viswanathan, H.L. Fraser, in: Proceedings of the Second Symposium on Friction Stir Welding, Gothenburg, Sweden, June 2000.
- [183] M.C. Juhas, G.B. Viswanathan, H.L. Fraser, in: K. Jata, E.W. Lee, W. Frazier, N.J. Kim (Eds.), Proceedings of the Lightweight Alloys for Aerospace Application, TMS, Warrendale, PA, USA, 2001, pp. 209–217.
- [184] T.J. Lienert, K.V. Jata, R. Wheeler, V. Seetharaman, in: Proceedings of the Joining of Advanced and Specialty Materials III, ASM International, Materials Park, OH, USA, 2001, p. 160.
- [185] A.J. Ramirez, M.C. Juhas, *Mater. Sci. Forum* 426–432 (2003) 2999.
- [186] T. Trap, E. Helder, P.R. Subramanian, in: K.V. Jata, M.W. Mahoney, R.S. Mishra, S.L. Semiatin, T. Lienert (Eds.), Friction Stir Welding and Processing II, TMS, Warrendale, PA, USA, 2003, p. 173.
- [187] W.A. Baeslack, J.R. Davis, C.E. Cross, *Metal Handbook*, vol. 6: Welding, Brazing and Soldering, ASM International, 1993, pp. 507–527.
- [188] Occupational Safety and Health Administration, Occupational Exposure to Hexavalent Chromium, OSHA RIN: 1218-AB45, 2001.
- [189] W.M. Thomas, P.L. Threadgill, E.D. Nicholas, *Sci. Tech. Weld. Joining* 4 (1999) 365.
- [190] T.J. Lienert, J.E. Gould, in: Proceedings of the First International Symposium on Friction Stir Welding, Thousand Oaks, CA, USA, June 1999.
- [191] T.J. Lienert, W.L. Stellwag Jr., B.B. Grimmer, R.M. Warke, *Weld. J.* 82 (1) (2003) 1s.
- [192] A.P. Reynolds, M. Posada, J. Deloach, M.J. Skinner, J. Halpin, T.J. Lienert, in: Proceedings of the Third International Symposium on Friction Stir Welding, Kobe, Japan, September 2001.
- [193] M. Posada, J. Deloach, A.P. Reynolds, M. Skinner, J.P. Halpin, in: K.V. Jata, M.W. Mahoney, R.S. Mishra, S.L. Semiatin, D.P. Field (Eds.), Friction Stir Welding and Processing, TMS, Warrendale, PA, USA, 2001, p. 159.
- [194] S.H.C. Park, Y.S. Sato, H. Kokawa, K. Okamoto, S. Hirano, M. Inagaki, *Scripta Mater.* 49 (2003) 1175.
- [195] R. Johnson, P.L. Threadgill, in: S.A. David, T. DebRoy, J.C. Lippold, H.B. Smartt, J.M. Vitek (Eds.), Proceedings of the Sixth International Conference on Trends in Welding Research, Pine Mountain, GA, ASM International, 2003, pp. 88–92.
- [196] M. Posada, J. Deloach, A.P. Reynolds, J.P. Halpin, in: S.A. David, T. DebRoy, J.C. Lippold, H.B. Smartt, J.M. Vitek (Eds.), Proceedings of the Sixth International Conference on Trends in Welding Research, Pine Mountain, GA, ASM International, 2003, pp. 307–312.
- [197] P.J. Konkol, J.A. Mathers, R. Johnson, J.R. Pickens, in: Proceedings of the Third International Symposium on Friction Stir Welding, Kobe, Japan, September 2001.
- [198] A.P. Reynolds, W. Tang, M. Posada, J. Deloach, *Sci. Technol. Weld. Joining* 8 (6) (2003) 455.
- [199] C.J. Sterling, T.W. Nelson, C.D. Sorensen, R.J. Steel, S.M. Packer, in: K.V. Jata, M.W. Mahoney, R.S. Mishra, S.L. Semiatin, T. Lienert (Eds.), Friction Stir Welding and Processing II, TMS, 2003, pp. 165–171.
- [200] ASM Special Handbook: Magnesium and Magnesium Alloys, ASM International, 1999, pp. 106–118.
- [201] R. Johnson, *Indian Foundry J.* 48 (3) (2002) 36–37.
- [202] R. Johnson, *Mater. Sci. Forum* 419–422 (2003) 365.
- [203] K. Nakata, S. Inoki, Y. Nagano, T. Hashimoto, S. Johgan, M. Ushio, in: Proceedings of the Third International Symposium on Friction Stir Welding, Kobe, Japan, September 27–28, 2001.
- [204] W.B. Lee, J.W. Kim, Y.M. Yeon, S.B. Jung, *Mater. Trans.* 44 (2003) 917.
- [205] W.B. Lee, Y.M. Yeon, S.B. Jung, *Mater. Sci. Technol.* 19 (2003) 785.
- [206] S.H.C. Park, Y.S. Sato, H. Kokawa, in: S.A. David, T. DebRoy, J.C. Lippold, H.B. Smartt, J.M. Vitek (Eds.), Proceedings of the Sixth International Conference on Trends in Welding Research, Pine Mountain, GA, ASM International, 2003, p. 267.
- [207] J.A. Esparza, W.C. Davis, E.A. Trillo, L.E. Murr, *J. Mater. Sci. Lett.* 21 (2002) 917–920.
- [208] J.A. Esparza, W.C. Davis, L.E. Murr, *J. Mater. Sci.* 38 (2003) 941–952.
- [209] G. Kohn, S. Antonsson, A. Munitz, in: S.K. Das (Ed.), *Automotive Alloys 1999*, TMS, 2000, pp. 285–292.
- [210] T. Nagasawa, M. Otsuka, T. Yokota, T. Ueki, in: H.I. Kaplan, J. Hym, B. Clow (Eds.), *Magnesium Technology 2000*, TMS, 2000, pp. 383–386.

- [211] S.H.C. Park, Y.S. Sato, H. Kokawa, *Scripta Mater.* 49 (2003) 161.
- [212] S.H.C. Park, Y.S. Sato, H. Kokawa, *Metall. Mater. Trans. A* 34 (2003) 987.
- [213] M.W. Mahoney, W.H. Harrigan, J.A. Wert, in: *Proceedings of the INALCO'98*, vol. 2, Cambridge, UK, April, 1998, pp. 231–236.
- [214] T.W. Nelson, H. Zhang, T. Haynes, in: *Proceedings of the Second Symposium on Friction Stir Welding*, Gothenburg, Sweden, June 2000.
- [215] L.E. Murr, Y. Li, E.A. Trillo, J.C. McClure, *Mater. Technol.* 15 (2000) 37.
- [216] R.A. Prado, L.E. Murr, D.J. Shindo, K.F. Sota, *Scripta Mater.* 45 (2001) 75.
- [217] K. Nakata, S. Inoki, Y. Nagano, M. Ushio, *Mater. Sci. Forum* 426–432 (2003) 2873.
- [218] S.C. Baxter, A.P. Reynolds, in: K. Jata, E.W. Lee, W. Frazier, N.J. Kim (Eds.), *Proceedings of the Lightweight Alloys for Aerospace Application*, TMS, Warrendale, PA, USA, 2001, pp. 283–293.
- [219] S.R. Sharma, R.S. Mishra, M.W. Mahoney, K.V. Jata, in: K.V. Jata, M.W. Mahoney, R.S. Mishra, S.L. Semiatin, D.P. Field (Eds.), *Friction Stir Welding and Processing*, TMS, 2001, pp. 151–157.
- [220] L.E. Murr, Y. Li, R.D. Flores, E.A. Trillo, J.C. McClure, *Mater. Res. Innovat.* 2 (1998) 150.
- [221] L.E. Murr, G. Sharma, F. Contreras, M. Guerra, S.H. Kazi, M. Siddique, R.D. Flores, D.J. Shindo, K.F. Soto, E.A. Trillo, C. Schmidt, J.C. McClure, in: S.K. Das, J.G. Kaufman, T.J. Lienert (Eds.), *Aluminum 2001—Proceedings of the TMS 2001 Annual Meeting Aluminum Automotive and Joining Symposia*, TMS, 2001.
- [222] H. Larsson, L. Karlsson, S. Stoltz, E.L. Bergqvist, in: *Proceedings of the Second International Symposium on Friction Stir Welding*, Gothenburg, Sweden, June 26–28, 2000.
- [223] R.J. Lederich, J.A. Baumann, P.A. Oelgoetz, in: K.V. Jata, M.W. Mahoney, R.S. Mishra, S.L. Semiatin, D.P. Field (Eds.), *Friction Stir Welding and Processing*, TMS, Warrendale, PA, USA, 2001, p. 71.
- [224] J.A. Wert, *Scripta Mater.* 49 (2003) 607.
- [225] W.B. Lee, Y.M. Yeon, S.B. Jung, in: K.V. Jata, M.W. Mahoney, R.S. Mishra, S.L. Semiatin, T. Lienert (Eds.), *Friction Stir Welding and Processing II*, TMS, Warrendale, PA, USA, 2003, p. 123.
- [226] W.B. Lee, Y.M. Yeon, S.B. Jung, *Scripta Mater.* 49 (2003) 423.
- [227] J.A. Baumann, R.J. Lederich, D.R. Bolser, R. Talwar, in: K.V. Jata, M.W. Mahoney, R.S. Mishra, S.L. Semiatin, T. Lienert (Eds.), *Friction Stir Welding and Processing II*, TMS, Warrendale, PA, USA, 2003, p. 199.
- [228] S. Lim, S. Kim, C.G. Lee, S. Kim, *Metall. Mater. Trans. A* 35 (9) (2004) 2837–2843.
- [229] Y.S. Sato, S.H.C. Park, M. Michiuchi, H. Kokawa, *Scripta Mater.* 50 (2004) 1233–1236.
- [230] A.C. Somasekharan, L.E. Murr, *Mater. Charact.* 52 (2004) 49–64.
- [231] K. Kimapong, T. Watanabe, *Weld. J.* 83 (10) (2004) 277S–282S.
- [232] C.M. Chen, R. Kovacevic, *Int. J. Mach. Tool. Manufact.* 44 (2004) 1205–1214.
- [233] J.C. Bassett, S.S. Birley, in: *Proceedings of the Second Symposium on Friction Stir Welding*, Gothenburg, Sweden, June 2000.
- [234] G. Campbell, T. Stotler, *Weld. J.* 78 (1999) 45.
- [235] K.J. Colligan, J.J. Fisher, J.E. Gover, J.R. Pickens, *Adv. Mater. Process.* 160 (2002) 39.
- [236] Z.Y. Ma, R.S. Mishra, M.W. Mahoney, *Scripta Mater.* 50 (2004) 931.
- [237] I. Charit, R.S. Mishra, Unpublished results.
- [238] Z.Y. Ma, R.S. Mishra, in: S. Seel, N.B. Dahotre, J.J. Moore, C. Suryanarayana, A. Agarwal (Eds.), *Surface Engineering: Materials Science II*, TMS, 2003, pp. 243–250.
- [239] P.B. Berbon, W.H. Bingel, R.S. Mishra, C.C. Bampton, M.W. Mahoney, *Scripta Mater.* 44 (2001) 61.
- [240] J.E. Spowart, Z.Y. Ma, R.S. Mishra, in: K.V. Jata, M.W. Mahoney, R.S. Mishra, S.L. Semiatin, T. Lienert (Eds.), *Friction Stir Welding and Processing II*, TMS, 2003, p. 243.
- [241] S.R. Sharma, Z.Y. Ma, R.S. Mishra, *Scripta Mater.* 51 (2004) 237.
- [242] N.E. Paton, C.H. Hamilton, J. Wert, M. Mahoney, *J. Met.* 34 (1982) 21.
- [243] X. Jiang, Q. Wu, J. Cui, L. Ma, *Metall. Trans. A* 24 (1993) 25.
- [244] J. Xinggang, C. Jiangzhong, M. Longxiang, *Acta Metall. Mater.* 41 (1993) 2721.
- [245] R.S. Mishra, T.R. Bieler, A.K. Mukherjee, *Acta Mater.* 43 (1995) 877.
- [246] Z.Y. Ma, R.S. Mishra, M.W. Mahoney, R. Grimes, *Metall. Mater. Trans. A* 36A (6) (2005) 1447.
- [247] R.S. Mishra, R.K. Islamgaliev, T.W. Nelson, Y. Hovansky, M.W. Mahoney, in: K.V. Jata, M.W. Mahoney, R.S. Mishra, D.P. Field (Eds.), *Friction Stir Welding and Processing*, TMS, 2001, p. 205.
- [248] G. Ricciardi, M. Cantello, G. Mollino, W. Varani, E. Garlet, in: *Proceedings of the Second International Seminar on Surface Engineering with High Energy Beam*, Science and Technology, CEMUL-IST, Lisbon, Portugal, 1989, pp. 415–423.
- [249] D. Pantelis, A. Tissandier, P. Manolatos, P. Ponthiaux, *Mater. Sci. Technol.* 11 (1995) 299.

- [250] C. Hu, T.N. Baker, *J. Mater. Sci.* 30 (1995) 891.
- [251] C. Hu, H. Xin, T.N. Baker, *J. Mater. Sci.* 30 (1995) 5985.
- [252] C. Hu, H. Xin, T.N. Baker, *Mater. Sci. Technol.* 12 (1996) 227.
- [253] C. Hu, T.N. Baker, *J. Mater. Sci.* 32 (1997) 5047.
- [254] T.C. Lei, J.H. Ouyan, Y.T. Pei, Y. Zhou, *Mater. Sci. Technol.* 11 (1995) 520.
- [255] L.R. Katipelli, N.B. Dahotre, *Mater. Sci. Technol.* 17 (2001) 1061.
- [256] S.H. Choo, S. Lee, S.J. Kwon, *Metall. Mater. Trans. A* 30 (1999) 1211.
- [257] S.H. Choo, S. Lee, S.J. Kwon, *Metall. Mater. Trans. A* 30 (1999) 3131.
- [258] M.C. Gui, S.B. Kang, *Mater. Lett.* 46 (2000) 2.
- [259] Y. Wang, X. Zhang, G. Zeng, F. Li, *Mater. Des.* 21 (2000) 447.
- [260] Y.S. Wang, X.Y. Zhang, G.T. Zeng, F.C. Li, *Composites, Part A* 32 (2001) 281.
- [261] A.N. Attia, *Mater. Des.* 22 (2001) 451.
- [262] D.L. Zhang, L. Zheng, *Metall. Mater. Trans. A* 27 (1996) 3983.
- [263] T. Din, J. Campbell, *Mater. Sci. Technol.* 12 (1996) 644.
- [264] Y.B. Yu, P.Y. Song, S.S. Kim, J.H. Lee, *Scripta Mater.* 41 (1999) 767.
- [265] D.L. Zalensas (Ed.), *Aluminum Casting Technology*, 2nd ed., AFS Inc., Illinois, 1993, p. 77.
- [266] S. Kumai, J. Hu, Y. Higo, S. Nunomura, *Acta Mater.* 44 (1996) 2249.
- [267] B. Zhang, D.R. Poirier, W. Chen, *Metall. Mater. Trans. A* 30 (1999) 2659.
- [268] M.E. Seniw, J.G. Conley, M.E. Fine, *Mater. Sci. Eng. A* 285 (2000) 43.
- [269] G. Atxaga, A. Pelayo, A.M. Irisarri, *Mater. Sci. Technol.* 17 (2001) 446.
- [270] K.T. Kashyap, S. Murrall, K.S. Raman, K.S.S. Murthy, *Mater. Sci. Technol.* 9 (1993) 189.
- [271] L. Wang, S. Shivkumar, *Z. Metallkd.* 86 (1995) 441.
- [272] T.J. Hurley, R.G. Atkinson, *Trans. AFS* 91 (1985) 291.
- [273] D. Argo, J.E. Gruzleski, *Trans. AFS* 16 (1988) 65.
- [274] J. Wang, S. He, B. Sun, K. Li, D. Shu, Y. Zhou, *Mater. Sci. Eng. A* 338 (2002) 101.
- [275] R.A. Prado, L.E. Murr, D.J. Shindo, J.C. McClure, in: *Proceedings of the First International Symposium on Friction Stir Welding*, Thousand Oaks, CA, USA, June 1999.
- [276] K.N. Krishnan, in: *Proceedings of the International Conference on Welding*, New Delhi, India, February 15–17, 2001.
- [277] K.N. Krishnan, *J. Mater. Sci.* 37 (2002) 473.
- [278] K.A.A. Hassan, A.F. Norman, P.B. Prangnell, *Acta Mater.* 51 (2003) 1923.
- [279] I. Charit, R.S. Mishra, Unpublished results.